5
Results & Discussion

This chapter deals with the regression models based on results obtained from the experimentation and characterization of developed electrode coatings. The developed regression models have been checked for adequacy using analysis of variance (ANOVA) and also discussed the effect of electrode coating ingredients on the various properties had been discussed. This chapter also discusses the results obtained through various experimentation performed on the fabricated dissimilar welds. Microstructural and mechanical characterization findings of the welds are also discussed in detail.

5.1 Development of Regression models for Physicochemical and Thermophysical properties of developed electrode coatings

The experimentation was performed to estimate the density, weight loss, change in enthalpy, thermal conductivity, thermal diffusivity, specific heat, contact angle, surface tension, and spreading area of the developed electrode coatings. The results obtained are summarized in Table 5.1. The linear, quadratic or cubic regression models of these properties have been developed in terms of percentage compositions of individual electrode coating ingredients along with their binary and tertiary mixtures as shown below in Eq. 5.1 to Eq. 5.10:

Density (D) = -0.75228 CaO - 0.20478 CaF_2 - 0.27465 SiO_2 - 14.19958 Al_2O_3 + 0.024391 CaO.CaF_2 + 0.027773 CaO.SiO_2 + 0.51868 CaO.Al_2O_3 + 0.24531 CaF_2.Al_2O_3 + 0.26024 SiO_2.Al_2O_3 - 7.08816 x 10^{-3} CaO.CaF_2.Al_2O_3 - 8.00216 x 10^{-3} CaO.SiO_2.Al_2O_3 - 2.74587 x 10^{-3} CaO.Al_2O_3.(CaO-Al_2O_3) **(5.1)**

% Weight loss (ΔW) = 8.08536 CaO + 0.10556 CaF_2 + 2.0011 SiO_2 + 4.68607 Al_2O_3 - 0.16902 CaO.CaF_2 - 0.33827 CaO.SiO_2 - 0.25206 CaO.Al_2O_3 + 0.10645 CaF_2.SiO_2 - 8.10068 x 10^{-3} CaF_2.Al_2O_3 - 0.11205 SiO_2.Al_2O_3 **(5.2)**

Change in enthalpy (ΔH) = 1.09802 x 10^5 CaO + 38099.18954 CaF_2 + 1.10278 x 10^5 SiO_2 + 2.95007 x 10^6 Al_2O_3 - 3579.75045 CaO.CaF_2 - 3149.04576 CaO.SiO_2 - 65699.28707 CaO.Al_2O_3 - 2486.30403 CaF_2.SiO_2 - 73691.08948 CaF_2.Al_2O_3 - 60659.6385 SiO_2.Al_2O_3 + 1136.42459 CaO.CaF_2.Al_2O_3 + 591.83581 CaO.SiO_2.Al_2O_3 + 805.35673 CaF_2.SiO_2.Al_2O_3 + 360.35492 CaF_2.Al_2O_3.(CaF_2-Al_2O_3) **(5.3)**

Thermal conductivity (T_C) = -0.64012 CaO - 0.36581 CaF_2 - 4.51231 SiO_2 - 3.17872 Al_2O_3 + 0.024529 CaO.CaF_2 + 0.14208 CaO.SiO_2 + 0.029265 CaO.Al_2O_3 + 0.11074 CaF_2.SiO_2 + 0.059467 CaF_2.Al_2O_3 + 0.48011 SiO_2.Al_2O_3 - 2.81985 x 10^{-3} CaO.CaF_2.SiO_2 + 7.43127 x 10^{-4} CaO.CaF_2.Al_2O_3 - 6.13732 x 10^{-3} CaO.SiO_2.Al_2O_3 - 8.29734 x 10^{-3} CaF_2.SiO_2.Al_2O_3 **(5.4)**

Thermal diffusivity (T_D) = 0.28867 CaO - 0.2452 CaF_2 - 1.91019 SiO_2 - 4.11901 Al_2O_3 + 0.055093 CaF_2.SiO_2 + 0.11058 CaF_2.Al_2O_3 + 0.45079 SiO_2.Al_2O_3 - 0.01132 CaF_2.SiO_2.Al_2O_3 **(5.5)**

Specific heat (SH) = 8.86733 CaO + 6.08905 CaF_2 + 43.79249 SiO_2 + 7.02726 Al_2O_3 - 0.40077 CaO.CaF_2 - 1.60641 CaO.SiO_2 + 0.29181 CaO.Al_2O_3 - 1.30345 CaF_2.SiO_2 - 0.42648 CaF_2.Al_2O_3 - 1.69409 SiO_2.Al_2O_3 + 0.042173 CaO.CaF_2.SiO_2 - 3.55789 x 10^{-3} CaO.CaF_2.Al_2O_3 - 0.015796 CaO.SiO_2.Al_2O_3 + 0.051986 CaF_2.SiO_2.Al_2O_3 **(5.6)**

Contact Angle (θ) = 29.14692 CaO - 4.38320 CaF_2 - 137.65478 SiO_2 - 155.96233 Al_2O_3 - 0.52629 CaO.CaF_2 + 0.92595 CaO.SiO_2 + 0.77363 CaO.Al_2O_3 + 2.87487 CaF_2.SiO_2 + 3.19805 CaF_2.Al_2O_3 + 3.96277 SiO_2.Al_2O_3 **(5.7)**

Spreading area (A_s) = 12617.5558 CaO + 5740.04783 CaF_2 - 6584.41055 SiO_2 + 7883.75276 Al_2O_3 - 503.49502 CaO.CaF_2 + 0.225 CaO.SiO_2 + 126.17032 CaO.Al_2O_3 + 86.97055 CaF_2.SiO_2 - 306.92522 CaF_2.Al_2O_3 - 723.02657 SiO_2.Al_2O_3 **(5.8)**

Surface tension (γ) = 8.38644 CaO + 4.52571 CaF_2 + 4.15753 SiO_2 + 9.35061 Al_2O_3 + 0.017594 CaO.CaF_2 + 6.7031 x 10^{-3} CaO.SiO_2 + 1.56922 x 10^{-3} CaO.Al_2O_3 - 1.38742 x 10^{-3} CaF_2.SiO_2 - 0.010102 CaF_2.Al_2O_3 - 0.024866 SiO_2.Al_2O_3 **(5.9)**

Adhesion energy/surface energy (W_a) = -0.19212 CaO + 0.048341 CaF_2 + 1.04956 SiO_2 + 1.01161 Al_2O_3 + 3.77335 x 10^{-3} CaO.CaF_2 - 7.51435 x 10^{-3} CaO.SiO_2 - 3.54292 x 10^{-3} CaO.Al_2O_3 - 0.021699 CaF_2.SiO_2 - 0.021737 CaF_2.Al_2O_3 - 0.025109 SiO_2.Al_2O_3 **(5.10)**

5.1.1 Regression analysis of physicochemical and thermophysical properties

The developed regression models were further analysed using ANOVA. This was done to establish the suitability of model and significance of input parameters along with their interactions on responces (Table 5.2).

Table 5.1: Experimental results of various properties

Coating	Density (g/cm^3)	Weight loss (%)	Change in enthalpy (J/g)	Thermal conductivity (W/mK)	Thermal diffusivity (mm^2/s)	Specific heat (MJ/m^3K)	Contact angle (Θ)	Surface tension (N/m)	Spreading area (mm^2)	Adhesion energy (J/m^2)
C1	1.55	14.99	-11514.7	0.3784	0.3691	1.025	43.365	455.12	6393.04	0.7859
C2	1.522	12.86	-16165.2	0.3816	0.3151	1.211	55.85	459.6	4901.76	0.7176
C3	1.531	15.42	-12923.8	0.3888	0.4118	0.9441	78.585	463.51	3180.84	0.5552
C4	1.52	14.08	-11131.7	0.3775	0.4291	0.8799	67.995	458.93	7321.87	0.6308
C5	1.541	15.19	-16524.2	0.3601	0.3523	1.022	90	464.61	1787.8	0.4646
C6	1.585	14.04	-12731.5	0.3812	0.3434	1.110	83.345	473.94	1799.6	0.5288
C7	1.556	13.29	-14565.2	0.3893	0.3308	1.177	98.16	473.84	3098.54	0.3851
C8	1.513	15.2	-15154.8	0.3733	0.3081	1.212	88.945	453.65	1840.25	0.4620
C9	1.53	13.66	-12658.2	0.3788	0.3233	1.172	34.59	453.01	10855.9	0.8259
C10	1.555	14.92	-13913.3	0.3874	0.3690	1.050	54.275	452.66	12376.7	0.7169
C11	1.52	13.35	-11004.1	0.3688	0.3684	1.001	51.37	450.55	8345.1	0.7318
C12	1.557	14.54	-12660.2	0.3899	0.3824	1.020	85.72	464.4	3594.58	0.4990
C13	1.579	16.84	-18965.8	0.3653	0.2840	1.286	35.79	454.77	11312.1	0.8236
C14	1.568	14.89	-14447.8	0.3516	0.3088	1.139	69.97	455.46	4101.17	0.6114
C15	1.576	16.29	-12823.1	0.3768	0.3252	1.159	90	461.42	1064.58	0.4614
C16	1.521	13.78	-13423.1	0.3848	0.3296	1.167	59.62	449.71	6139.49	0.6771
C17	1.506	14.49	-13468.5	0.3429	0.3058	1.1485	69.53	462.43	4201.76	0.6241
C18	1.463	15.84	-13423.1	0.3756	0.2998	1.208	48.1	470.16	6486.07	0.7841
C19	1.558	13.86	-10364.2	0.3589	0.2942	1.220	86.685	456.1	3397.52	0.4824
C20	1.531	15.02	-11626.9	0.3699	0.3059	1.209	88.83	472.03	3465.05	0.4816
C21	1.578	13.94	-11320.9	0.3921	0.3357	1.168	81.01	457.17	3748.48	0.5286

Table 5.2: ANOVA results of regression models for various properties

Property	Source	Sum of squares	DOF	Mean square	F value	P value	Model status	R^2 value
Density (D)	Model	0.019	11	1.882E-003	4.18	0.0169	S	0.80
	Linear Mixture	8.436E-003	3	2.812E-003	6.24	0.0117	S	
	$CaO.CaF_2$	2.160E-004	1	2.16E-004	0.48	0.5045	NS	
	$CaO.SiO_2$	6.714E-005	1	6.714E-005	0.15	0.7076	NS	
	$CaO.Al_2O_3$	5.512E-003	1	6.512E-003	14.45	0.0035	S	
	$CaF_2.Al_2O_3$	1.499E-006	1	1.499E-006	0.08	0.9551	NS	
	$SiO_2.Al_2O_3$	1.738E-003	1	1.738E-003	13.86	0.0078	S	
	$CaO.CaF_2.Al_2O_3$	1.520E-003	1	1.520E-003	3.37	0.0962	NS	
	$CaO.SiO_2.Al_2O_3$	1.206E-003	1	1.806E-003	4.01	0.0732	NS	
	$CaO.Al_2O_3$.(CaO-Al_2O_3)	1.356 E-003	1	1.521 E-003	2.87	0.1256	NS	
	Residual	4.507E-003	9	4.507E-004				
	Total	0.023	20					
Weight loss (ΔW)	Model	12.33	9	1.37	1.65	0.0212	S	0.77
	Linear Mixture	5.36	3	1.79	2.16	0.015	S	
	$CaO.CaF_2$	0.5	1	0.96	1.16	0.3038	NS	
	$CaO.SiO_2$	3.48	1	3.86	4.66	0.0438	S	
	$CaO.Al_2O_3$	0.46	1	2.28	2.76	0.2313	NS	
	$CaF_2.SiO_2$	0.013	1	0.38	0.46	0.8280	NS	
	$CaF_2.Al_2O_3$	0.14	1	0.002	0.02	0.4901	NS	
	$SiO_2.Al_2O_3$	0.56	1	0.45	0.55	0.1941	NS	
	Residual	9.11	11	0.83				
	Total	21.44	20					
Thermal conductivity (T_C)	Model	2.593E-003	13	1.994E-004	1.73	0.0238	S	0.76
	Linear Mixture	6.886E-004	3	2.295 E-004	1.99	0.2043	NS	
	$CaO.CaF_2$	5.556E-008	1	5.556E-008	14.8	0.0184	S	
	$CaO.SiO_2$	5.164E-005	1	5.164E-005	0.45	0.0361	S	
	$CaO.Al_2O_3$	1.369E-004	1	1.369E-004	1.19	0.03121	S	
	$CaF_2.SiO_2$	4.074E-005	1	4.074E-005	0.35	0.0457	S	
	$CaF_2.Al_2O_3$	5.856 E-04	1	5.856 E-004	5.07	0.059	NS	
	$SiO_2.Al_2O_3$	6.567 E-04	1	6.567 E-004	5.69	0.0485	S	
	$CaO.CaF_2.SiO_2$	1.095 E-04	1	1.095 E-004	0.95	0.3625	NS	
	$CaO.CaF_2.Al_2O_3$	8.084 E-06	1	8.084 E-006	0.07	0.7989	NS	
	$CaO.SiO_2.Al_2O_3$	5.514 E-04	1	5.514 E-004	4.78	0.0651	NS	
	$CaF_2.SiO_2.Al_2O_3$	1.008 E-03	1	1.008 E-003	8.73	0.0213	S	
	Residual	8.078 E-04	7	1.154E-004				
	Total	3.401 E-03	20					
Thermal diffusivity (T_D)	Model	4.688E-03	7	6.697E-004	1.03	0.0455	S	0.75
	Linear Mixture	2.678 E-03	3	8.927E-004	1.37	0.2947	NS	
	$CaF_2.SiO_2$	6.825 E-05	1	6.825 E-005	0.1	0.0315	S	
	$CaF_2.Al_2O_3$	2.152 E-04	1	2.152 E-004	0.33	0.0498	S	
	$SiO_2.Al_2O_3$	1.262 E-04	1	1.262 E-004	0.19	0.0167	S	

	$CaF_2.SiO_2.Al_2O_3$	1.905 E-03	1	1.905 E-003	2.93	0.0107	S	
	Residual	8.451 E-03	13	6.501E-004				
	Total	0.013	20					
Specific heat (SH)	Model	0.11	13	8.578E-003	0.86	0.0178	S	0.69
	Linear Mixture	0.024	3	8.046E-003	0.81	0.3302	NS	
	$CaO.CaF_2$	2.641E-004	1	2.641E-004	0.027	0.0487	S	
	$CaO.SiO_2$	6.221E-005	1	6.221E-005	0.22	0.0320	S	
	$CaO.Al2O_3$	1.727E-003	1	1.727E-003	0.17	0.6890	NS	
	$CaF_2.SiO_2$	3.075E-003	1	3.075E-003	0.31	0.5950	NS	
	$CaF_2.Al_2O_3$	4.739E-004	1	4.739E-004	0.048	0.8332	NS	
	$SiO_2.Al_2O_3$	2.200E-003	1	2.200E-003	6.272	0.0046	S	
	$CaO.CaF_2.SiO_2$	0.024	1	0.024	2.47	0.0165	S	
	$CaO.CaF_2.Al_2O_3$	1.853E-004	1	1.853E-004	0.019	0.8951	NS	
	$CaO.SiO_2.Al_2O_3$	3.652E-003	1	3.652E-003	0.37	0.5631	NS	
	$CaF_2.SiO_2.Al_2O_3$	0.040	1	0.040	3.39	0.0860	NS	
	Residual	0.069	7	9.919E-003				
	Total	0.18	20					
Change in enthalpy (ΔH)	Model	6.679E+07	13	5.138E+006	1.74	0.0234	S	0.76
	Linear Mixture	1.478E+06	3	4.928E+005	0.17	0.9151	NS	
	$CaO.CaF_2$	2.702E+06	1	2.702E+006	0.92	0.037	S	
	$CaO.SiO_2$	1.076E+06	1	1.076E+006	0.37	0.0489	S	
	$CaO.Al_2O_3$	1.574E+05	1	1.574E+005	0.05	0.8238	NS	
	$CaF_2.SiO_2$	2.042E+06	1	2.042E+006	0.69	0.4325	NS	
	$CaF_2.Al_2O_3$	8.446E+06	1	8.446E+006	2.87	0.1342	NS	
	$SiO_2.Al_2O_3$	1.130E+07	1	1.130E+007	3.84	0.0321	S	
	$CaO.CaF_2.Al_2O_3$	1.784E+07	1	1.784E+007	6.06	0.0434	S	
	$CaO.SiO_2.Al_2O_3$	5.028E+06	1	5.028E+006	1.71	0.2326	NS	
	$CaF_2.SiO_2.Al_2O_3$	8.959E+06	1	8.959E+006	3.04	0.1246	NS	
	$CaF_2.Al_2O_3.(CaF_2\text{-}Al_2O_3)$	1.802E+07	1	1.802E+007	6.12	0.0426	S	
	Residual	2.061E+07	7	2.944E+006				
	Total	8.740E+07	20					
Spreading area (A_s)	Model	1.385E+008	9	1.539E+007	10.85	0.0182	S	0.69
	Linear Mixture	1.040E+008	3	3.468E+007	0.99	0.3418	NS	
	$CaO.CaF_2$	8.547E+006	1	8.547E+006	4.01	0.0375	S	
	$CaO.SiO_2$	1.71	1	1.71	11.12	0.0107	S	
	$CaO.Al_2O_3$	5.724E+005	1	5.724E+005	7.02	0.0286	S	
	$CaF_2.SiO_2$	2.550E+005	1	2.550E+005	0.029	0.8669	NS	
	$CaF_2.Al_2O_3$	3.387E+006	1	3.387E+006	6.87	0.0213	S	
	$SiO_2.Al_2O_3$	1.880E+007	1	1.880E+007	2.17	0.1687	NS	
	Residual	9.524E+007	11	8.659E+006				
	Total	2.338E+008	20					
Contact Angle (Θ)	Model	7.842E-003	9	8.837E-004	6.35	0.0273	S	0.88
	Linear Mixture	2.736E-003	3	1.178E-003	3.45	0.0550	NS	
	$CaO.CaF_2$	6.203E-004	1	6.203E-004	0.026	0.8744	NS	
	$CaO.SiO_2$	5.127E-004	1	5.127E-004	0.081	0.7812	NS	
	$CaO.Al_2O_3$	1.225E-003	1	1.225E-003	0.06	0.8105	NS	
	$CaF_2.SiO_2$	4.692E-004	1	4.692E-004	6.89	0.0201	S	

	$CaF_2.Al_2O_3$	5.426E-006	1	5.426E-006	1.01	0.3312	NS	
	$SiO_2.Al_2O_3$	8.232E-004	1	8.232E-004	7.81	0.0176	S	
	Residual	0.014	11	1.143E-003				
	Total	0.031	20					
Surface tension (γ)	Model	1039.31	9	115.48	3E+5	0.0001	S	0.99
	Linear Mixture	1039.27	3	346.42	1E+6	0.0001	S	
	$CaO.CaF_2$	0.010	1	0.010	32.73	0.0001	S	
	$CaO.SiO_2$	1.515E-003	1	1.515E-003	4.75	0.0519	NS	
	$CaO.Al_2O_3$	8.854E-005	1	8.854E-005	0.28	0.6087	NS	
	$CaF_2.SiO_2$	6.490E-005	1	6.490E-005	0.20	0.6607	NS	
	$CaF_2.Al_2O_3$	3.669E-003	1	3.669E-003	11.51	0.0060	S	
	$SiO_2.Al_2O_3$	0.022	1	0.022	69.83	0.0001	S	
	Residual	3.508E-003	11	3.189E-004				
	Total	1039.32	20					
Adhesion energy (W_a)	Model	0.21	9	0.023	4.99	0.0306	S	0.93
	Linear Mixture	0.16	3	0.053	3.18	0.0670	NS	
	$CaO.CaF_2$	4.800E-004	1	4.800E-004	5.01	0.0385	S	
	$CaO.SiO_2$	1.904E-003	1	1.904E-003	5.44	0.0242	S	
	$CaO.Al_2O_3$	4.513E-004	1	4.513E-004	0.027	0.8724	NS	
	$CaF_2.SiO_2$	0.016	1	0.016	4.76	0.0350	S	
	$CaF_2.Al_2O_3$	0.017	1	0.017	1.02	0.3349	NS	
	$SiO_2.Al_2O_3$	0.023	1	0.023	1.36	0.2687	NS	
	Residual	0.018	11	0.017				
	Total	0.039	20					

Note: DOF – Degree of freedom; S – Significant; NS – Not Significant

In Table 5.2, the R^2 values for all properties approaching unity, and it indicates that the response model value fits closely to the actual experimental values with less variation. The variations of predicted values from actual values for various properties are shown in Figure 5.1.

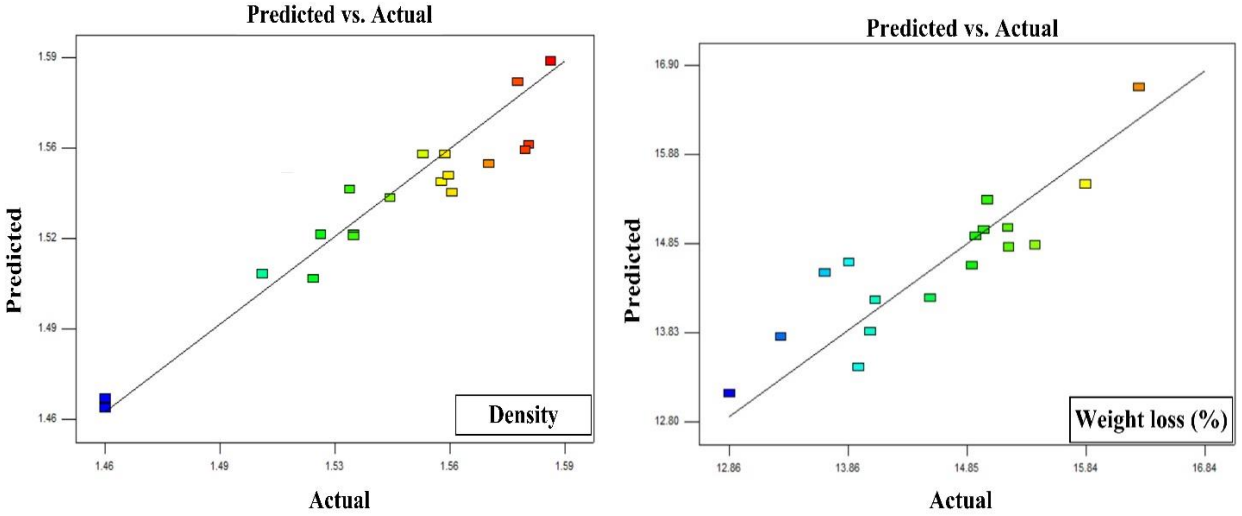

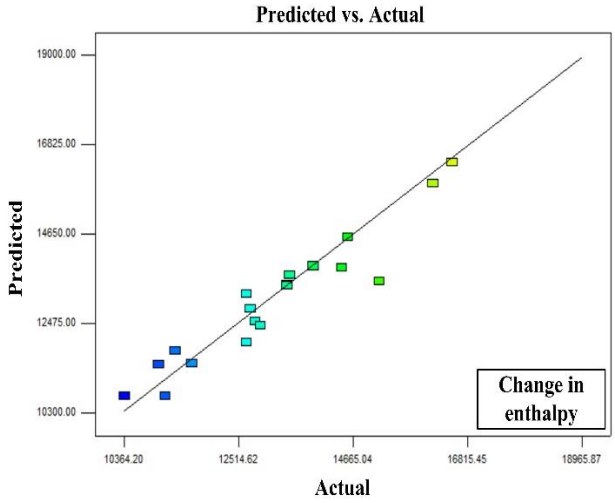
Predicted vs. Actual
Predicted
Actual
19000.00
16825.00
14650.00
12475.00
10300.00
10364.20
12514.62
14665.04
16815.45
18965.87
Change in enthalpy

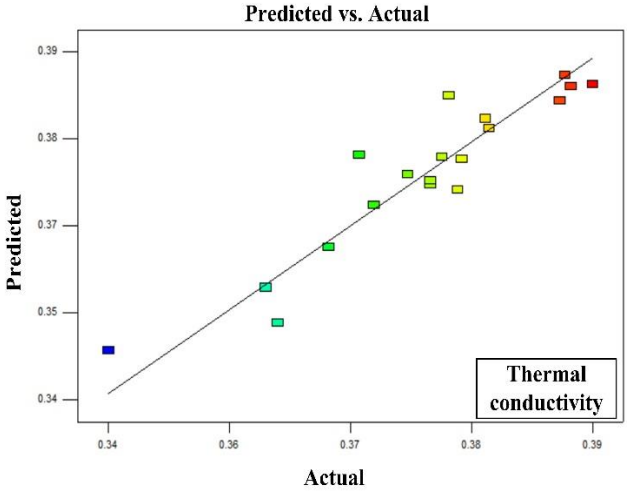
Predicted vs. Actual
Predicted
Actual
0.39
0.38
0.37
0.35
0.34
0.34
0.36
0.37
0.38
0.39
Thermal conductivity

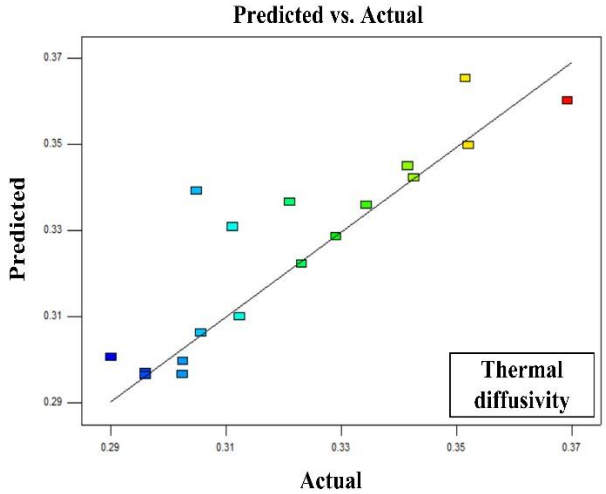
Predicted vs. Actual
Predicted
Actual
0.37
0.35
0.33
0.31
0.29
0.29
0.31
0.33
0.35
0.37
Thermal diffusivity

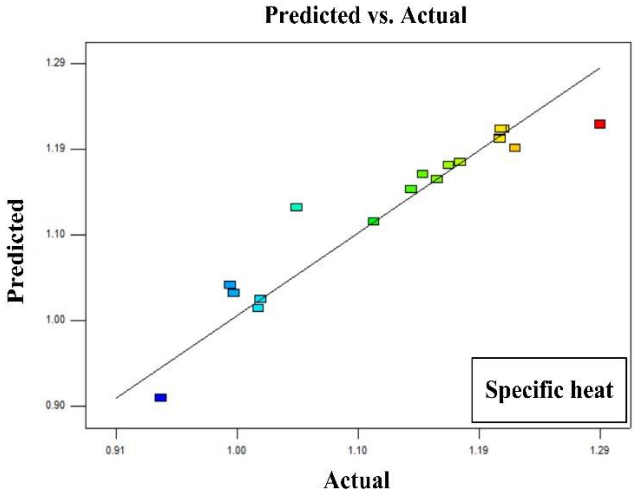
Predicted vs. Actual
Predicted
Actual
1.29
1.19
1.10
1.00
0.90
0.91
1.00
1.10
1.19
1.29
Specific heat

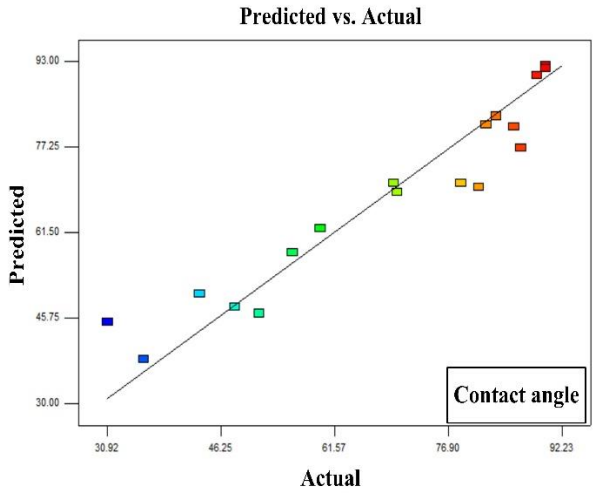
Predicted vs. Actual
Predicted
Actual
93.00
77.25
61.50
45.75
30.00
30.92
46.25
61.57
76.90
92.23
Contact angle

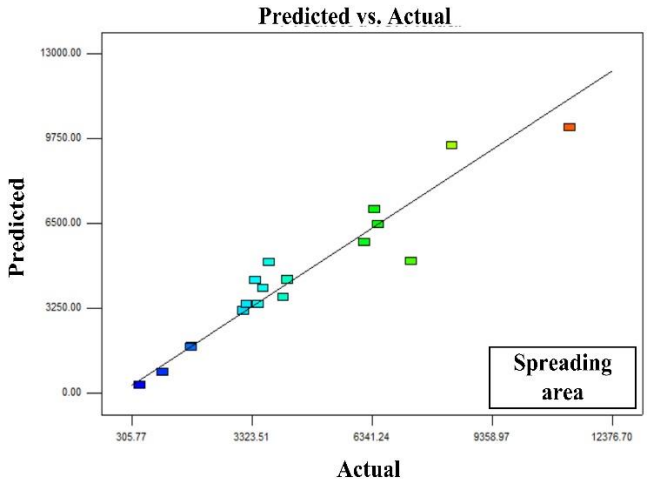
Predicted vs. Actual
Predicted
Actual
13000.00
9750.00
6500.00
3250.00
0.00
305.77
3323.51
6341.24
9358.97
12376.70
Spreading area

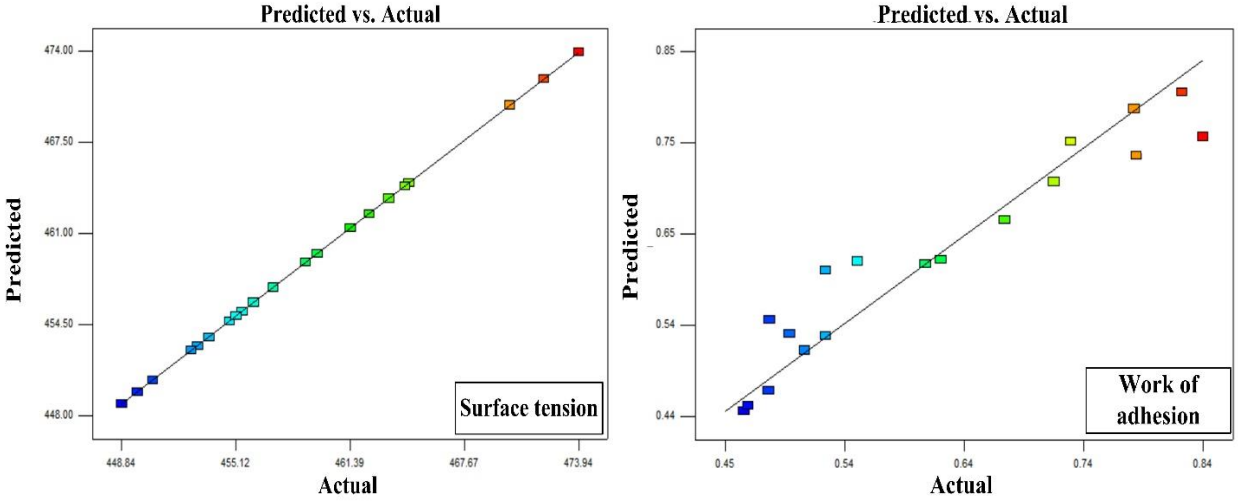

Figure 5.1: Predicted vs. actual plots

5.1.2 Effect of coating ingredients and their interactions on the properties

5.1.2.1 Density

It can be seen from Table 5.2 and Table A1, every individual coating ingredient has a significant decreasing effect on density. $SiO_2.Al_2O_3$ is the only binary mixture that has a significantly increasing effect on density. Ternary mixtures do not show any effect on the density of these coating formulations. Slag-metal reactions take place during the welding process with coated electrodes. SiO_2 and Al_2O_3 oxides are known as network former, which has an increasing effect on the density of the molten slag. During the welding process, if oxide inclusions in the weld increase, it can decrease the fluidity and increase the density due to its capability to form networks. CaO, Al_2O_3, and SiO_2 present in the coating reacts during the welding and form SiO_4^{4-} complexions, which help to reduce the oxide inclusion in the weld and controls the fluidity of the weld pool (Eq. 5.11, 5.12). Also, when the Al reacts with the SiO_2 present in the slag Al_2O_3 (slag) forms, which improves the slag detachability and reduce the diffusible hydrogen content and this improves the welding quality (Eq. 5.13) (Burck et al., 1990).

$$CaO = Ca^{2+} + O^{2-} \quad (5.11)$$

$$SiO_2 + 2O^{2-} = SiO_4^{4-} \quad (5.12)$$

$$2Al + \frac{3}{2} SiO_2\,(slag) = 3Si + Al_2O_3\,(slag) \quad (5.13)$$

5.1.2.2 Weight loss

The thermal stability of the electrode coating constituents is an essential aspect of flux coated electrode welding. Welding performance and weld quality may get affected due to the thermal instability of the flux constituents (Sharma et al., 2018). Adverse effects are being seen on the slag performance due to the hygroscopic nature (H_2O chemically bonded) of the electrode coatings. SiO_2 and Al_2O_3 are the oxides that have a melting temperature above 1710°C and 2072°C, respectively, which are thermally stable. From Table 5.1, it was observed that coating mixture 2 and coating mixture 7 have lower weight loss as compared to other compositions, which contains a higher amount of silica and alumina having higher thermal stability at a higher temperature. From regression analysis, it was observed that (Table 5.2 and Table A1) individual constituents has significantly increasing effect on the weight loss (%) of different coating mixtures while binary mixture $CaO.SiO_2$ has a significant decreasing effect on weight loss. Other binary mixtures do not significantly affect the weight loss of different mixtures. The CaO mineral added to prepare the coating mixture is hygroscopic in nature and have a increasing effect on weight loss. Due to the hygroscopic nature, it leads to the reduction in viscosity of the slag and increases the chances of contamination from air or moisture. Moisture has a noticeable effect on coating mixtures containing chlorides and fluorides. CaF_2 reduces the hygroscopic nature of CaO, as reported earlier (Kanjilal et al., 2006). Figure 5.2 presents the relation of weight

loss vs temperature for some electrode coatings. In these plots, it can be seen that as the temperature increases, the flux coating weight is reduced. The weight loss with the temperature rise represents the thermal stability of these flux coatings. The maximum weight loss (16.84%) was observed in coating number C13 (Table 5.1). The lowest weight gain was observed in the case of coating number C2 (12.86%). Figure 5.2 represents the trend of weight loss in different coatings as the temperature rises which, explains the thermal stability of various coatings at high temperatures.

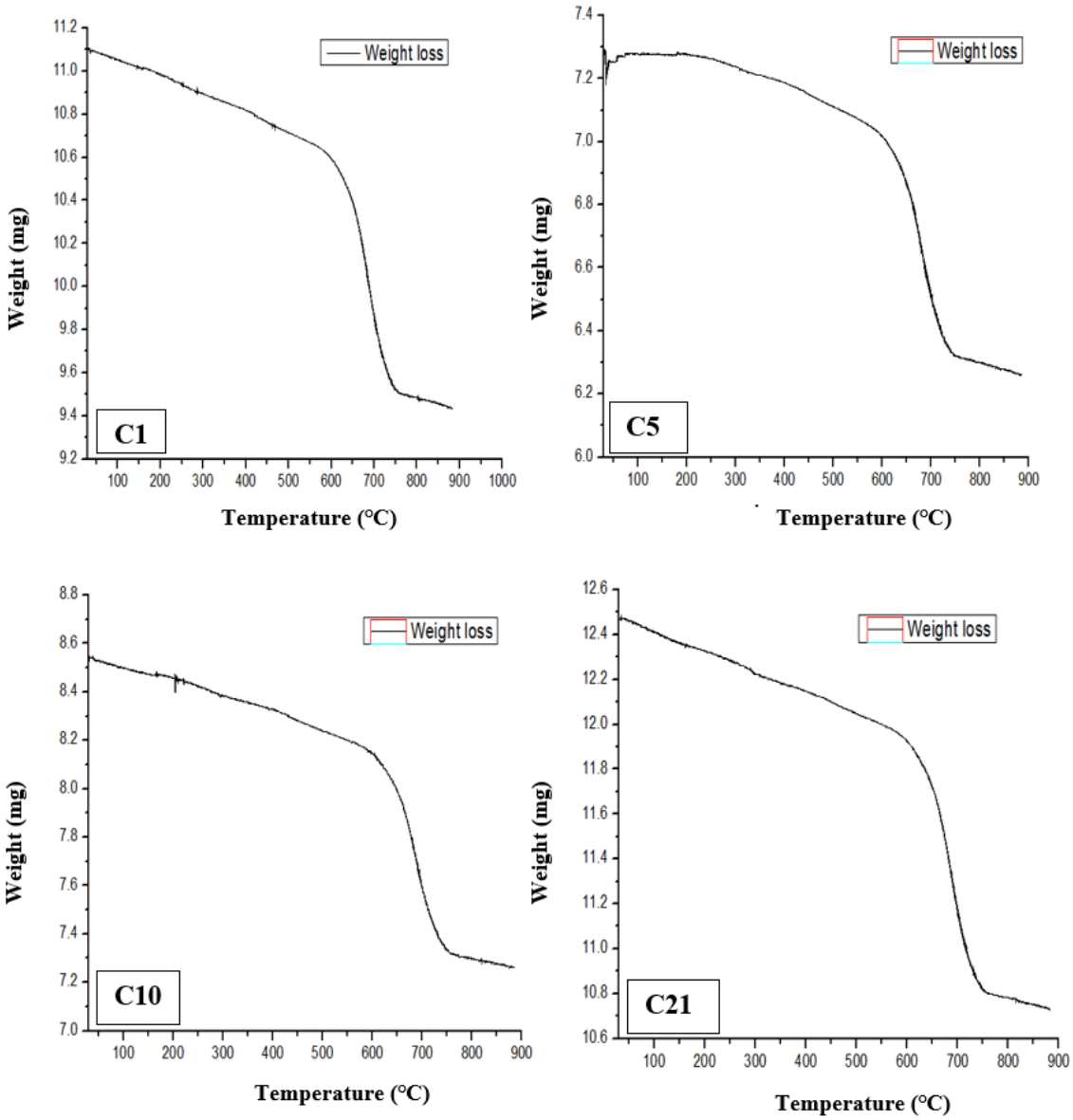

Figure 5.2: Weight vs. Temperature plots for various electrode coatings

5.1.2.3 Change in enthalpy

Table 5.1 presents the change in enthalpy values of different coating mixtures, which are in negative values, shows that the nature of reactions taking place is exothermic, i.e., coating mixture releases heat. Individual coating mixture ingredients do not have a significant effect on enthalpy (From Table 5.2 and Table A1). $CaO.CaF_2$, $SiO_2.CaO$ and $Al_2O_3.SiO_2$ binary mixtures have significant decreasing effect on the change in enthalpy, while other binary mixtures do not have significant affect. From Table 5.1, it was observed that coating composition 11 has the minimum value of the change in enthalpy, and coating composition 13 has the maximum value. Figure 5.3 presents the plots of heat flow vs temperature for some electrode coatings. During the heating cycle, small endothermic peaks were observed in the temperature range of (675°C to 700°C). Thus the enthalpy change was calculated for all the electrode coatings using these plots.

All the coatings behave differently and have different ΔH values. The higher the negative value of ΔH, the higher energy is released during the reaction. Thermal scanning provides qualitative and quantitative information to the thermal properties of solid materials such as the melting and degradation temperatures, glass transition temperature, melt and crystallization enthalpy, specific and latent heats, polymorphism, and purity of the materials.

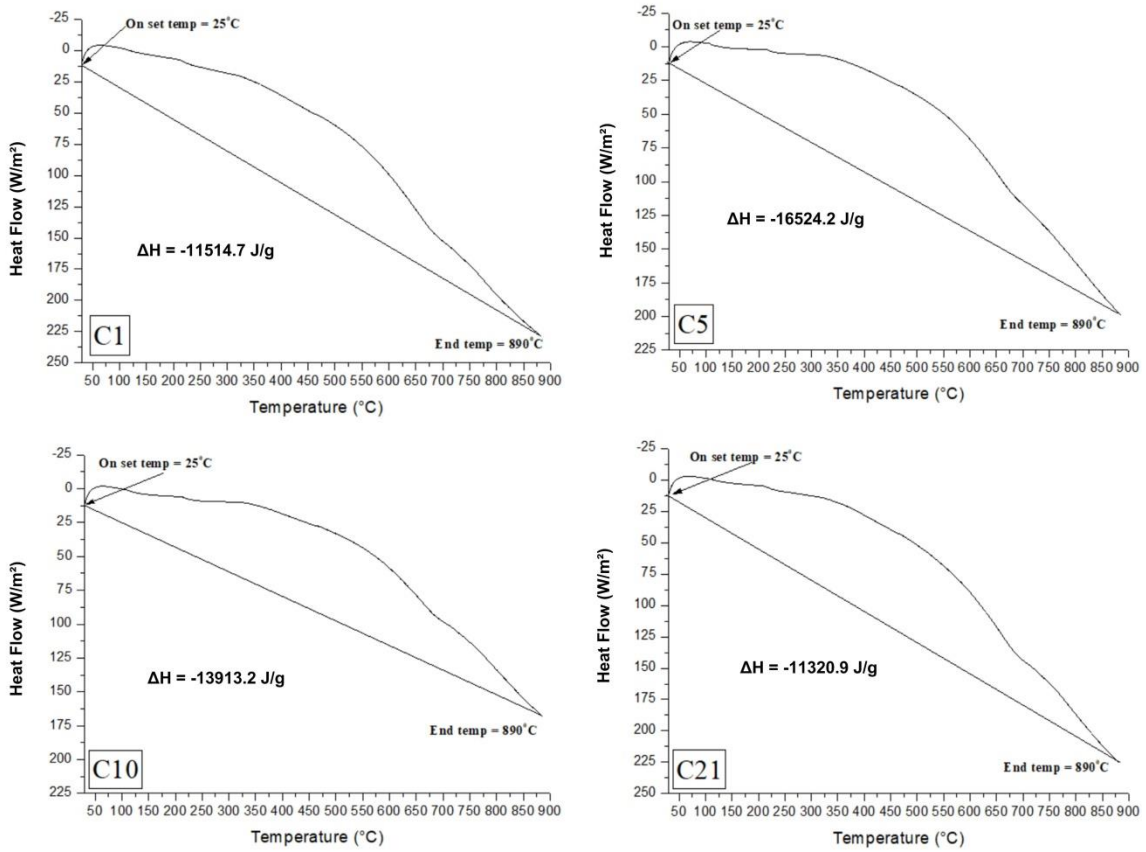

Figure 5.3: Heat flow vs. temperature plots for various electrode coatings

5.1.2.4 Thermal properties

The presence of network forming chains has a significant effect on the thermal behavior of the fluxes. As the SiO_2 content in the welding flux increases, it also increases the thermal conductivity of the fluxes due to the presence of Si^{4+} covalently bonded ions in the network chain (Kerstan et al.; 2011). The nature of the cations present in the mixture significantly affects the thermal conductivity of the welding fluxes. The physical and thermal properties were influenced by the non-bridging oxygen available in the system. A significant role of alkaline ions was observed in controlling the thermo-physical properties (density, thermal conductivity, thermal expansion, and thermal diffusivity) of alumina-silicate based glasses (Kerstan et al. 2011; Kaur et al., 2011; Garai et al., 2015). Thermal conductivity was observed higher if the mixture contains Si^{4+} ions, which have greater polarization. Coating 2 and coating 7 have a higher amount of silica and alumina, and from the experimental analysis, their thermal conductivities are higher as compared to other coatings. From the regression analysis, it was observed that individual coating ingredients do not have significant effect on the thermal conductivity. The binary mixtures show significantly increasing effect on the thermal conductivity except $CaF_2.Al_2O_3$ binary mixture. $CaF_2.Al_2O_3.SiO_2$ is the ternary mixture that shows significant decreasing effect on the thermal conductivity. From the regression analysis, it can be observed that binary mixtures (Table 5.2 and Table A1). $CaF_2.Al_2O_3$, $CaF_2.SiO_2$, $SiO_2.Al_2O_3$ have significantly increasing effect on the thermal diffusivity. $CaF_2.Al_2O_3.SiO_2$ ternary mixture significantly decreases the thermal diffusivity of the coating mixtures. It was observed that $CaO.CaF_2.SiO_2$ ternary mixture significantly increasing the specific heat (Table 5.2 and Table A1).$CaF_2.Al_2O_3$ binary mixture has a significant decreasing effect on specific heat of coating mixtures.

5.1.2.5 Wettability properties

The contact angle is the primitive data for wettability study. It indicates the degree of wetting at the interface of the solid-liquid surface. Small contact angles (< 90°) correspond to high wettability, while large contact angles (> 90°) correspond to low wettability. In welding, there is a requirement for an optimized wetting property. It ensures that flux provides a protecting shield and acts as a blanket, saving the weld pool from environmental impurities and gases. The individual and interaction effect of coating composition constituents on the wettability properties has been carried out using regression models and analyzed with the help of ANOVA using the F-Test (Table 5.2 and Table A1). It was observed that the binary mixture $CaF_2.SiO_2$ and $SiO_2.Al_2O_3$ have significant increasing effect on the contact angle. Previous researchers observed and reported that the contact angle is controlled by free oxygen available during high-temperature reactions. Silica (SiO_2) is a strong network former which during reactions lowers the availability of O^{2-} (free oxygen ions), which are generally present on the solid/liquid interface, hence increasing the interfacial tension and contact angle (Kim et al., 2015; Kingery et al., 1953; Yanhui et al, 2014; Shigeta et al., 1989; Jung et al., 2010). From Table 4.4 and Table 5.1, it can be seen that the coating compositions with a higher amount of $CaO.CaF_2$ (C1, C3, C13) having a low contact angle while the compositions with low $CaO.CaF_2$ and high $SiO_2.Al_2O_3$ possesses a high contact angle. Better wettability between the substrate and the coating composition was observed when the contact angle was low, which results in better spreadability. A larger spreading area was observed in the compositions those are having a lower contact angle. From the regression analysis, binary mixtures $CaO.SiO_2$, $CaO.Al_2O_3$, have a significant increasing effect on the spreading area, whereas binary mixtures $CaO.CaF_2$ and $CaF_2.Al_2O_3$ have significant decreasing effect. The developed coatings are highly basic (Higher Basicity Index) in nature. The addition of basic oxides lowers the viscosity of the melt, which also leads to a low contact angle and larger spreading area (Crespo et al., 2010).

According to Eq. 4.7 ($\gamma_{LG} = x_1 f_1 + x_2 f_2 + x_3 f_3 + \ldots\ldots\ldots\ldots\ldots x_t f_t$), surface tension depends on the individual constituent and their mole fraction. Surface tension factor (f_t) for different ingredients was obtained from the previous studies (Kim et al., 2015; Yanhui et al., 2014). Surface tension values for different coating compositions were calculated and presented in Table 5.1. From the regression model in Table 5.2 and Table A1, it was observed that the binary mixtures $CaO.CaF_2$, has a significant increasing effect on surface tension. Binary mixtures $CaF_2.Al_2O_3$ and $SiO_2.Al_2O_3$ show significantly decreasing effect on surface tension. Earlier researches observed a correlation of contact angle and interfacial tension because of the strong chemical reactions at the solid/liquid interface due to the sharing of electrons, which results in higher binding energies and strong chemical bonds. When the basic oxides like CaO dissociate, it releases the free oxygen (O^{2-}), and this free oxygen has the tendency to modify the complex network structures made by SiO_2 due to its strong network forming ability. SiO_2 reduces the free oxygen ions, which results in an increase in interfacial tension. From Table 5.1 and Table 5.2, it can be seen that the composition C18 is having a higher amount of $SiO_2.Al_2O_3$ with low $CaO.CaF_2$ results in higher surface tension. Jung et al., 2010 also agree that an increase in the Al_2O_3 in the flux increases the surface tension in $CaO\text{-}SiO_2\text{-}Al_2O_3$ flux system. So, the addition of Al_2O_3 by replacing SiO_2 in the coating compositions leads to higher surface tension due to the increase in AlO_4^{5-} and SiO_4^{4-} networks due to bulk polymerization. According to Kim et al., (2015), as the TiO_2/SiO_2 ratio increases, the surface tension increased, and it decreases with the increasing SiO_2/Al_2O_3 ratio.

From the regression analysis, it was observed that binary mixtures $CaO.CaF_2$ and $CaO.SiO_2$ have significantly increasing effect on the adhesion energy. With an increase in CaF_2 in the flux mixture, an increase in the adhesion energy was observed. Binary mixture $CaF_2.SiO_2$ has significantly decreasing effect on the adhesion energy. Dissociation of basic oxides produces the free oxygen ions, which has a decreasing effect on the contact angle, thus increases the adhesion energy. In welding operations viscosity and interfacial tension influence the smoothness of weld. A low interfacial tension produces a concave bead while higher produces a convex bead. So, the proportion of minerals present in coating plays an important role in controlling the

basicity index, physicochemical properties, and wettability characteristics. The adhesion energy is inversely proportional to the measured contact angle. The addition of CaF_2 in the flux decreases the viscosity and increases its flow-ability by decreasing the interfacial tensions.

5.1.3 Contour surface plots for various properties

The contour plot is a two-dimensional (2D) representation of the response plotted against combinations of mixture components. The lines on the contour plots represent a constant response value, whereas different colors represent a possible range of output values. The contour plots depicting values of various estimated properties for different proportions of electrode coating ingredients as shown in Figure 5.4. The variation of a particular property response with respect to electrode coating ingredients can be easily observed from these plots.

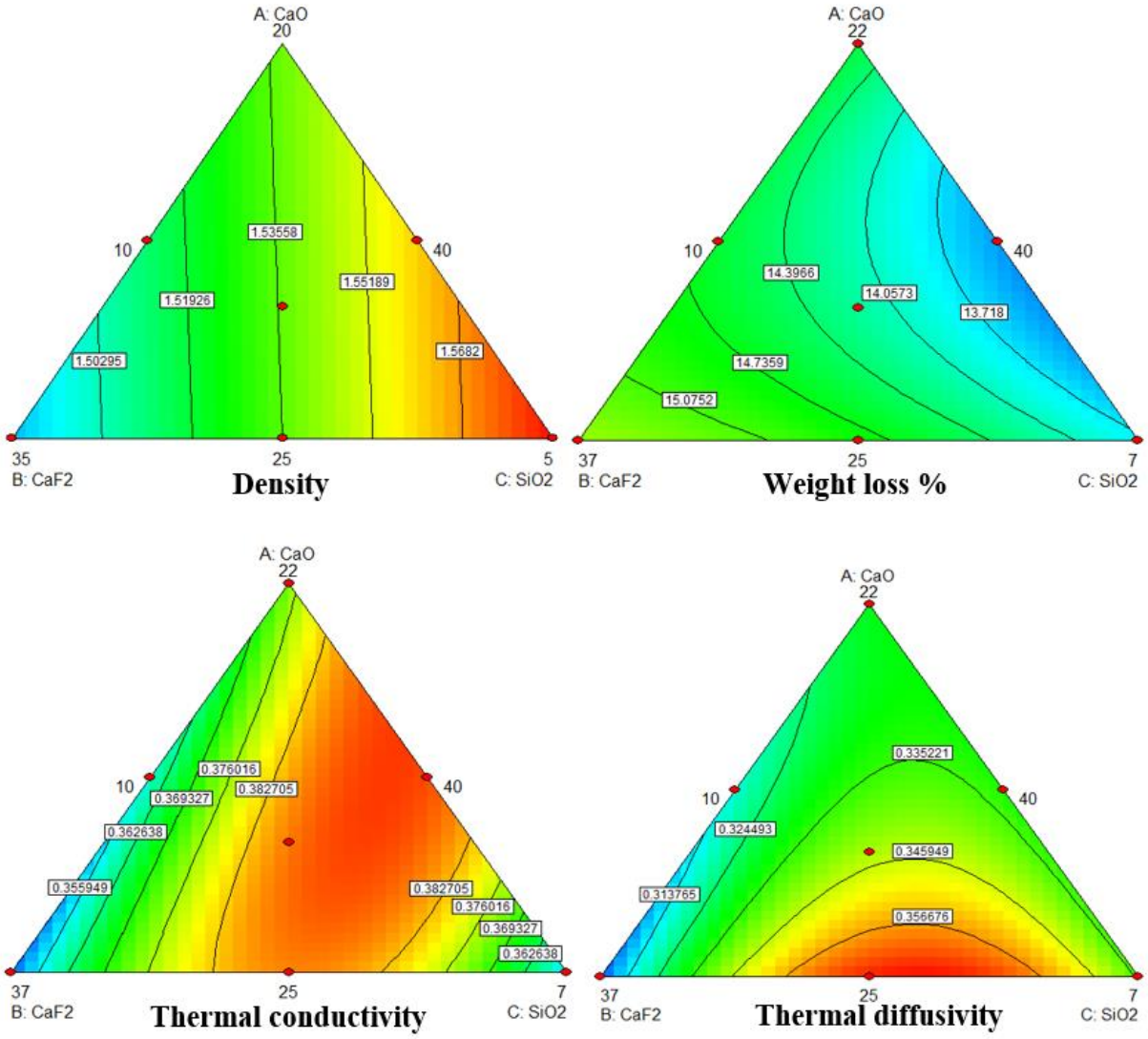

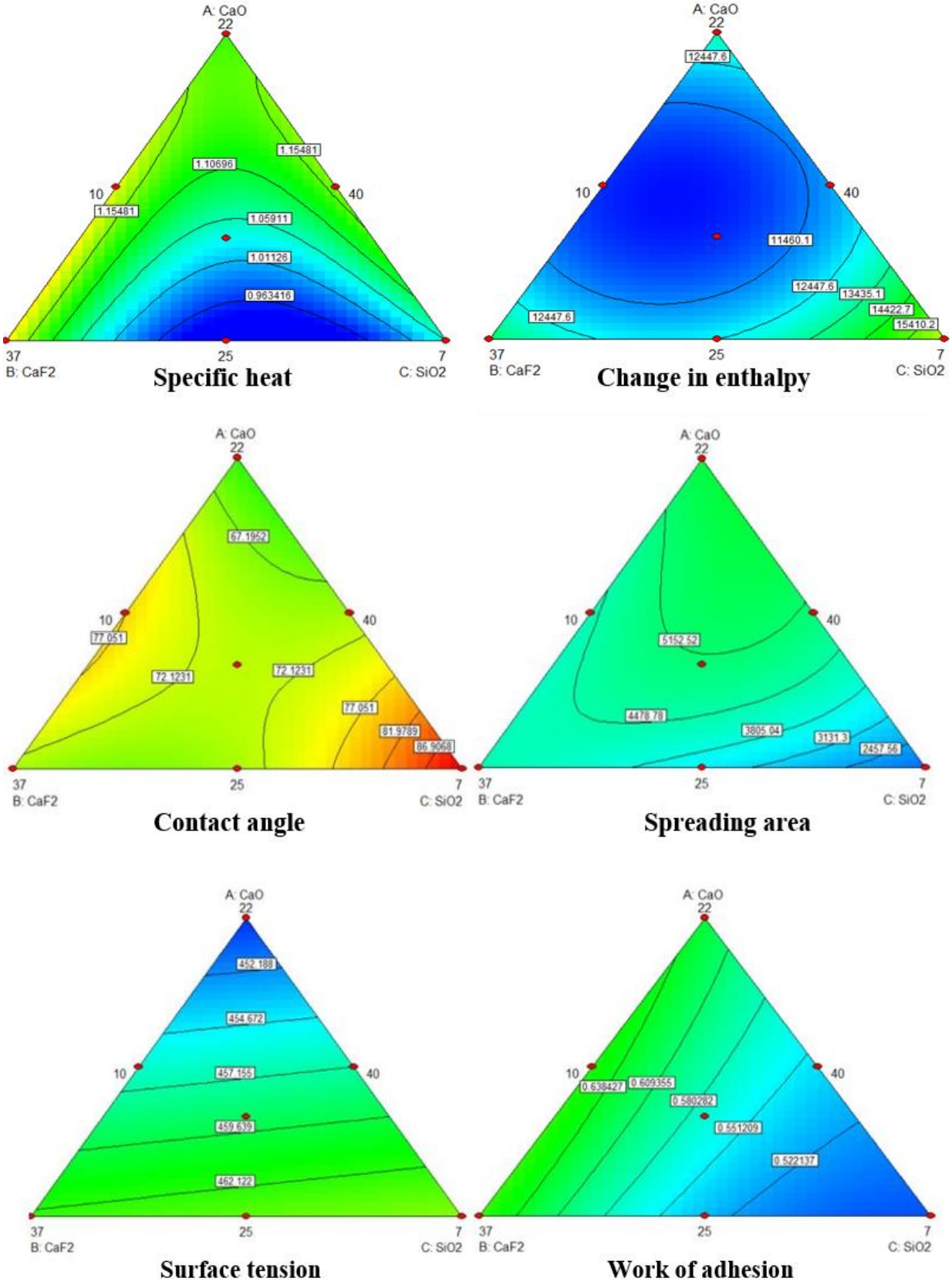

Figure 5.4: Contour surface plots

5.1.4 Multi objective optimization and model validation

The simultaneous optimization of more than one response is a multi-objective, multivariable nonlinear optimization problem. Derringer et al., 1980 proposed a multiobjective optimization method that makes use of desirability function, which is actually the transformation of the response variable into a value. Overall or composite desirability (D) is the weighted geometric mean of individual desirability of various responses. Thus, the simultaneous optimization of several responses gets reduced to optimizing a single response. Weights are fixed according to the importance of an objective function in the multiobjective optimization. The composite desirability (Harington, 1965; Castillo, 1996) is given by Eq. 5.14 and Eq. 5.15:

$$D = (d_1^{W_1} . d_2^{W_2} . d_3^{W_3} \dots\dots\dots\dots . d_n^{W_n})^{\frac{1}{\Sigma_i^n W_i}} \quad (5.14)$$

$$D = (\Pi_i^n d_i^{W_i})^{\frac{1}{\Sigma_i^n W_i}} \quad (5.15)$$

Here n is a number of property responses, d_i is the desirability of a particular property response, and w_i is the weight factor. Table 5.3 shows the three multiobjective optimized solutions with equal weights to all the weld responses. The optimized solutions have been obtained for the optimization of various properties.

The developed regression model of various properties was validated using four randomly selected electrode coatings for conducting the confirmatory experiments. The experimental results, along with the predicted values, are summarized in Table 5.4 and Table 5.5. The error percentage in all the responses should less than 5% which validates the model. The actual Vs predicted values for all the properties are presented in Figure 5.5.

Table 5.3: Optimum solution of electrode coating mixtures for various properties

S.No	CaO	CaF_2	SiO_2	Al_2O_3	D	ΔW	ΔH	T_C	T_D	SH	Θ	A_s	γ	W_a	Desirability
1	22.95	40	8.229	3.819	1.5551	13.27	11542.1	0.391	0.3320	1.18461	58.66	2186.26	462.16	0.4713	0.974
2	22.98	38.678	8.339	5.000	1.5398	14.07	13295.3	0.388	0.3218	1.01535	58.55	2211.78	461.43	0.4714	0.973
3	23.03	36.962	10.00	5.000	1.5068	14.96	15682.1	0.380	0.3097	1.21530	60	1994.94	468.02	0.4727	0.97

Table 5.4: Error % for physicochemical and thermophysical properties

Coating mixture				Predicted						Actual					
CaO	CaF_2	SiO_2	Al_2O_3	D	W_L	ΔH	Tc	Td	SH	D	WL	ΔH	Tc	T_D	SH
25.0	38.5	8.5	3.0	1.525	14.83	12454.1	0.387	0.365	0.924	1.531	15.42	12923.8	0.388	0.411	0.944
20	40	10	5	1.53	16.75	14473.6	0.382	0.321	1.091	1.556	16.29	14565.2	0.3893	0.3308	1.177
25	40	9	1	1.549	14.59	13841.8	0.3767	0.336	1.172	1.568	14.89	14447.8	0.3516	0.3088	1.139
23.5	40	8.5	3	1.553	13.44	11816.4	0.3917	0.331	1.213	1.578	13.94	11320.9	0.3921	0.3357	1.168

Error %					
D	WL	ΔH	Tc	Td	SH
0.39	3.95	3.63	0.25	11.19	2.11
1.69	2.74	0.63	1.91	2.98	7.88
1.18	2.05	4.3	6.56	8.33	2.81
1.6	3.72	4.19	0.1	1.20	3.70

Table 5.5: Error % for wettability properties

				Predicted value				Actual value				Error %			
CaO	CaF_2	SiO_2	Al_2O_3	Θ	A_s	γ	W_a	Θ	A_s	γ	W_a	Θ	A_s	γ	W_a
25.0	38.5	8.5	3.0	81.42	3385.2	463.5	0.531	78.58	3180.8	463.52	0.555	3.48	6.05	0	4.32
20	40	10	5	94.46	2645.5	473.54	0.323	98.16	3098.5	473.84	0.315	3.76	14.0	0	2.47
25	40	9	1	62.41	4899.8	455.71	0.674	69.97	4101.7	455.77	0.611	10.8	16	0	9.34
23.5	40	8.5	3	78.73	3754.6	457.16	0.544	81.01	3748.4	457.1	0.528	2.81	0.15	0	2.94

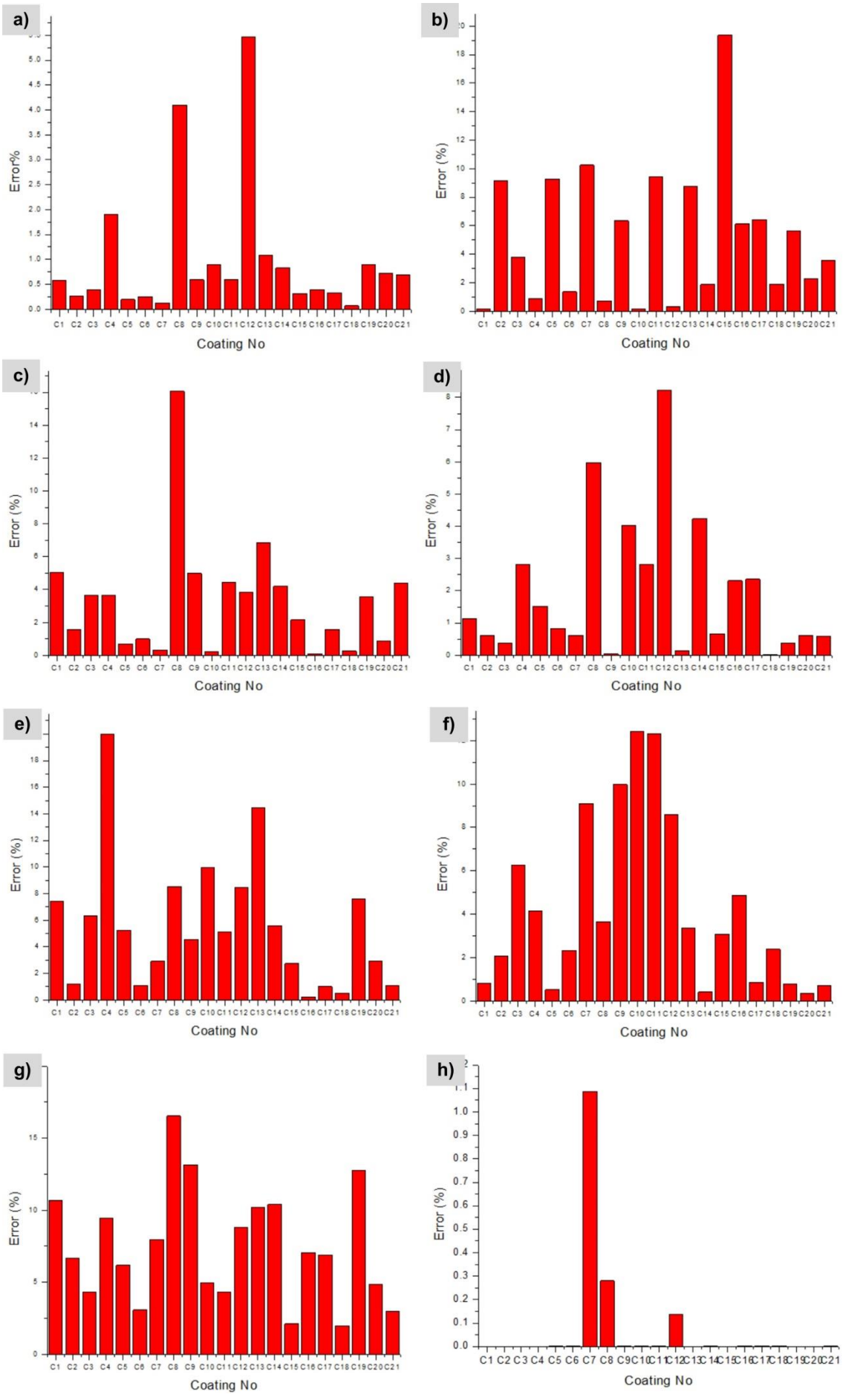
a)
Error%
Coating No
b)
Error (%)
Coating No
c)
Error (%)
Coating No
d)
Error (%)
Coating No
e)
Error (%)
Coating No
f)
Error (%)
Coating No
g)
Error (%)
Coating No
h)
Error (%)
Coating No

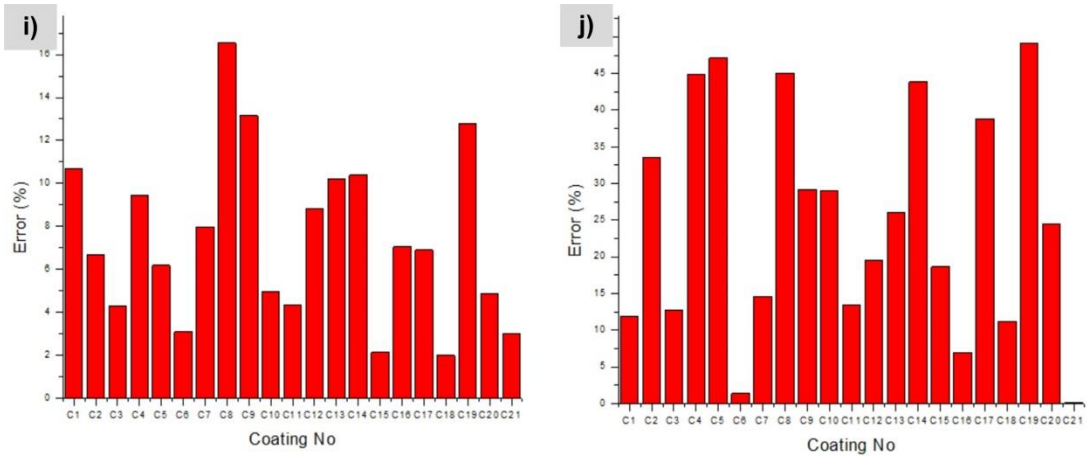

Figure 5.5: Graphical representation of Error % of estimated properties a) Density b) Weight Loss c) Change in enthalpy d) Thermal conductivity e) Thermal diffusivity f) Specific heat g) Contact angle h) Surface tension i) Adhesion energy j) Spreading area

5.2 Phase and structural analysis of electrode coatings

X-ray diffraction analysis (XRD) was performed to confirm the crystalline behavior of different coating compositions. XRD also helps to identify the different compounds existing in given compositions. Fourier Transform Infrared Spectroscopy (FTIR) was performed for all the coating compositions to observe the infrared absorption spectra. This technique enables the detection of various bonds among the different elements. XRD plots of coating compositions C3, C8, C12, and C16 are shown in Figure 5.6a. Significant peaks were observed at the same 2θ, and the oxide phases were identified as calcite ($CaCO_3$), Fluorspar (CaF_2), Silica (SiO_2), Calcinated Bauxite (Al_2O_3), and Rutile (TiO_2). These minerals were identified as per the coating compositions developed. FTIR spectra (Figure 5.6b) of different coating compositions were plotted and observed the stretching vibration region of $[SiO_4]^{4-}$ (tetrahedral symmetric stretching vibration) between the region 800 cm^{-1} to 1100 cm^{-1}. $[AlO_4]^{5-}$ (tetrahedral asymmetric vibration) were identified between the region 600 cm^{-1} to 800 cm^{-1}. When there is an increase in the network forming oxides, the amount of non-bridging oxygen (NBO) increased and affects the stabilization of the network structure. Due to the electrostatic force of attraction, silicate anions (SiO_4^{4-}) tend to develop a bond with the network modifiers (Al^{3+}) (Kim et al., 2015). The electrostatic forces between the two types of non-bridging oxygen decrease with the addition of CaO, K_2O, and BaO network breaker elements, which decreases the thermo-physical properties (Rada et al., 2008).

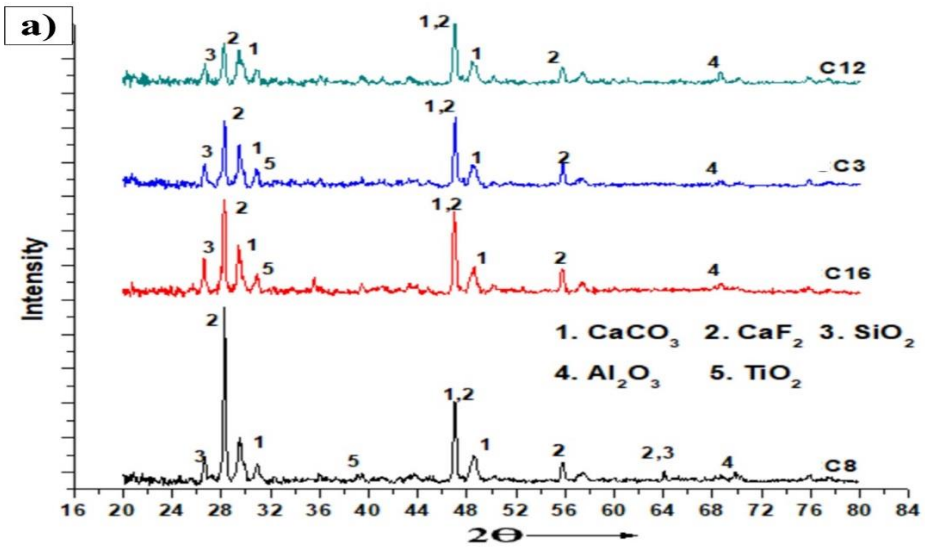

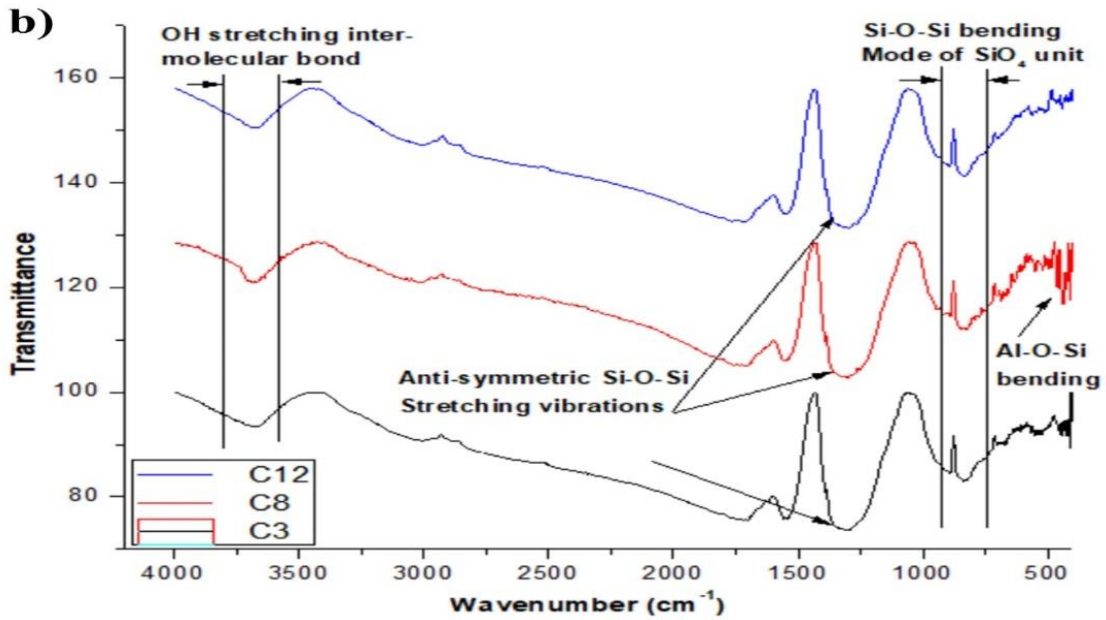

Figure 5.6: a) XRD analysis of coating compositions b) FTIR spectra for coating compositions

5.3 Multipass bead on plate analysis (ER90S-B3 based electrodes)

5.3.1 Qualitative analysis with bead chemistry and microhardness

Multipass weld beads were deposited on the P22 base plate using ER90S-B3 core wire-based laboratory-developed twenty-one set of electrodes. Visual observations were performed during the deposition of the multi-pass weld beads. It was observed that coating mixtures containing a higher amount of silica and calcinated bauxite with a lower amount of fluorspar lead to better slag detachability, arc stability, lower smoke, and weld quality. Qualitative observations for all the weld beads were recorded to analyze the behavior of each electrode coating. The beads possessing better qualitative observations are presented in the Table 5.6. The beads which show poor qualitativive observations are not shown in Table 5.6. Chemical analysis results for all the deposited welds are presented in Table 5.7, along with microhardness values. Qualitative observations for all the weld beads were recorded to analyze the behavior of each developed electrode. After depositing the weld beads, the base plate was strike 3 times with a hammer to estimate the slag detachability behavior. The previous literature suggests that rutile generally improves the slag detachability in the welding fluxes, while fluorites decrease the slag detachability (Jindal et al., 2013, 2014; Bhandari et al., 2016a, 2016b). From Table 4.4 and Table 5.6, the electrode coatings having a higher basicity index (> 3.25) possesses poor slag detachability with an irregular bead appearance. Porosity was also observed in the welds that are having poor slag detachability. Electrode coatings with a low basicity index (< 3) possess a better bead profile with improved slag detachability. Figure 5.7 presents the comparison of beads with a difference in bead appearance and slag detachability. Microhardness testing was performed to evaluate the mechanical behavior of these welds. As the microhardness of steel P22 was 210 Hv and for P91 is around 260 Hv, so welds should have matching microhardness value for better performance. Table 5.7 presents the major alloying elements detected in each weld. Cr and Mo are significant alloying elements that play an essential role in high-temperature applications by providing better mechanical and corrosion resistance properties. Welds beads deposited using coating electrodes C2 and C18 possess better weld quality, bead appearance, slag detachability, and higher wt.% of alloying elements. These welds were also free from porosity and produced less smoke as compared to other electrodes.

Table 5.6: Qualitative analysis of deposited weld beads

	Slag detachability	**Porosity**	**Bead appearance**	**Arc stability**
C2.	Good	No	Good	Good
C5.	Average	No	Average	Good
C6.	Good	No	Average	Good
C10.	Good	No	Average	Good
C12.	Good	No	Average	Average
C14.	Average	No	Average	Average
C15.	Good	No	Average	Good
C17.	Average	No	Good	Average
C18.	Good	No	Good	Good
C20.	Good	No	Good	Average
C21.	Good	No	Good	Good

Table 5.7: Chemical analysis of weld beads (wt. %) and microhardness

	C	**Si**	**Mn**	**S**	**Cr**	**Mo**	**Ni**	**Microhardness (Hv)**
C1.	0.05	0.24	0.25	0.019	1.97	0.962	0.05	256
C2.	0.059	0.26	0.27	0.013	2.14	1.03	0.04	240
C3.	0.06	0.25	0.29	0.013	1.88	0.966	0.04	256
C4.	0.06	0.24	0.29	0.013	1.88	0.988	0.04	250
C5.	0.06	0.22	0.29	0.012	2.05	0.96	0.1	256
C6.	0.06	0.23	0.31	0.013	2.08	1.01	0.04	217
C7.	0.058	0.21	0.24	0.013	1.75	0.881	0.1	264
C8.	0.063	0.31	0.25	0.016	1.78	0.921	0.1	268
C9.	0.06	0.25	0.27	0.010	2.15	0.919	0.039	222
C10.	0.08	0.20	0.23	0.012	1.56	0.81	0.03	217
C11.	0.07	0.26	0.29	0.012	2.03	0.962	0.04	238
C12.	0.062	0.28	0.25	0.015	1.89	0.965	0.03	255
C13.	0.07	0.31	0.27	0.020	1.70	0.843	0.13	265
C14.	0.05	0.27	0.32	0.027	1.91	0.871	0.13	255
C15.	0.07	0.23	0.25	0.021	1.77	1.01	0.06	253
C16.	0.06	0.28	0.25	0.017	1.86	0.93	0.03	239
C17.	0.07	0.34	0.40	0.030	2.15	1	0.05	243
C18.	0.05	0.29	0.27	0.019	2.01	0.986	0.03	241
C19.	0.057	0.26	0.35	0.023	1.94	0.97	0.06	276
C20.	0.04	0.25	0.33	0.017	1.94	0.95	0.1	247
C21.	0.06	0.27	0.31	0.013	2.01	0.965	0.04	223

Note: C – Carbon, Si – Silicon, Mn – Manganese, S – Sulphur, Cr – Chromium, Mo – Molybednum, Ni - Nickel

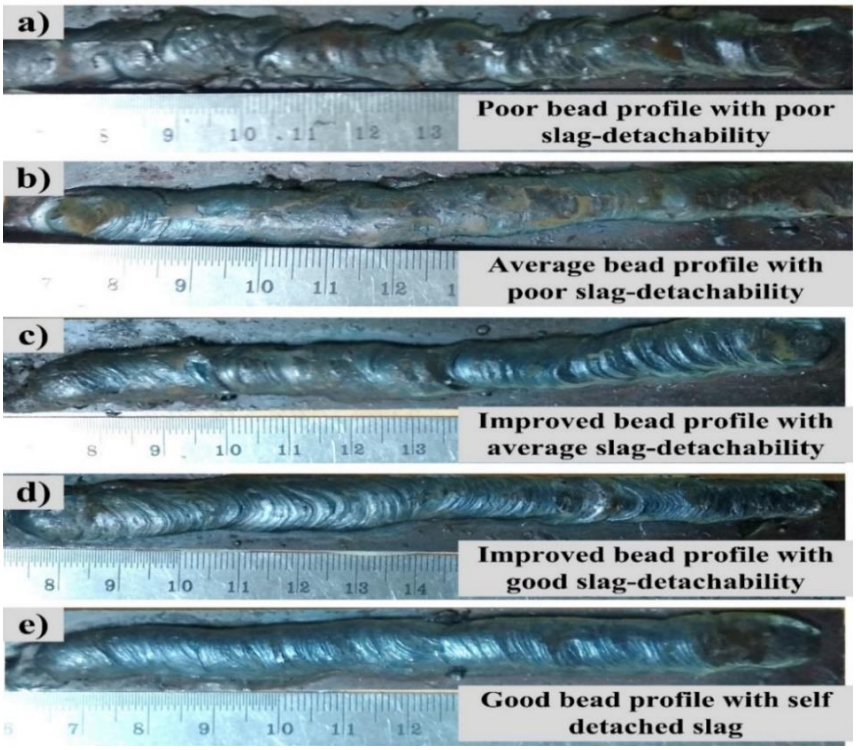

Figure 5.7: Multipass bead on plate for developed coating compositions a) C4 b) C16 c) C14 d) C20 e) C2

5.3.2 Development of Regression models and regression analysis for weld bead chemistry and Vickers's Microhardness

The weld chemistry of the deposited beads along with microhardness is shown in Table 5.7. The linear, quadratic or cubic regression models of these weld responses have been developed in terms of percentage compositions of individual electrode coating ingredients along with their binary and tertiary mixtures are given below in Eq. 5.16 to 5.21:

%C = 5.25743 x 10^{-3} CaO - 3.1907 x 10^{-3} CaF_2 + 6.81171 x 10^{-3} SiO_2 - 0.092640 Al_2O_3 + 2.47179 x 10^{-3} $CaF_2.Al_2O_3$ **(5.16)**

%Si = 0.011353 CaO - 3.43565 x 10-3 CaF_2 + 0.012290 SiO_2 + 3.8429 x 10^{-3} Al_2O_3 **(5.17)**

%Mn = -0.087037 CaO - 0.069939 CaF_2 - 3.60553 x 10^{-3} SiO_2 - 0.17487 Al_2O_3 + 4.65432 x 10^{-3} $CaO.CaF_2$ - 4.22828 x 10^{-3} $CaO.SiO_2$ + 8.04382 x 10^{-3} $CaO.Al_2O_3$ + 4.14513 x 10^{-3} $CaF_2.SiO_2$ + 4.26070 x 10^{-4} $CaF_2.Al_2O_3$ + 5.0947 x 10^{-3} SiO_2. Al_2O_3 **(5.18)**

%Cr = -0.78303 CaO - 0.18108 CaF_2 + 1.73963 SiO_2 - 0.32561 Al_2O_3 + 0.02791 $CaO.CaF_2$ - 0.02052 $CaO.SiO_2$ + 0.02587 $CaO.Al_2O_3$ - 0.02895 $CaF_2.SiO_2$ - 7.97263 x 10^{-3} $CaF_2.Al_2O_3$ + 0.024837 SiO_2. Al_2O_3 **(5.19)**

%Mo = -0.37377 CaO - 0.059665 CaF_2 + 0.37188 SiO_2 - 0.12513 Al_2O_3 + 0.01124 $CaO.CaF_2$ + 7.2258 x 10^{-3} $CaO.SiO_2$ + 3.30985 x 10^{-3} $CaO.Al_2O_3$ - 0.010288 $CaF_2.SiO_2$ + 5.06178 x 10^{-3} $CaF_2.Al_2O_3$ - 1.42309 x 10^{-4} SiO_2. Al_2O_3 **(5.20)**

H_v = 566.69256 CaO + 57.16674 CaF_2 + 873.44242 SiO_2 + 939.12967 Al_2O_3 - 14.2663 $CaO.CaF_2$ - 61.19313 $CaO.SiO_2$ - 72.23664 $CaO.Al_2O_3$ - 15.40532 $CaF_2.SiO_2$ - 1.20568 $CaF_2.Al_2O_3$ - 31.47587 SiO_2. Al_2O_3 + 1.07941 $CaO.CaF_2.SiO_2$ + 0.71449$CaO.CaF_2.Al_2O_3$ + 4.17803 $CaO.SiO_2.Al_2O_3$ - 1.80638 $CaF_2.SiO_2.Al_2O_3$ **(5.21)**

The regression analysis was performed and the results are presented in Table 5.8.

Table 5.8: ANOVA results of regression models for various weld responses

	Source	Sum of squares	DOF	Mean square	F value	P value	Status	R^2 value
%C	Model	4.840E-004	4	1.210E-004	2.79	0.0335	S	**0.86**
	Linear Mixture	2.389E-004	3	7.964E-005	1.23	0.3326	NS	
	CaF_2. Al_2O_3	2.450E-004	1	2.450E-004	7.43	0.0199	S	
	Residual	1.039E-003	16	6.495E-005				
	Total	1.523E-003	20					
%Si	Model	7.277E-003	3	2.426E-003	5.65	0.0421	S	**0.91**
	Linear Mixture	7.277E-003	3	2.426E-003	5.65	0.0421	S	
	Residual	0.016	17	9.160E-004				
	Total	0.023	20					
%Mn	Model	8.944E-003	9	9.938E-004	3.25	0.0319	S	**0.92**
	Linear Mixture	3.837E-003	3	1.279E-003	1.11	0.3868	NS	
	$CaO.CaF_2$	7.304E-004	1	7.304E-004	0.63	0.4430	NS	
	$CaO.SiO_2$	6.028E-004	1	6.028E-004	0.52	0.4848	NS	
	$CaO.Al_2O_3$	2.326E-003	1	2.326E-003	2.02	0.1832	NS	
	$CaF_2.SiO_2$	5.793E-004	1	5.793E-004	5.66	0.0393	S	
	$CaF_2.Al_2O_3$	6.527E-006	1	6.527E-006	0.005	0.9414	NS	
	$SiO_2.Al_2O_3$	9.333E-004	1	9.333E-004	4.81	0.0476	S	
	Residual	0.013	11	1.153E-003				
	Total	0.022	20					
%Cr	Model	0.20	9	0.022	3.85	0.0399	S	**0.85**
	Linear Mixture	0.069	3	0.023	0.89	0.4772	NS	
	$CaO.CaF_2$	0.026	1	0.026	5.23	0.0336	S	
	$CaO.SiO_2$	0.014	1	0.014	0.55	0.4753	NS	
	$CaO.Al_2O_3$	0.024	1	0.024	4.99	0.0356	S	
	$CaF_2.SiO_2$	0.028	1	0.028	1.09	0.3194	NS	
	$CaF_2.Al_2O_3$	2.285E-003	1	2.285E-003	6.87	0.0277	S	
	$SiO_2.Al_2O_3$	0.022	1	0.022	0.85	0.3754	NS	
	Residual	0.29	11	0.026				
	Total	0.48	20					
%Mo	Model	0.021	9	2.312E-003	3.31	0.0328	S	**0.93**
	Linear Mixture	9.862E-003	3	3.287E-003	4.70	0.0239	S	
	$CaO.CaF_2$	4.259E-003	1	4.259E-003	6.09	0.0312	S	
	$CaO.SiO_2$	1.759E-003	1	1.759E-003	2.52	0.1410	NS	
	$CaO.Al_2O_3$	3.939E-004	1	3.939E-004	0.56	0.4687	NS	
	$CaF_2.SiO_2$	3.569E-003	1	3.569E-003	5.10	0.0452	S	
	$CaF_2.Al_2O_3$	9.212E-004	1	9.212E-004	1.32	0.2754	NS	
	$SiO_2.Al_2O_3$	7.282E-007	1	7.282E-007	5.95	0.0395	S	
	Residual	7.691E-003	11	6.992E-004				
	Total	0.028	20					
	Model	1173.75	13	90.29	3.60	0.0285	S	
	Linear Mixture	72.64	3	24.21	0.15	0.9280	NS	

H_v	$CaO.CaF_2$	0.26	1	0.26	1.61	0.9691	NS	**0.90**
	$CaO.SiO_2$	217.00	1	217.00	1.32	0.2880	NS	
	$CaO.Al_2O_3$	24.90	1	24.90	9.15	0.0151	S	
	$CaF_2.SiO_2$	170.64	1	170.64	1.04	0.3419	NS	
	$CaF_2.Al_2O_3$	47.73	1	47.73	8.58	0.0192	S	
	$SiO_2.Al_2O_3$	12.48	1	12.48	11.69	0.0049	S	
	$CaO.CaF_2.SiO_2$	16.04	1	16.04	0.098	0.7637	NS	
	$CaO.CaF_2.Al_2O_3$	7.47	1	7.47	0.046	0.8371	NS	
	$CaO.SiO_2.Al_2O_3$	255.52	1	255.52	1.56	0.2523	NS	
	$CaF_2.SiO_2.Al_2O_3$	47.76	1	47.76	0.29	0.6063	NS	
	Residual	1148.96	7	164.14				
	Total	2322.70	20					

In the Table 5.8, the R^2 values for all properties are approaches to unity and it predicts that the response models fit better to the actual data and show less difference between the predicted and actual values. The variations of predicted values from actual values for various properties are shown in Figure 5.8.

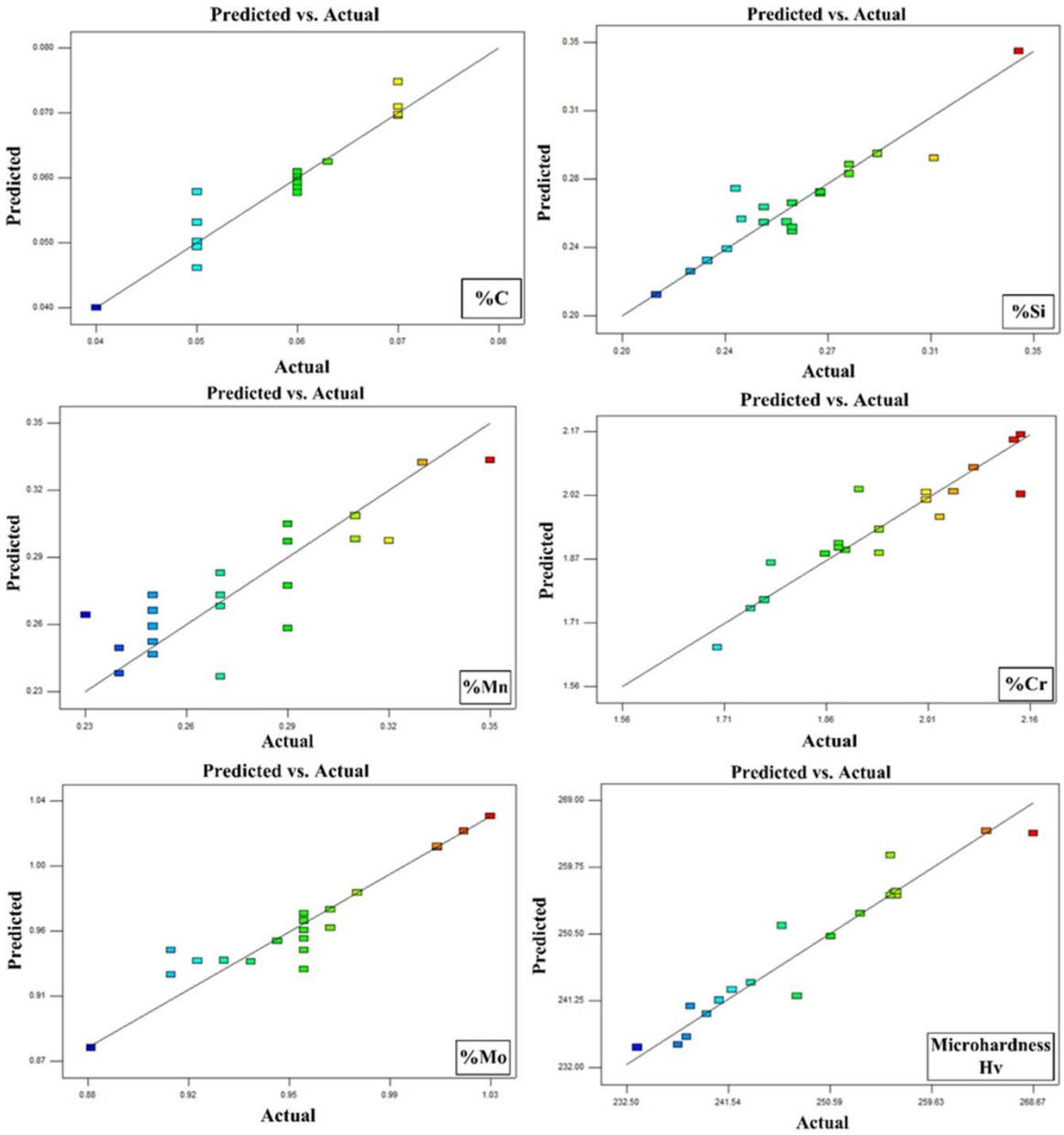

Figure 5.8: Predicted vs. actual plots of various weld responses

5.3.3 Effect of coating ingredients and their interactions on weld bead chemistry and microhardness

5.3.3.1 Effect of electrode coating ingredients on weld chemistry

Literature reveals that increasing the weld carbon content increases hardenability, so as the weld cools, it can effectively be quenched, resulting in a hard, brittle phase in the HAZ. Hardened steel also has a slightly lower density than unhardened, which can cause distortion, residual stresses, and crack. The carbon content in the weld should be lesser than the parent metal or filler metal for better weldability and weld quality (Mitra et al., 1991). With the increase in oxygen concentration in the weld, the transfer of carbon from the weld to slag increases. Basicity of the flux system significantly affects the oxygen content in the welds (North et al., 1978; Davis et al., 1991). From Table 4.2 and Table 5.7, the carbon content found in all the welds was lesser than the carbon content present in filler wire. A mathematical regression model was developed and using ANOVA (F-test) the effect of different coating ingredients and their interaction were estimated (Table 5.8). It was observed that individual constituents do not have any significant effect on the carbon content. The significant increasing effect of binary mixture $CaF_2.Al_2O_3$ was seen on the carbon content in the weld, while other binary components do not affect the carbon content in the weld. Coating compositions with a higher basicity index cause lower weld carbon content than the coating mixtures with a lower basicity index. SiO_2 and CaO decompose during the arc welding process and releases oxygen, which reacts with carbon (present in filler wire and base metal) to form oxides and results in a reduction of carbon content in the weld.

Individual ingredients CaO, SiO_2 and Al_2O_3 of the electrode coating have a significant increasing effect on the Si content of the welds. But from the previous literature, it can be seen that the activity of SiO_2 in the slag-metal reaction by CaO decreased due to the formation of SiO_4^{4-} complex ions (Bhandari et al., 2016a). An increase in the silica content in the electrode composition leads to an increase in the silicon content in the welds. SiO_2 is also known for its capability to enhance slag detachability in welds, which improves the weld quality.

The manganese content in all the welds was found to be in the range of 0.23-0.4 wt% as compared to Mn present in the filler wire (0.61wt%). In general, the concentration of Mn present in filler wire impacts the transfer of weld pool manganese content (Mitra et al., 1991). The manganese is transferred from the weld metal to slag with the addition of CaF_2 content in the electrode coatings (Bhandari et al., 2016a). Binary mixtures $CaF_2.SiO_2$ and $SiO_2.Al_2O_3$ are the only mixtures that have significant increasing effect on the manganese content in the weld shown by regression analysis (Table 5.8 and Table A2). Other binary mixture components do not impact the weld metal manganese significantly. Electrode compositions with a higher basicity index possess more manganese content, which decreases the transfer of manganese from weld to slag, so it is better to use coating mixtures with high basicity index for better weld properties (Davis et al., 1991).

Cr content of filler wire and parent materials impact the Cr content present in the welds. All the welds have lower Cr content as compared to filler wire (Cr = 2.52); this is due to the dissociation of SiO_2. When SiO_2 dissociates, it increases the availability of free oxygen which, causes the oxidation of chromium to form chromium oxide. Higher Cr content in the welds is essential in applications where the corrosion resistance of the weld plays an important role. From the regression analysis (Table 5.8 and Table A2), it can be seen that individual coating ingredients do not play any significant effect on the Cr content. $CaO.CaF_2$, $CaO.Al_2O_3$ and $CaF_2.Al_2O_3$ binary mixtures have a significant increasing effect on the Cr content, while the other mixtures containing SiO_2 have a significant decreasing effect on the Cr content of the welds.

Molybdenum has a high oxygen affinity due to which it can form oxides and other nonmetallic inclusion which, affects the microstructural and mechanical properties of the alloy. Molybdenum primarily increases the corrosion resistance of the alloys when added in a limited amount. From the regression analysis, the SiO_2 indivisually has significant increasing effect on

the Mo content of the weld and other indiviasual constituents have significant decresing effect on the weld metal Mo content. The binary components $CaO.Al_2O_3$, $CaF_2.Al_2O_3$, and $SiO_2.Al_2O_3$ have significantly decresing effect on the Mo content.

5.3.3.2 Effect of coating on the microhardness of different weld

Higher the carbon equivalent higher is the hardness of the weld, which leads to the susceptibility of cold cracking with higher carbon equivalent (Lancaster et al., 1980). The binary mixtures of SiO_2 shows a decreasing trend by increasing the oxygen level in the weld pool, which further combines with carbon to form its oxides. SiO_2 causes the decrease in manganese and carbon content in the weld therby decreasing microhardness. The regression analysis (Table 5.8 and Table A2) shows the significant decreasing effect of binary mixtures $CaO.Al_2O_3$, $CaF_2.Al_2O_3$ and $SiO_2.Al_2O_3$ on the observed microhardness values. $SiO_2.Al_2O_3$ is a very effective binary mixture that has a significant decreasing effect on the average weld microhardness with higher F value (11.69) as shown in Table 5.8.

5.3.3.3 Contour plots of various weld responses

The contour plots depict values of various investigated properties for different proportions of electrode coating ingredients, as shown in Figure 5.9. The variation of a particular property response with respect to electrode coating ingredients can be easily observed from these plots.

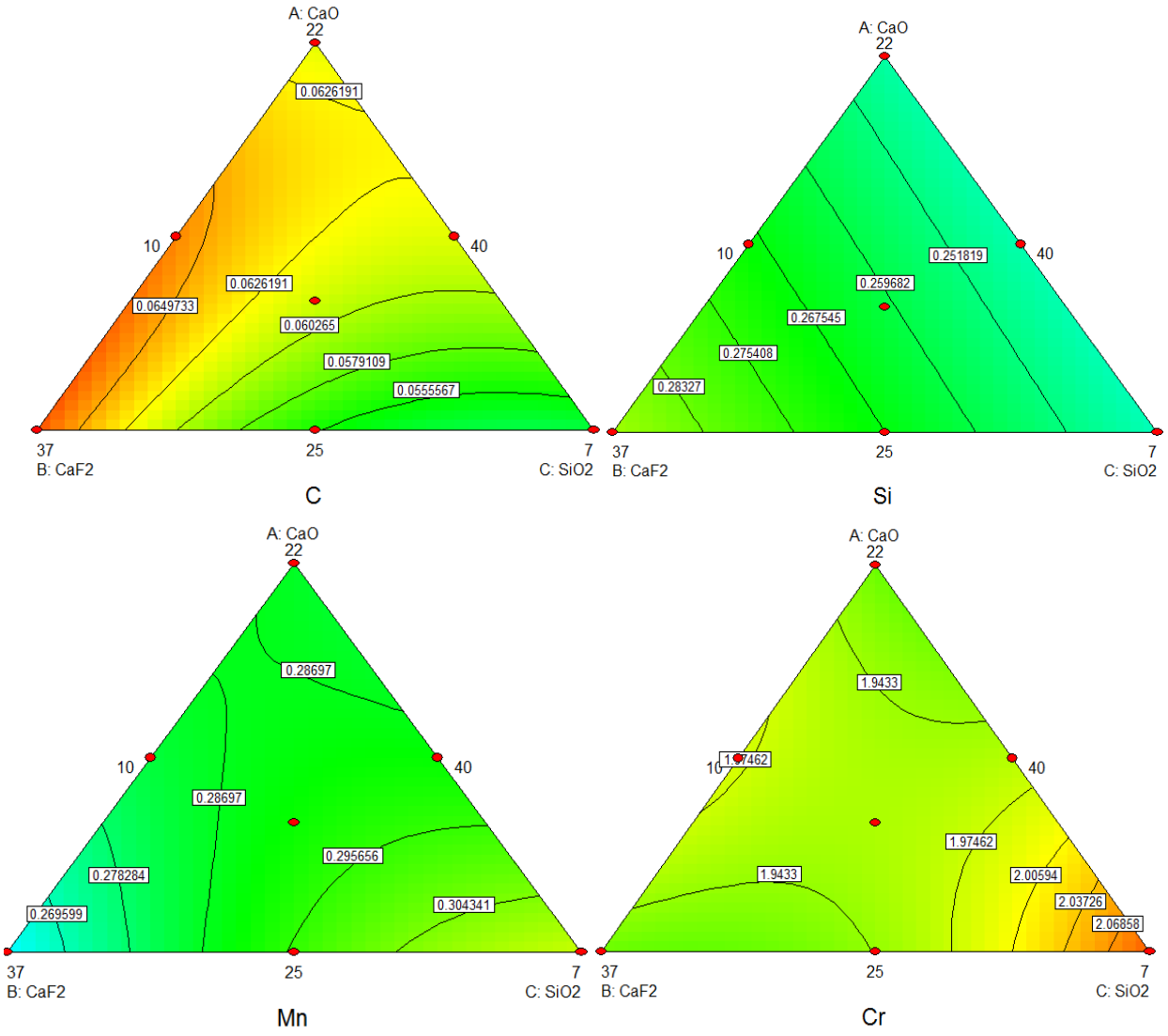

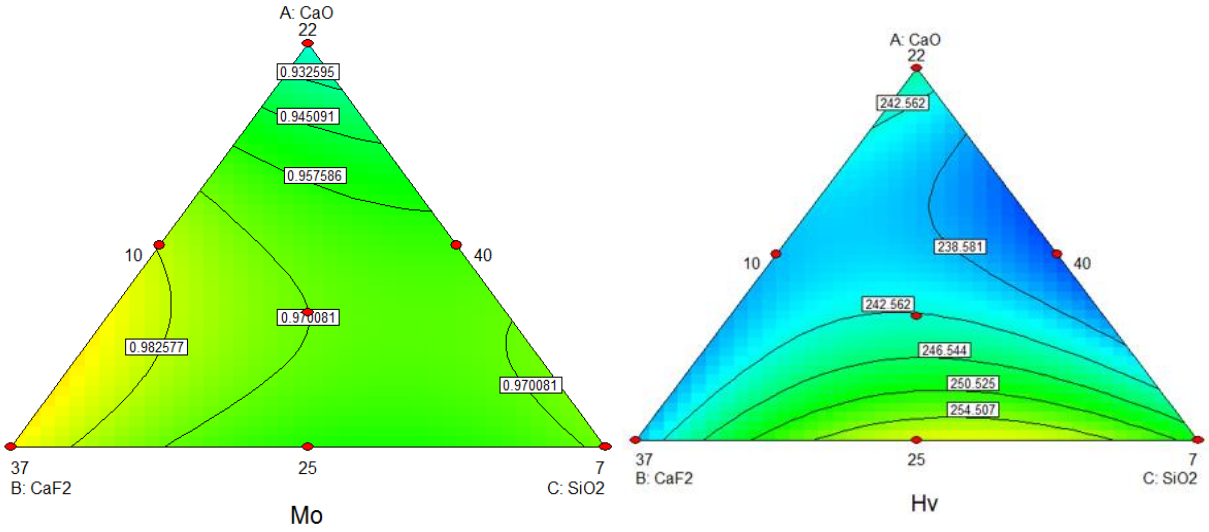

Figure 5.9: Contour surface plots

5.3.4 Model validation and multi objective optimization

The developed regression model of various properties was validated using four randomly selected electrode coatings for conducting the confirmatory experiments. The experimental results, along with the predicted values, are summarized in Table 5.9. From Table 5.9, it was observed that error (%) for C, Si, Cr, Mo and microhardness property response are less than 5%, while Mn shows an error of more than 5%, in two of the solutions out of 4 solutions. The optimization of elements (carbon, silicon) in the weld, maximizing the elements (chromium, molybdenum), and keeping microhardness in a range developed as a nonlinear, multivariable and multiobjective optimization problem. The complex desirability optimization method proposed by Derringer et al., 1980 was used to optimized these properties. In this study, the problem is to improve the microhardness and weld chemistry. Optimized solutions were presented in Table 5.10.

Table 5.9: Error (%) in chemical composition of multi-pass bead on plate for C, Si, Mn, Cr, Mo and Hv

Coating mixture				Predicted value				Actual value				Error %			
CaO	**CaF_2**	**SiO_2**	**Al_2O_3**	**C**	**Si**	**Mn**	**Cr**	**C**	**Si**	**Mn**	**Cr**	**C**	**Si**	**Mn**	**Cr**
25	40	5	5	0.0569	0.227	0.305	2.071	0.06	0.23	0.31	2.08	5.44	1.29	1.63	0.43
23.5	40	8.5	3	0.0417	0.2452	0.289	1.95	0.05	0.27	0.31	2.01	19.9	10.11	6.96	3.03
25	35	10	5	0.0467	0.303	0.266	1.855	0.05	0.29	0.27	2.01	7.06	4.29	1.17	8.35
25	39	10	1	0.0668	0.2826	0.250	1.809	0.07	0.31	0.27	1.7	4.79	9.69	7.65	6.02

Predicted value		Actual value		Error %	
Mo	**Hv**	**Mo**	**Hv**	**Mo**	**Hv**
1.011	237.29	1.01	239.58	0.09	0.96
0.948	234.63	0.965	237.04	1.79	1.02
0.992	239.79	0.986	243.54	0.6	1.56
0.953	264.72	0.965	246.28	1.21	6.96

Table 5.10: Optimum electrode coating composition for chemical composition and microhardness of weld deposits

S.No.	CaO	CaF_2	SiO_2	Al_2O_3	C	Si	Mn	Cr	Mo	H_v	Desirability
1	25	35	10	5	0.046	0.30	0.26	2.09	0.99	242.81	0.84
2	22.5	37.5	10	5	0.055	0.26	0.27	2.09	1.01	250.39	0.66

Note: C – Carbon, Si – Silicon, Mn – Manganese, Cr – Chromium, Mo – Molybednum, Hv – Microhardness

5.4 Multipass bead on plate analysis (Inconel-82 based electrodes)

Weld beads were deposited on the low alloy steel plate using twenty-one laboratory-developed electrodes. It was concluded that coating mixtures having a higher amount of silica and calcinated bauxite with a lower amount of fluorspar leads to better slag detachability, arc stability, lower smoke, and weld quality. In this investigation, chemical analysis results for all the deposited weld deposits are presented in Table 5.11, along with qualitative observations and microhardness values. Qualitative observations for all the weld beads were recorded to analyze the behavior of each developed electrode. After depositing the weld beads, the base plate was strike three times with a hammer to estimate the slag detachability behavior. It was reported that rutile generally improves the slag detachability in the welding fluxes, while fluorites decrease the slag detachability. However, it has also been reported that fluorites improve the slag detachability in basic flux system of nickel wire-based electrodes, but does not in the acidic flux systems (Qin et al., 2013; Sham et al., 2014; Wang et al., 2016). The slag detachability of nickel wire-based electrodes was observed to be a little poor as compared to the low alloy steel electrodes. Microhardness testing was performed to evaluate the mechanical behavior of these welds. As microhardness of the SS304L base is around 200 Hv and for P91 base is around 245 Hv, so welds with matching microhardness is required for the better weld properties. Table 5.11 presents the major alloying elements detected in each weld. Cr and Ni are the major alloy elements that play an essential role in high-temperature applications by providing better mechanical properties and corrosion resistance in corrosive environments. Welds made with electrodes C7 and C16 (Figure 5.10) possess better weld quality, bead appearance, slag detachability, and higher wt. % of alloying elements. These welds were also free from porosity and produced less smoke as compared to other electrodes with better mechanical properties.

Table 5.11: Chemical and qualitative analysis of deposited welds with microhardness

	Cr (wt.%)	**Ni (wt.%)**	**Fe (wt.%)**	**Nb (wt.%)**	**Hv**	**SD**	**Porosity**	**BA**	**AS**
C2	16.2	64.58	16.69	1.4	191.99	Good	No	Good	Good
C4	15.8	61.83	17.13	1.71	194.67	Average	No	Average	Poor
C7	16.94	66.93	12.18	1.6	189.63	V good	No	Good	Good
C8	16.45	60.29	15.68	1.8	185.62	Average	No	Average	Good
C9	16.43	65.2	15.01	1.3	176.77	Average	No	Average	Good
C10	15.71	65.5	15.26	1.37	190.76	Good	No	Good	Good
C11	15.84	63.85	17.01	1.25	187.27	Good	No	Good	Good
C12	15.45	60.85	20.45	1.52	160.04	Good	No	Good	Good
C15	16.95	67.58	12.32	1.4	165.69	Average	No	Average	Good
C16	17.1	66.42	12.5	1.62	190.2	V good	No	Good	Good
C17	16.32	66.51	13.12	1.73	184.42	V good	No	Average	Poor
C18	15.48	62.81	16.72	1.85	184.58	V good	No	Good	Good
C19	16.71	64.18	16.21	1.47	188.63	Good	No	Average	Good

Note: Hv - Microhardness, SD – Slag Detachability, BA – Bead appearance, AS – Arc stability

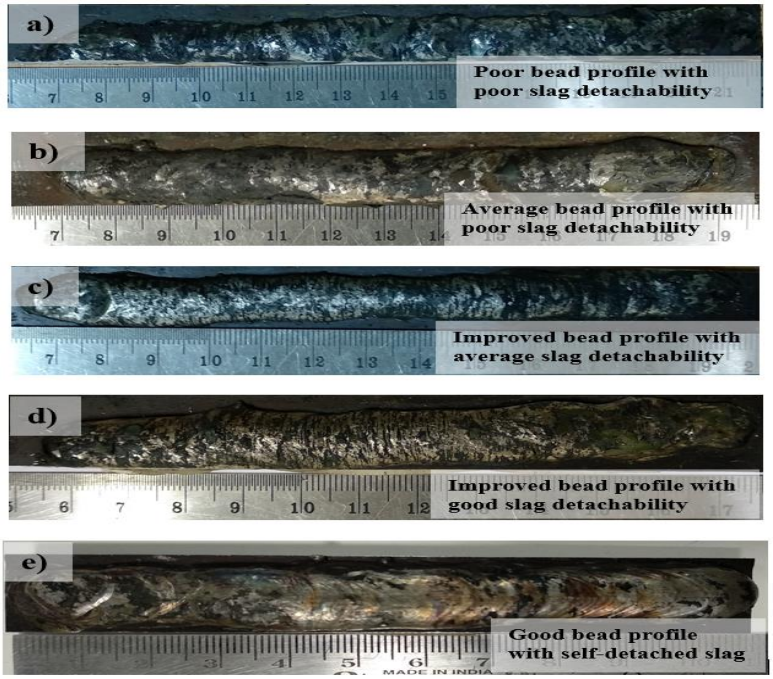

Figure 5.10: Multipass bead on plate for developed coating compositions a) C5 b) C13 c) C15 d) C2 e) C7

5.5 Selection of electrodes to fabricate P22/P91 and P91/SS304 dissimilar welds

Multipass bead on plate analysis was performed with the ER90S-B3 and IN-82 based electrodes. Qualitative analysis along with multiobjective optimization was performed to evaluate the performance of a twenty-one set of developed electrodes with each core wire (ER90S-B3 and IN-82). After analyzing the different properties, it was concluded that the ER90S-B3 electrode prepared using coatings C2 and C18 fair out better amongst all the twenty-one coated electrodes. Similarly, after analyzing the qualitative analysis for multipass beads deposited using nickel-based electrodes, the electrodes prepared using C7 and C16 fair out better amongst all the twenty-one nickel-based electrode coatings. In this work, ferromanganese, ferrosilicon, ferrochrome and ferrotitanium powders were used as deoxidizers. The welding pretrials were performed after adding small proportions of these deoxidizers. The addition of these deoxidizers not only improves the cleanliness of the final weld but also improves the weld quality and appearance. Table 5.12 and Table 5.13 shows the modified electrode coatings to fabricate P22/P91 and P91/SS304L dissimilar joints, respectively.

Table 5.12: Modified electrode coatings to fabricate P22/P91 dissimilar weld

Coating No.	**Electrode coating ingredients (wt.%)**								
	CaO	**CaF_2**	**SiO_2**	**Al_2O_3**	**TiO_2**	**Cr**	**Fe-Si**	**Fe-Mn**	**Binder**
E2M	20	27.5	12.5	7.5	12.5	7.5	2.5	2.5	Bal.
E18M	25	30	7.5	5	17	3	2.5	2.5	Bal.

Table 5.13: Modified electrode coatings to fabricate P91/SS304L dissimilar weld

Coating No.	**Electrode coating ingredients (wt.%)**									
	CaO	**CaF_2**	**SiO_2**	**Al_2O_3**	**TiO_2**	**Fe-Cr**	**Fe-Si**	**Fe-Mn**	**Fe-Ti**	**Binder**
E7M	18.5	25	10.0	7.5	20	5	2.5	2.5	2.5	Bal.
E16M	23.0	30.0	8.0	5.0	15	7.5	2.5	2.5	-	Bal.

5.6 Fabrication and characterization of P22/P91 dissimilar welds

5.6.1 Fabrication, preliminary inspections and weld chemistry

P22 and P91 plates were welded using a welding procedure discussed in section 4.4.7. Three different dissimilar welds of P22/P91 were prepared using the SMAW process by employing the laboratory-made electrodes E2M, E18M, and commercial electrode (E9018-B3). P22 and P91 are iron-based low alloy steels having a low percentage of carbon (<0.09 wt.%) with Cr and Mo as a significant constituent (Table 4.2). Filler wire (ER90S-B3) compatible with P22 alloy was used in this investigation due to its availability, low cost, and better mechanical properties. The chemical composition of fabricated welds is presented in Table 5.14.

Table 5.14: Chemical composition of P22/P91 welds fabricated using different electrodes **(wt.%)**

Welds	**C**	**Si**	**Mn**	**P**	**S**	**Cr**	**Mo**	**Ni**	**Fe**	**C_E**
CE	0.078	0.52	0.69	0.026	0.015	3	1.02	0.04	Bal.	1
E2M	0.02	0.27	0.46	0.019	0.019	4.01	0.88	0.1	Bal.	1.074
E18M	0.024	0.61	0.44	0.030	0.015	3.25	0.87	0.08	Bal.	1.126

Note: CE – commercial electrode; E2M – Modified electrode coating E2; E18M – Modified electrode coating E18 (Table 4.12); C_E – Carbon equivalent

The chemical compositions are measured on the atomic absorption spectroscope. The measurements were taken in the center of weld fusion zone on three points. As the dilution calculations were performed by assuming the 30% base dilution (15% each for both the base plates) and 70% filler dilution for the dissimilar weld using SMAW process. Table 4.2 presents the chemical compositions of base plates and filler metal used in this study. Table 5.14 presents the chemical composition of fabricated welds. By considering the dilution effect, the Cr content was estimated 3.412 wt. %. Cr content in E2M was observed as 4.01 wt. % which is higher because the addition of chromium powder in the coating and better weld recovery of Cr in laboratory developed electrode fabricated welds. The concentration of Mo and Mn was estimated and are comparable to the concentration estimated using atomic absorption spectrometry analysis. Mo was recovered well 0.88 and 0.87 wt. % in E2M and E18M welds. Similarly, the Mn was recovered 0.46 and 0.44 wt. % in both the E2M and E18M respectively. It was observed from the above calculations that weld element recovery and electrode coating compositions also play a significant role along with the dilution in deciding the final weld compositions.

It was observed that the welds fabricated with the laboratory-made electrode contain a low carbon wt.% (<0.024) as compared to the commercial electrode weld (= 0.078). Higher carbon content in the welded joint leads to higher hardness and hence makes it brittle. Higher hardness significantly increases the risk of cracking after welding, especially in the Heat Affected Zone. The weldability of steel depends upon many factors, of which carbon equivalent (C_E) is one of the significant factors. Usually, the C_E (IIW) for steels are somewhat around 0.4 wt.%. Steels having C_E 0.4% or above sometimes required PWHT. For Cr-Mo steels, post-weld heat treatment required as the base materials and welds having a C_E > 0.8%.

5.6.2 Weld microstructure investigation and analysis

A typical dissimilar weld consists of multiple zones, namely base metal, heat affected zone, and weld region. These zones show a significant change in microstructure, which yields differences in properties and their behavior. The macrograph and optical microstructures of different zones of P22/P91 dissimilar weld fabricated using laboratory-made electrodes E2M are shown in Figure 5.11, while for commercial electrodes (E9018-B3), is shown in Figure 5.12. The three regions of the weld are distinctively visible and showcase precipitation of different phases and grains within them. Five different regions are labelled on the macrograph presented in Figure 5.11 and Figure 5.12 with optical microstructures. Figure 5.11a shows the microstructure of P22 base metal, which consists of a predominantly tempered bainitic structure. A fine dispersion of carbides is found inside the ferrite grains. Comparing the base metals P22 and P91, it is evident

that P22 has coarser grains as compared to the P91 (Figure 5.11a and 5.11f). PWHT of welds has caused grain coarsening in the P22 region and it also accelerates the kinetics of the carbon migration occurring on the boundary of base and weld. The microstructure of the P22 base/weld interface (Figure 5.11b) exhibits a very fine region of grain coarsening in the heat-affected zone of P22, which is majorly caused by the base to weld carbon migration (Fuchs et al., 2010; Mayr et al., 2019; Sudha et al., 2006). Weld metal microstructure is composed of cast dendrites fully upper bainite structure (Figure 5.11c). The interface of the P91 base and the P22 matched filler weld is a mismatch region due to the significant difference in chromium concentration, which leads to a Cr-gradient across the weld boundary. It encourages carbon to migrate, which further leads to the formation of deleterious chromium carbides. There is a significant change of microstructure in regions close to the fusion zone (Figure 5.11d-5.11e). The grain size in the weld was coarsened. The carbon migration has taken place, and a lighter spot was observed in the carbon depleted zone due to the migration of carbon from weld towards P91. An area adjacent to the weld HAZ appears to be much darker due to the accumulation of carbon near the fusion line. The reduction of carbon in the weld interface makes the joint sensitive when exposed to cyclic stresses. This joint is susceptible to failure, majorly owing to the formation of a soft carbon depleted region. The post-weld heat treatment temperature, for P22/P91 weld, should be limited to 750°C. (Sultan et al., 2017).

Microstructures of different regions of dissimilar weld fabricated using commercial electrodes are shown in Figure 5.12. The microstructure of welds fabricated using laboratory-developed and commercial electrodes present a similarity in the weld region. This is majorly due to the same filler wire being used. The only difference is in the coating composition, which affects the weld region microstructure minimally, though, a significant difference is observed in the width of different zones. A broader area of carbon depleted soft zone was observed in the P22/weld interface (Figure 5.12b) in the case of commercial electrode fabricated weld. A higher width of the carbon depleted zone signifies greater migration across the weld boundary. The commercially fabricated weld has a higher content of carbon as compared to laboratory developed ones as per the weld metal chemistry investigations (Table 5.14). From Figure 5.12d-e, the grains observed at the Weld/P91 base interface were quite coarse in nature as compared to Figure 5.12d-e with a higher width of carbon depleted zone. An increase in the size of the grains at the weld interface in case of welds fabricated using commercial electrodes exhibits poor mechanical performance as compared to the laboratory-made electrode welds. A substantial increase in grain size results in inferior properties and can be detrimental for longer cycles or fatigue, as encountered in boiler operations over a long period.

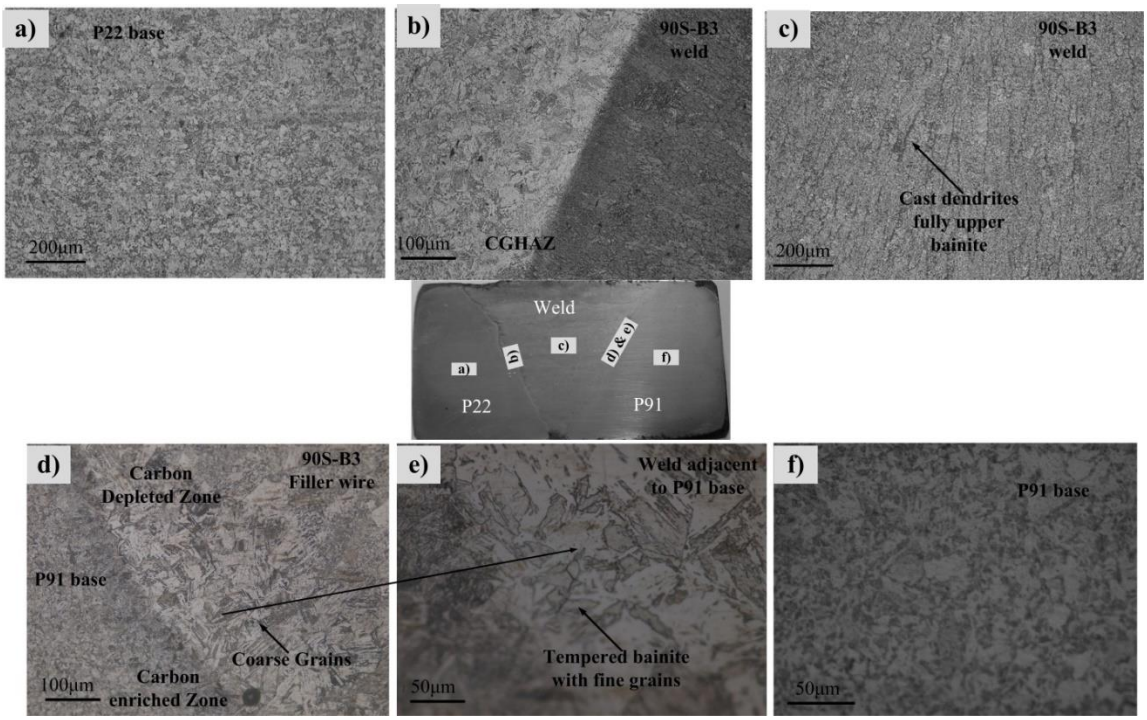

Figure 5.11: Microstructural examination of P22/P91 dissimilar weld fabricated using electrodes E2M a) P22 base metal b) Interface P22/Weld c) Weld metal d) Interface of weld/P91 e) Interface of weld/P91 (magnified) f) P91 base metal)

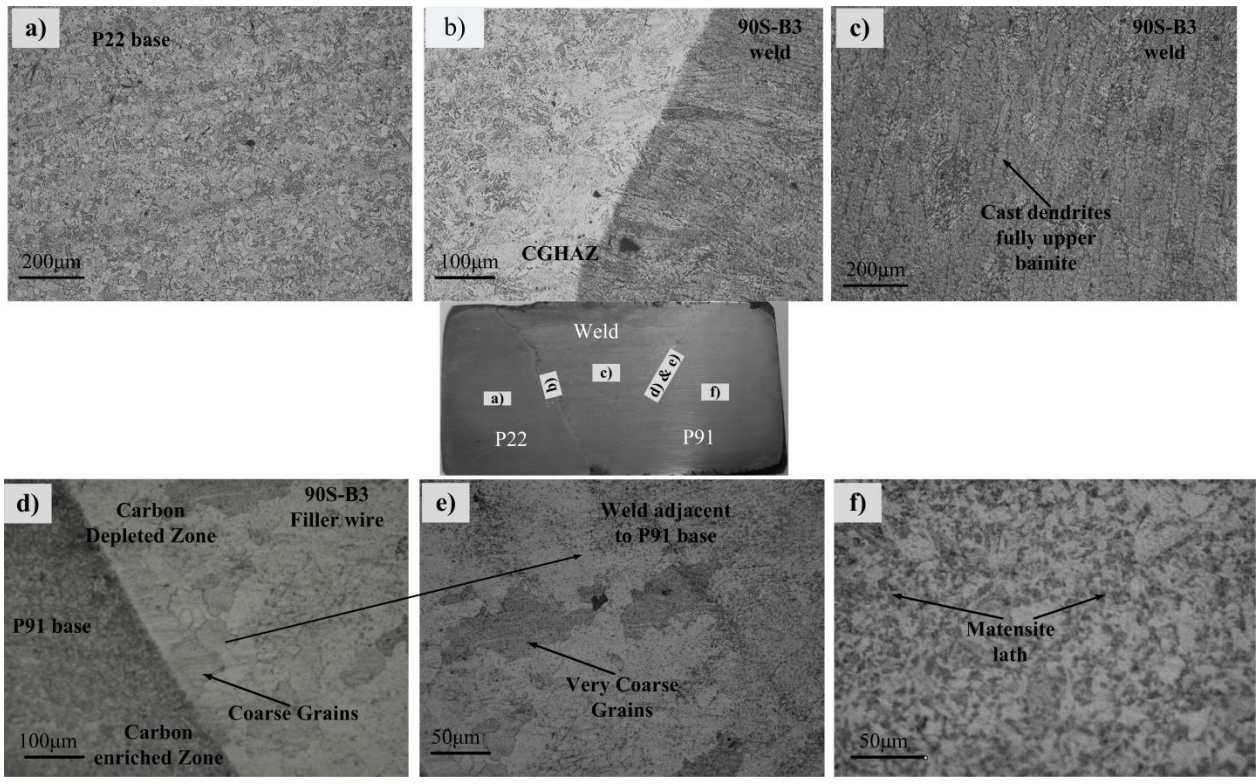

Figure 5.12: Micrographs of different regions of dissimilar weld using commercial electrodes CE a) P22 base metal b) Interface P22/Weld c) Weld metal microstructure d) Interface P91/Weld e) Interface of weld/P91 (magnified) f) P91 base metal

5.6.3 Comparison of weld`s mechanical behavior

Microhardness profile of P22/P91 dissimilar weld fabricated using laboratory-made electrodes E2M, E18M, and commercial electrode CE is shown in Figure 5.13. These observations were made after the post weld heat treatment of the welded specimens. The variations in the microhardness can be seen due to the presence of different metallurgical regions across the dissimilar welds. The average hardness of various regions of the different welds is shown in Table 5.15. When exposed to high temperatures, carbon diffuses from the low chromium side of the weld interface due to the activity gradient. As a result, the precipitates on this side start dissolving leading to a change of structure from bainite to ferrite. A P22 base metal exhibits the lowest hardness amongst all the welds. As moving from weld to the P91 base metal, the value of hardness increases due to the formation of brittle and hard martensite in the P91 near the fusion line. Larger grains near the fusion line of P91/weld was observed in the case of commercial electrode fabricated welds as compared to the E2M welds (Figure 5.11d and Figure 5.12d). Therefore, a sharp increase in the hardness was noticed due to the accumulation of carbon along the P91 fusion line. The maximum hardness of 254 Hv was observed in HAZ near the weld/P91 interface in case of commercial electrode weld while the lower values were observed in the laboratory-developed electrode welds. Previous studies recorded a very high value of hardness (> 400Hv) for P22/P91 dissimilar welds without performing post-weld heat treatments, which results in brittle welds and deteriorate the mechanical properties. Different post-weld heat treatments were performed by the researchers, and there was a noticeable drop in the microhardness values (Kulkarni et al., 2018; Sultan et al., 2016, 2017).

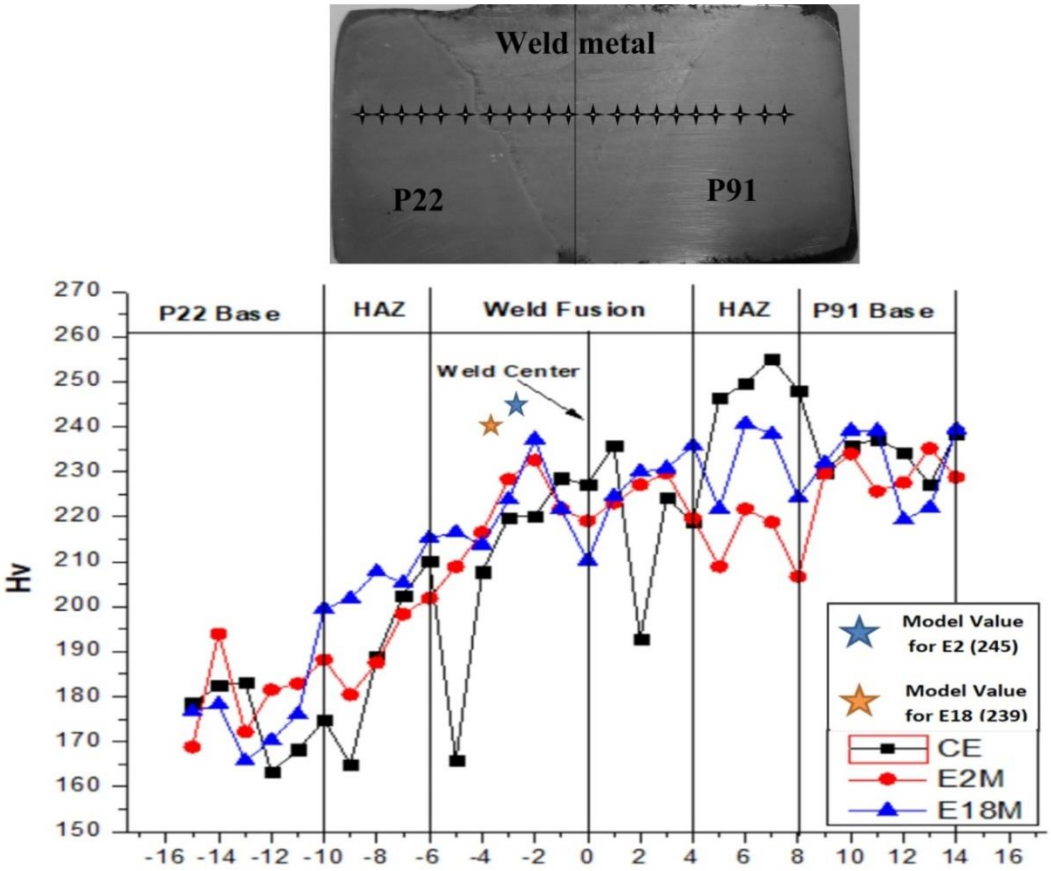

Figure 5.13: Microhardness profile of fabricated welds

Table 5.15: Average microhardness across different regions of the welds

	Base P22	HAZ P22	Weld	HAZ P91	Base P91
C.E	175±7	191±17	214±19	249±4	233±5
E2M	182±10	192±8	221±10	214±6	230±6
E18M	177±11	207±5	224±9	231±8	232±8

From Figure 5.13 and Table 5.15, the hardness profile of the welds fabricated using E2M electrodes was uniform, and no sharp change was observed. The welds fabricated using E2M coating weld has lower average microhardness as compared to the weld fabricated using E18M electrode coating. This is mainly because higher CaO content in the electrode coatings tends to increase hardness, while an increase in SiO_2 content reduces the hardness (Bhandari et al., 2016). Coating E18M has a higher CaO content of 25 wt.% as compared to 20 wt.% in E2M; moreover, the SiO_2 content of E18M is 5 wt.%, which is less as compared to 7.5 wt.% in E2M.

Tensile test fractured specimens of fabricated welds and respected stress vs strain diagrams are shown in Figure 5.14 and Figure 5.15. The value of ultimate tensile strength, yield strength, and percent elongation of transverse weld specimens are presented in Table 5.16. Maximum tensile strength {= 630.23 N/mm^2} was observed in the case of weld made with E2M electrodes. The tensile strength obtained in the case of electrodes E2M was higher than the P22 base and closer to the base metal P91, which is in agreement with the findings of previous researchers (Mayr et al., 2018). The mechanical properties of the welds depend upon the microstructure of the weld and chemical composition. Materials used in high-temperature applications require enhanced ductility and tensile properties. The fracture process is more complicated in the dissimilar weld as compared to similar welds. Previous studies reported that the fracture generally happened on the low alloy steel side. This generally happens due to the formation of the weaker and stronger zone because of carbon migration along the transition joint (Sultan et al., 2016, 2017; Hajiannian et al., 2013; Mittal et al., 2015; Sudha et al., 2006; Fuchs et al., 2010; Mayr et al., 2018; Maruyama et al., 2013). From Figure 5.14, all the tensile specimens fractured from the P22 base metal, which suggests that weld joints are stronger than the P22 base metal. It also reveals that the soft zone formed near the fusion line due to the carbon migration was not the weakest zone of the joint. Post weld heat treatment reduced the tensile strength and restored ductility due to the tempering of the base metal. Rathod et al. (2015, 2016a) suggested that the weld strength mismatch has a strong influence on the crack driving force and crack growth. The weld strength mismatch should always be higher than unity, which is required for healthy weld properties. Weld strength mismatch presented in Eq. 5.22.

$$Y_{SR} = Y_{S\,(WM)} / Y_{S\,(BM)} \tag{5.22}$$

Where Y_{SR} is weld strength mismatch, $Ys_{\,(BM)}$ and $Y_{S\,(WM)}$ are yield strength of base metal and weld metal respectively. In the case of a dissimilar weld, for calculation purpose, Ys (BM) is taken as the maximum one among the two base metals.

From Table 5.16, it is observed that for the electrodes E2M and CE, the YSR of the welds is greater than unity but less than unity for E18M weld. The value of YSR for the welds fabricated using laboratory-developed electrodes E2M is highder comparable to the commercial weld. Yield strength was also improved with the higher Cr content because Cr provides some degree of solid solution strengthening because it's a substitutional atom in both BCC and FCC crystal lattice (Pandey et al., 1994). Weld made with laboratory electrode E2M possesses a higher amount of Cr with Low amount of Fe (See Table 5.14), which also leads to better tensile properties.

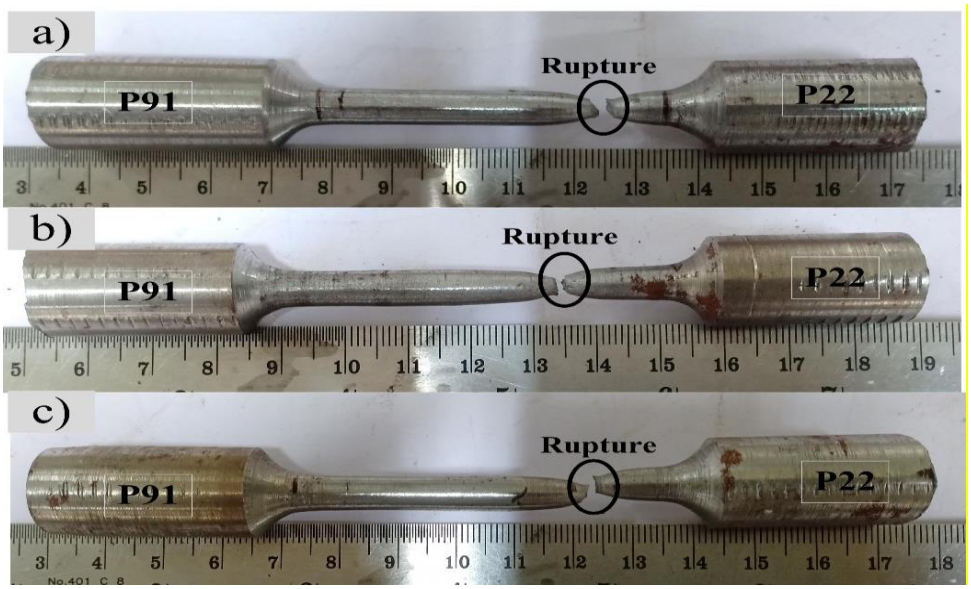

Figure 5.14: Fractured weld tensile test specimen fabricated using a) commercial electrode CE b) Electrode E2M c) Electrode E18M

Table 5.16: Tensile properties of welds

	UTS (N/mm²)	**Ys (N/mm²)**	**%E**	**Y_{SR} (P91 to weld)**	**Failure location**
P22 base metal	515	275	29.22		-
P91 Base metal	695	478	22.37		-
CE weld	610.16±15	500.12	35.05	1.09	P22 side
E2M weld	630.23±10	550.29	32.81	1.15	P22 side
E18M weld	545.18±31	450.43	33.21	0.94	P22 side

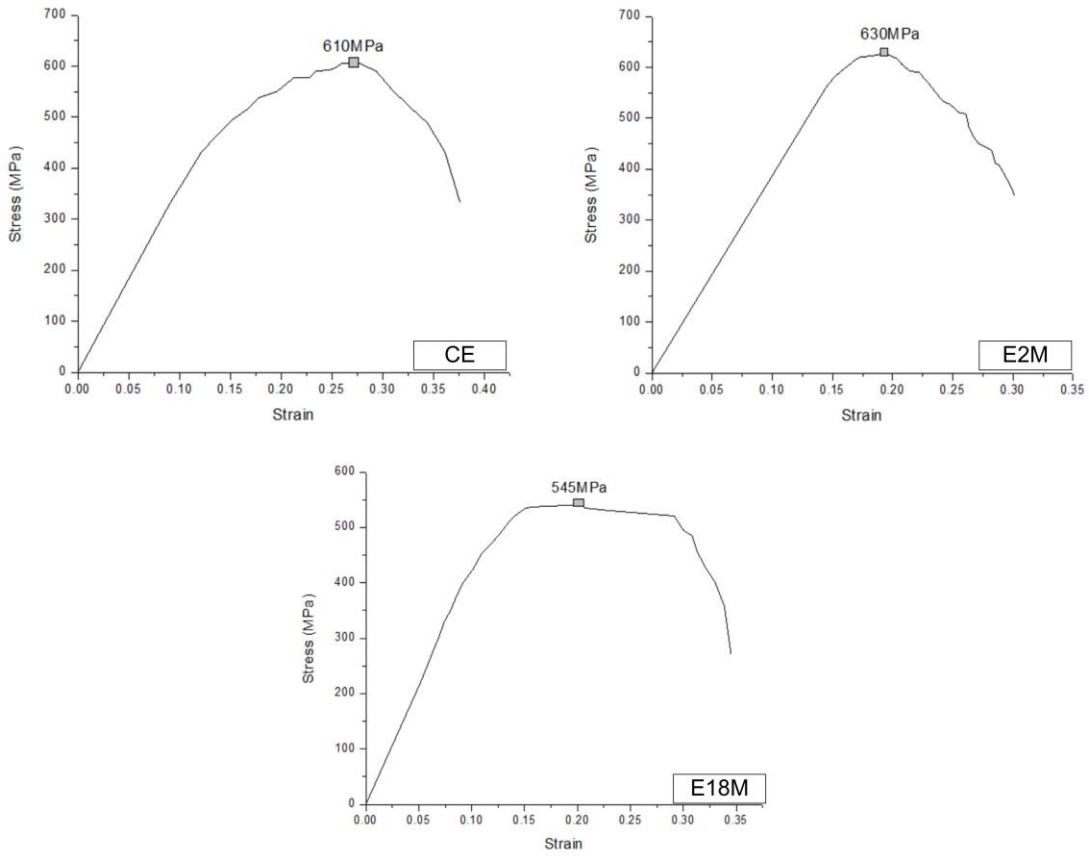

Figure 5.15: Stress vs strain of tensile test for fabricated weld specimen

The results of the Charpy impact tests performed at room temperature are given in Table 5.17. The average impact energy value obtained from three iterations has been reported here. Weld fabricated with laboratory-made electrode E2M has a higher impact fracture energy (144J). High flux basicity reduces weld metal oxygen and improves toughness. For dissimilar weldment, the minimum prescribed value for toughness is 80J (Lau et al., 1986; Jindal et al., 2014). All fabricated welds possess lower values than the base materials but have a higher value than the permissible value. It has been reported that replacing CaO with CaF_2 causes a significant reduction in the weld metal oxygen, which improves the toughness (Natalie et al., 1986). Laboratory prepared electrode coatings are highly basic coatings with a higher basicity index (B.I > 1.5), which provide welds with better mechanical properties due to the low oxygen and hydrogen levels.

Table 5.17: Impact properties of welds

Specimen	P22 base	P91 base	Weld CE	Weld E2M	Weld E18M
Impact Energy (J)	198±4	247±4.5	121±4	144±6	115±3

5.7 Hot corrosion investigations on P22/P91 dissimilar welds

Specimens were cut from the fabricated welds (CE, E2M, and E18M) and base materials (P22, P91) to perform hot corrosion experiments under the exposure of salt mixtures (SM1, SM2). The detailed procedure for specimen preparation and experimentation was discussed in section 4.4.9. Thermogravimetric analysis was performed on the prepared specimen and studied the oxidation kinetics involved. X-ray diffraction and SEM/EDS analysis were used to characterize the corroded specimens.

5.7.1 Thermogravimetric analysis and oxidation kinetics

Molten salt corrosion experiments were performed at the temperature of 650°C and 750°C for 50 hours. Weight gained during the 50 hours cyclic study was observed and used to predict the oxidation kinetics for the different specimens operated under these conditions. In agreement

with the literature (Chicardi et al., 2016; Khanna et al., 1986; Laverde et al., 2004; Mahajan et al., 2019a, 2019b; Mittal et al., 2015) low alloy Cr-Mo steels possess parabolic oxidation kinetics at high temperatures when exposed to molten salt environments. Figure 5.16 shows the plots of the observations recorded during the corrosion study for 50 cycles. General kinetics equation uses to fit these curves and calculate the parabolic rate constant is represented by Eq. 5.23:

$$\frac{\Delta W}{A} = k_p t^n + C \qquad (5.23)$$

Where `n` is the oxidation exponent (0.5 for parabolic curves), Kp is the oxidation rate constant, ΔW/A = weight gain/unit area, t is the oxidation time and C is a constant that includes the oxidation prior to reaching the isothermal condition.

Parabolic rate constants for different specimen operated at different conditions were calculated using Eq. 5.23 is expressed in Table 5.18.

Table 5.18: Parabolic rate constant (K_p) ($mg^2\ cm^{-4}\ s^{-1}$) for different specimen

	650°C SM1	750°C SM1	650°C SM2	750°C SM2
P22 Base	0.140 x 10-8	1.93 x 10-8	3.01 x 10-8	8.95 x 10-8
CE	0.1 x 10-8	1.3 x 10-8	2.1 x 10-8	6.7 x 10-8
E2M	0.0935 x 10-8	0.9 x 10-8	1.5 x 10-8	4.7 x 10-8
E18M	0.1 x 10-8	1.2 x 10-8	1.8 x 10-8	5.5 x 10-8
P91 Base	0.0954 x 10-8	0.344 x 10-8	0.273 x 10-8	1.72 x 10-8

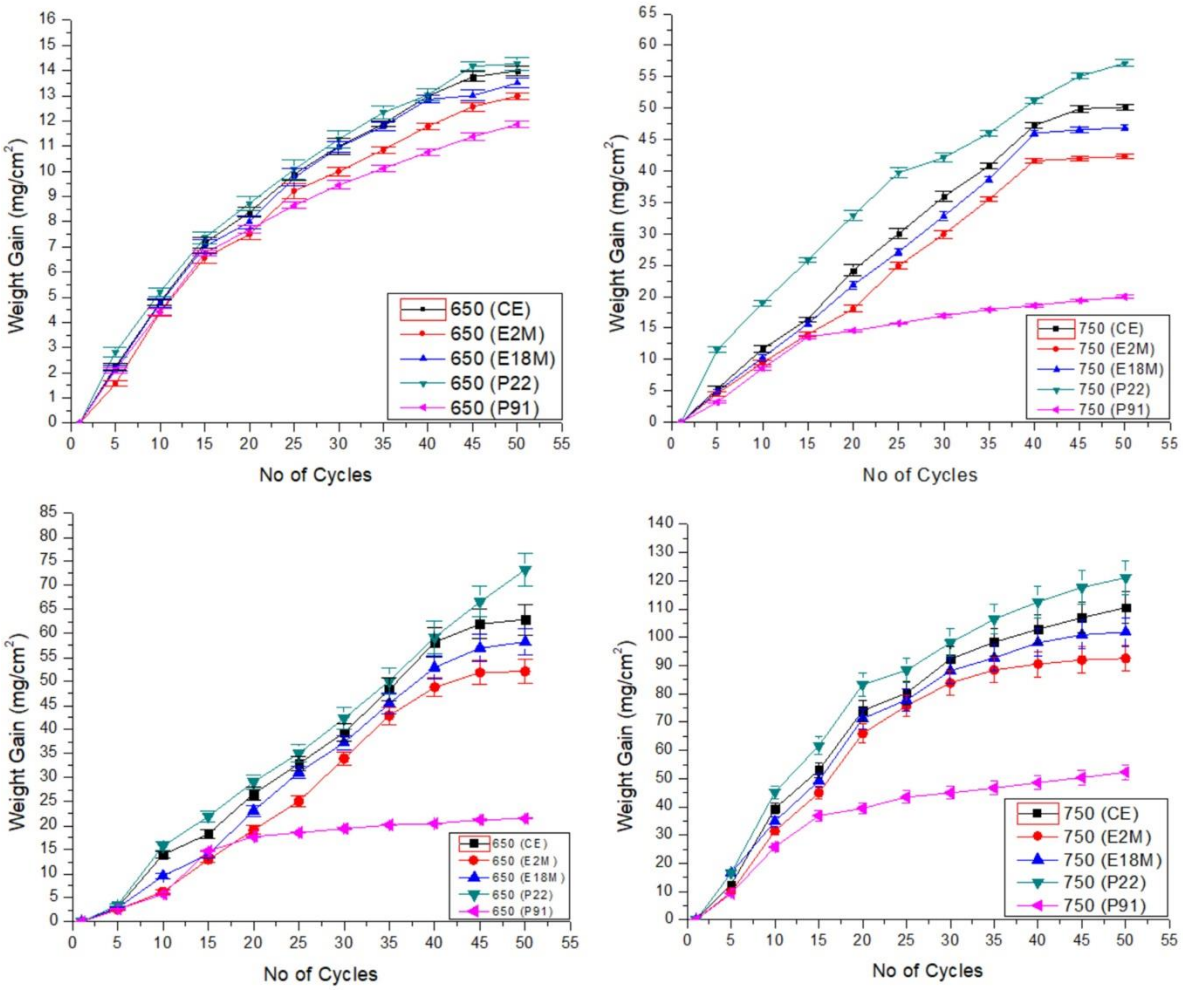

Figure 5.16: Weight gain plots for different weld specimens

Oxidation exponent `n` was used to describe the behavior of oxidation kinetics. The value of `n` (Oxidation exponent) and R^2 (coefficient of determination) was calculated by fitting the thermogravimetric plots (Figure 5.16) using curve fitting analysis (Table 5.19). To the parabolic

oxidation kinetics, the value of the oxidation exponent should be 0.5, and for the linear oxidation kinetics, it comes out to be 1. From Table 5.19, it was observed that the value of the oxidation exponent for most cases lies in the range of 0.47 - 0.7. This states that the specimen follows the parabolic oxidation kinetics, which means the growth of a protective oxide layer decreases with an increase in time.

Table 5.19: Coefficient of determination (R^2) and oxidation exponent (n)

	650°C SM1		750°C SM1		650°C SM2		750°C SM2	
Specimen	**n**	**R^2**	**n**	**R^2**	**n**	**R^2**	**n**	**R^2**
P22 Base	0.7	0.986	0.64	0.977	0.82	0.959	0.66	0.928
CE	0.77	0.969	0.7	0.992	0.75	0.959	0.68	0.919
E2M	0.7	0.983	0.71	0.992	0.8	0.99	0.63	0.905
E18M	0.77	0.964	0.72	0.993	0.73	0.987	0.69	0.953
P91 Base	0.71	0.953	0.47	0.984	0.69	0.915	0.65	0.846

From Figure 5.16, it was observed that the specimen exposed to molten salt mixtures at 750°C gain higher weight for the initial 15-20 cycles, and the corrosion rate become slower as the number of cycles increased. For temperature 650°C, an apparent linear regime after a parabolic period was observed in some cases. This is due to the complex oxidation process of the alloys at a higher temperature. P22 base experienced the highest weight gain in all the cases, while P91 weight gain was recorded as the lowest. Figure 5.16 also depicts that the welds prepared with E2M electrodes gain lesser weight than the weld made with commercial electrodes (CE). Higher weight gain was observed in the specimen exposed to SM2 as compared to SM1 for both the temperature conditions. A lower corrosion rate was observed in the case of E2M welds as compared to CE welds.

Under the molten salt attack, the protective oxides are dissolved at the oxide/salt interface and re-precipitate as non-protective particles. Alkali sulphate Na_2SO_4 is a prerequisite to the hot corrosion (Rapp, 2002). The melting temperature of Na_2SO_4 is 884°C, and after combining with V_2O_5 forms the sodium metavanadate ($NaVO_3$), which has a very low first melting temperature (~571°C). This sodium vanadate acts as an oxygen carrier to the alloy surface and accelerates the corrosion (Kumar et al., 2007). Aggressive corrosion attack was also observed when the chlorine is present into the oxidation environment, which is generally called active oxidation. Alkali chlorides react with metals to form metal chlorides (Eq. 5.24), which have high vapor pressure at metal/scale interface, leading to continuous evaporation (Eq. 5.25) (Mohanty et al., 2004; Nielsen et al., 2000).

$$M\,(s) + Cl_2\,(g) = MCl_2\,(s) \quad (5.24)$$

$$MCl_2\,(s) = MCl_2\,(g) \quad (5.25)$$

$$3MCl_2\,(g) + 3O_2\,(g) = M_2O_3\,(s) + 3Cl_2\,(g) \quad (5.26)$$

$$2MCl_2\,(g) + \frac{3}{2}O_2\,(g) = M_3O_4\,(s) + 2Cl_2\,(g) \quad (5.27)$$

M in the above equations can be Fe, Cr, Ni, or Mo. The concentration of oxygen near the oxide scale is higher, leading to the oxidation of the metal chlorides (Eq. 5.26 and Eq. 5.27). Low alloy steel with a higher amount of Fe results in the formation of loose and non-protective iron oxides (Fe_2O_3 and Fe_3O_4), which does not protect the alloy against further attack. The presence of chlorine in the molten salts can react with Cr_2O_3 and make this protective oxide layer porous. This further leads to the penetration of chlorine through cracks and voids, which reacts with alloying elements (Fe, Cr, Ni, or Mo) and accelerates the corrosion.

Highly basic electrodes are known to reduce the diffusible hydrogen content of the molten weld pool. This invariably leads to the fabrication of sound and defect-free welds with enhanced structural integrity. Cr and Ni in welds are known to increase the corrosion resistance characteristics. Investigations on fabricated weld reveal that welds made with laboratory-

developed electrodes contain higher Cr and Ni content as compared to the commercial electrodes.

5.7.2 X-Ray Diffraction analysis of welds

Figure 5.17 presents the XRD plots of corroded specimens. A significant oxide scaling was observed in the corroded weld specimens. The various oxides were observed in the corroded specimens. The Fe_2O_3 was observed as the main oxide phase at 2θ = 35.82° [01-056-1303] along with Fe_3O_4 at 2θ = 33.46° [01-076-8881] in the oxidized specimen. Oxide phases like $FeCr_2O_4$, $NiFe_2O_4$, $CrNiO_4$ are also observed along with FeS_2 and Mn_2O_3 which are in accordance with the findings of Kumar et al. (2007). The inner anion migration of oxygen (O^{2-}) and sulfur (S^{1-}) in the case of corroded specimen further causes grain boundary oxidation and sulfidation. These grain boundaries act as fast diffusion paths for cation and anion migration to increase the corrosion rate. However, the impact of elemental sulfur is much more than oxygen as sulfides are much corrosive than oxides. The sulfides provide a path for rapid outward diffusion of the cation (mainly Fe), resulting in a rapid corrosion attack (Ghosh et al., 2016). Higher outward diffusion of iron (Fe) was observed due to the presence of Fe_2O_3 as a significant phase in the inner oxide scale. In the welded specimen, Cr rich spinals were found in combination with iron and nickel, which slow down the corrosion rate by forming a protective layer against attacking species of molten salts.

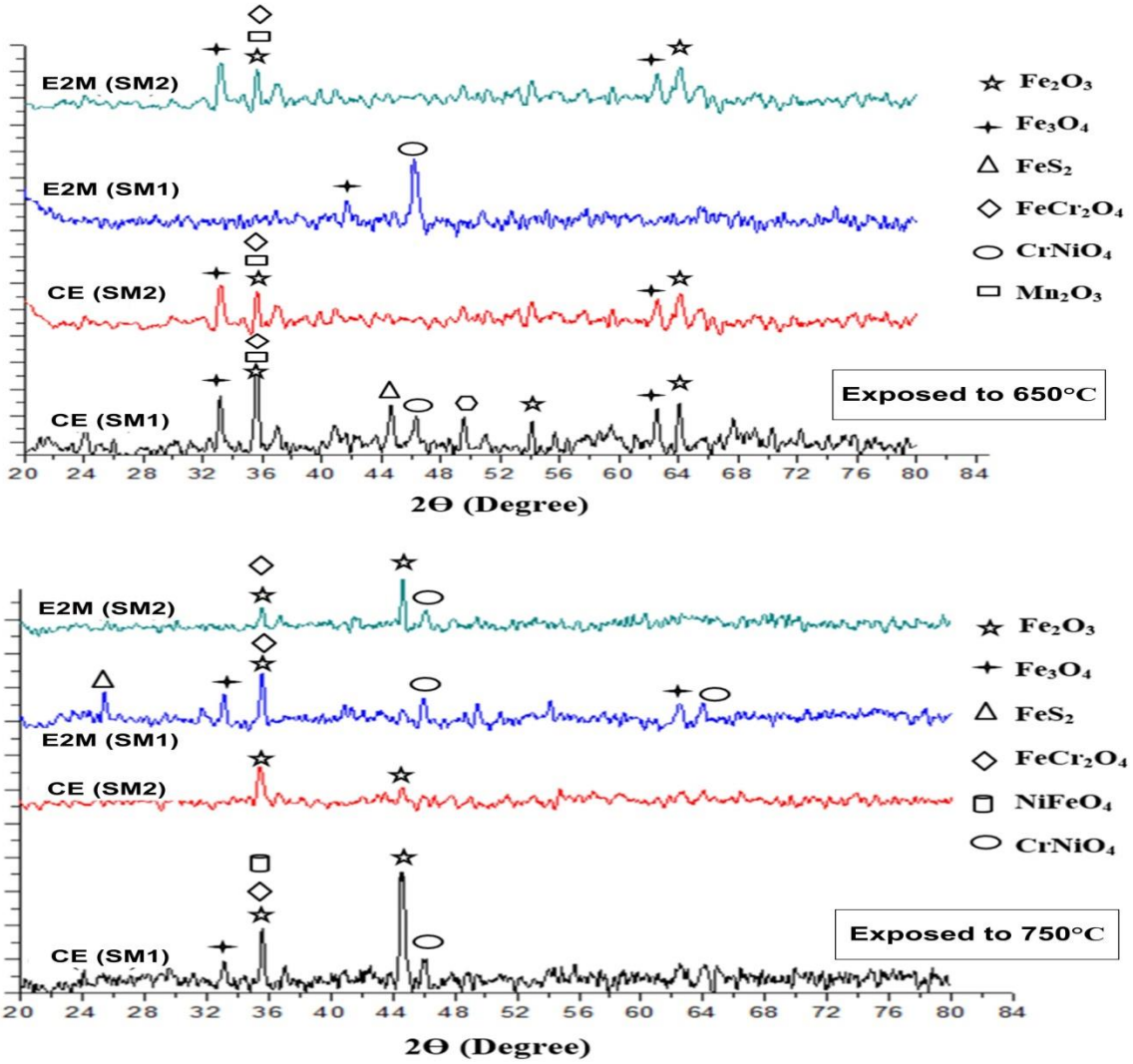

Figure 5.17: XRD plots of post corrosion weld specimens

5.7.3 SEM/EDS Analysis

SEM images were used to estimate the oxide scale thickness formed on the weld specimens mounted along the cross-section. Line scan graphs were also taken to observe the intensity of different elements along the weld cross-section.

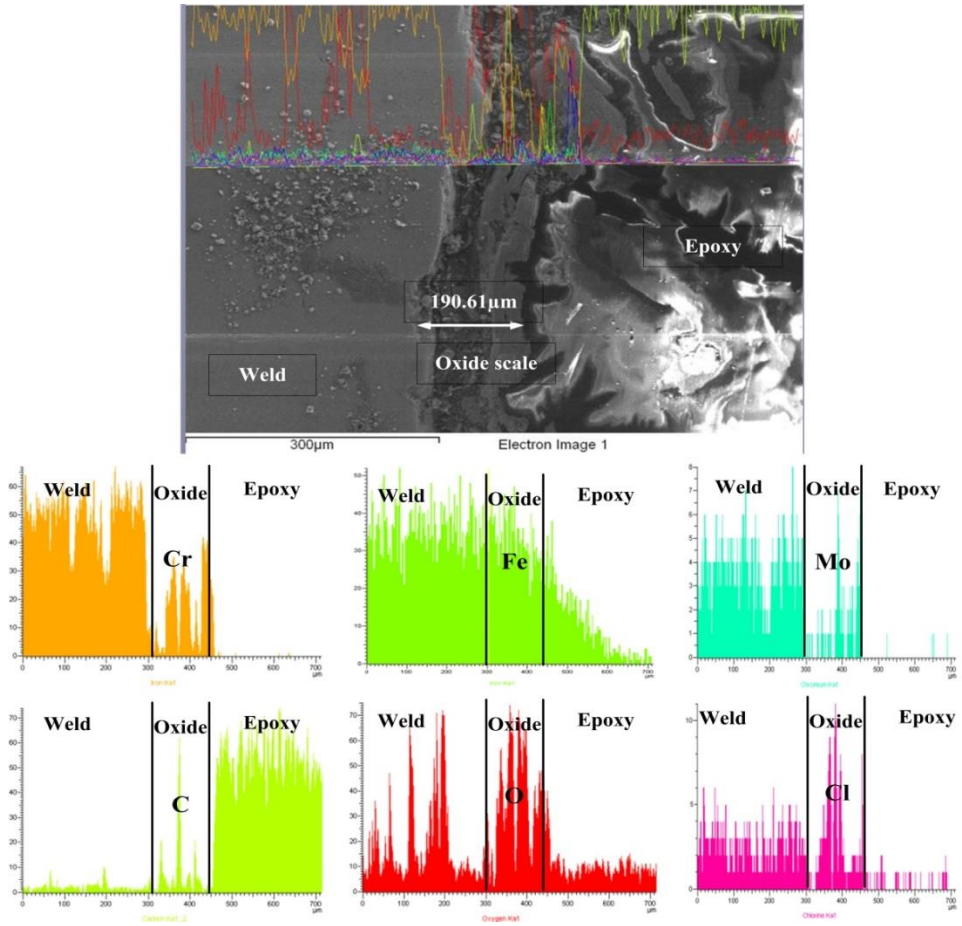

Figure 5.18: SEM images with EDS line scan mapping of P22 steel under the exposure of Na_2SO_4 + NaCl salt mixture at 750°C

From the thermo-gravimetric analysis, maximum weight gain was observed in the P22 base metal under the molten salt mixtures at different temperatures. Oxide scale thickness of 190.6µm was observed in the P22 base metal specimen when exposed to SM2 (Figure 5.18). Line scan graphs also support the results obtained from the SEM images. Outer oxide scale majorly consists of Fe-oxides as the intensity of the oxygen and iron was higher with a significantly low amount of Cr.

5.7.3.1 Welds exposed to $Na_2SO_4 + V_2O_5$ (SM1)

SEM images of commercial weld specimens (CE) and weld (E2M) exposed to salt mixture 1 (SM1) at temperature 750°C were shown in Figure 5.19 and Figure 5.20, respectively. Oxide scale thickness observed in weld (E2M) was lower (65.61µm) as compared to the oxide layer thickness of the commercial weld (130.50µm). SEM images of weld specimens exposed to SM1 revealed the Cr layer in the lower part of the scale attached to the substrate. A small concentration of Sulphur was also distributed at the lower scale of E2M and CE welds. The base metal experienced intense spalling and significantly higher weight gain as compared to the welded specimens. CE weld specimens also experienced a high corrosion rate during the initial hours of study when exposed to the salt mixture. These higher corrosion rates might be attributed to the rapid pickup of oxygen through the molten salt layer. From the XRD analysis (Figure 5.17) of the corroded specimens, Fe_2O_3 was found to be the significant phase present in the oxide scale. The presence of Fe_2O_3 in the upper scale has been reported to be non-protective oxides that accelerate the hot corrosion.

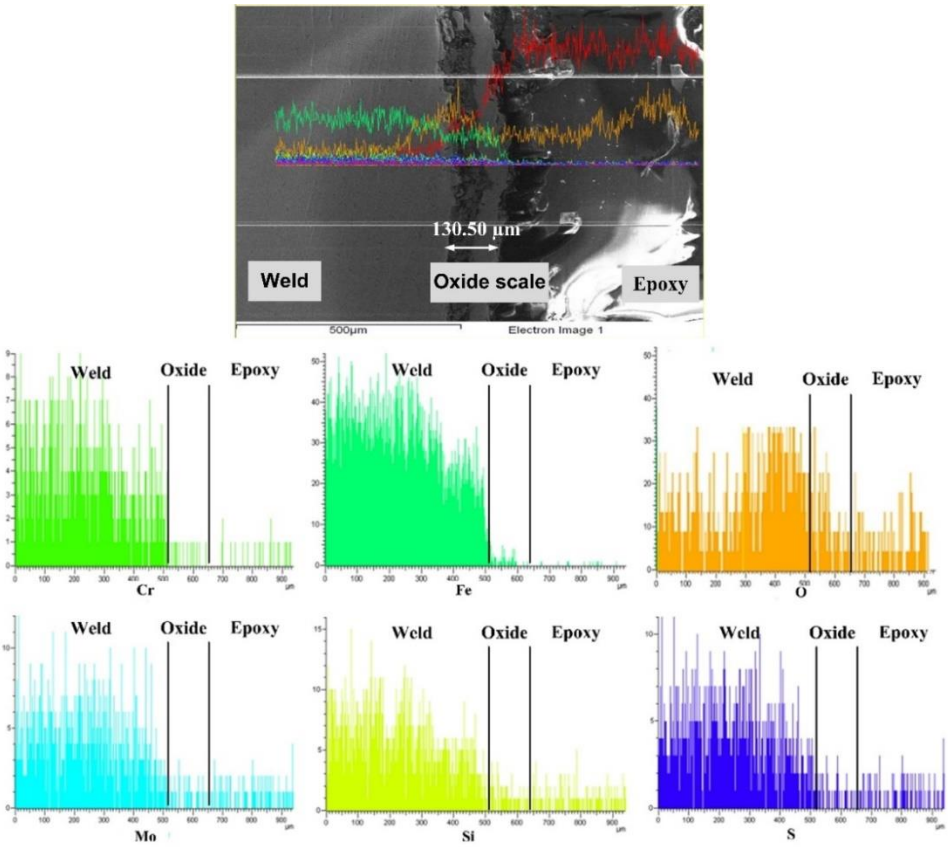

Figure 5.19: SEM images with EDS line scan mapping of commercial weld (CE) under the exposure of Na_2SO_4 + V_2O_5 salt mixture at 750°C

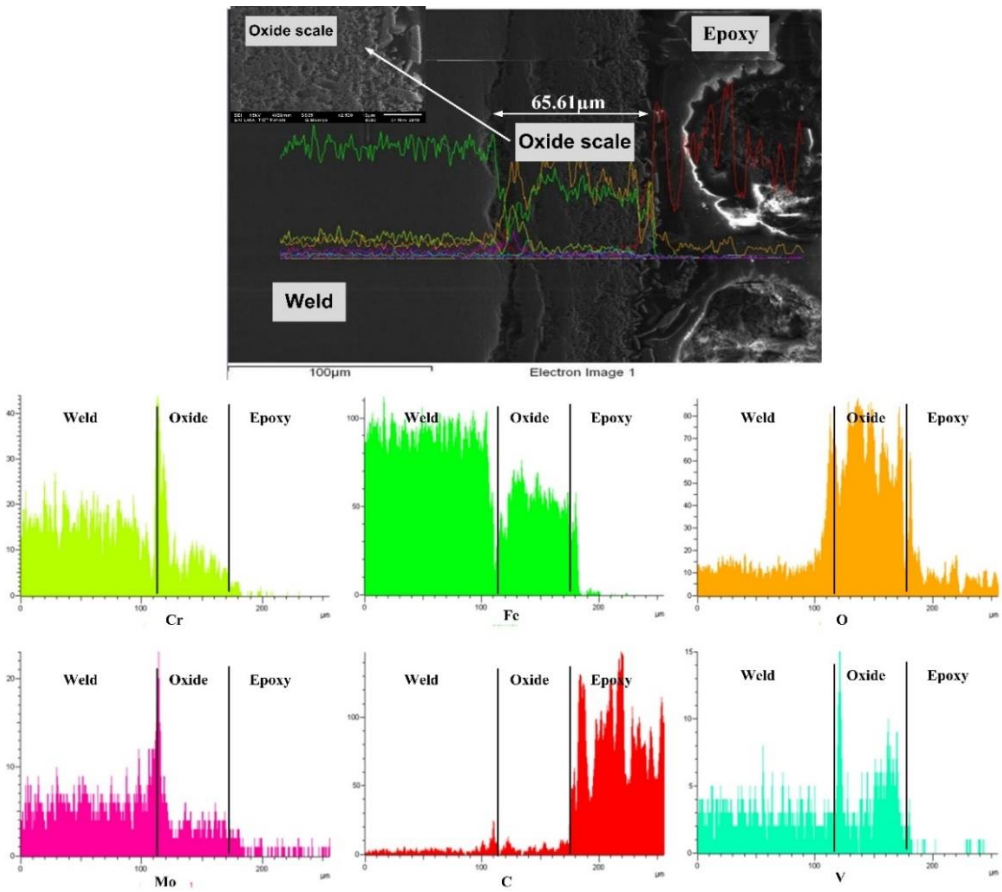

Figure 5.20: SEM images with EDS line scan mapping of weld (E2M) under the exposure of Na_2SO_4 + V_2O_5 salt mixture at 750°C

Further, it was observed that the oxide scale in weld specimens mainly consists of iron with a small amount of Cr. The higher weight gain of base metal and commercial electrode specimens with the formation of thicker scale have been attributed to the absence of protective inner scale of Fe-Cr oxides, which may be due to the non-availability of Cr in this region. The debonding was observed at the metal/scale interface, which might be due to the formation and evaporation of acidic oxides of Mo, Cr, W, and V present in the specimen (Mohanty et al., 2004; Nielsen et al., 2000). These acidic oxides exhibit high vapor pressure, thereby leading to their evaporation from the salt/gas interface results in the debonding of the oxides from the substrate.

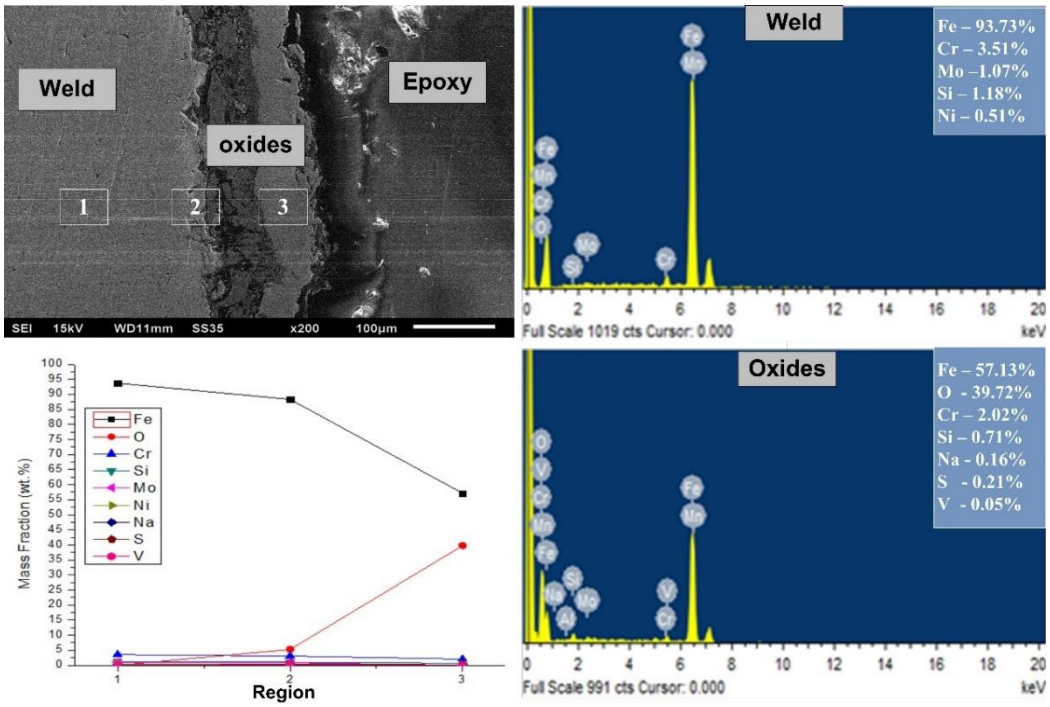

Figure 5.21: SEM image with EDS point analysis of commercial weld (CE) under the exposure of Na_2SO_4 + V_2O_5 salt mixture at 750°C

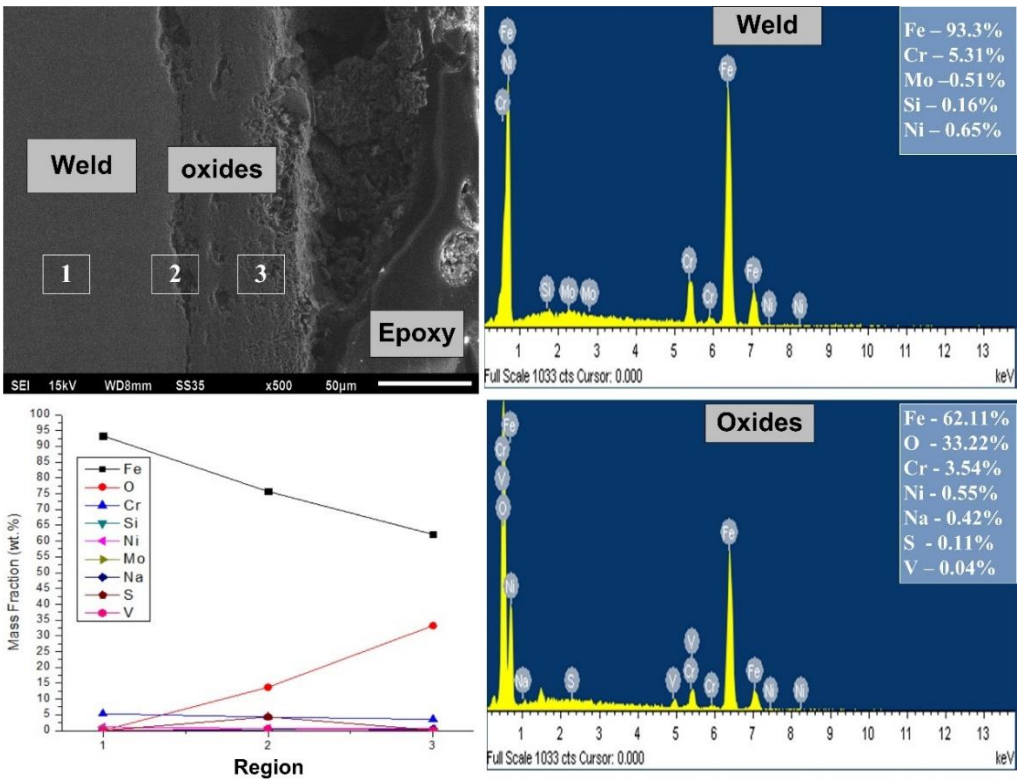

Figure 5.22: SEM image with EDS point analysis of weld (E2M) under the exposure of Na_2SO_4 + V_2O_5 salt mixture at 750°C

SEM images with EDS point analysis of welded specimens exposed to SM1 are shown in Figure 5.21, and Figure 5.22. Surface oxides were composed of Fe_2O_3 and Fe_3O_4. A higher concentration of oxygen was observed in the oxide scale of the CE weld specimen (39.72%) as compared to E2M. From the EDS point analysis, a higher concentration of Cr was observed at the metal/scale interface (point 2) in the case of weld E2M. The formation of a Cr-rich oxide scale at a metal/scale interface provides protection from the harmful species like S to diffuse results in better corrosion resistance of the alloy. From the XRD analysis (Figure 5.17), $(Fe, Cr)_2O_3$, $NiCrO_4$, Cr_2O_3, Cr_2NiO_4 along with iron oxides were identified in the case of weld specimen E2M. There was a significant increase in the oxide scaling observed in the specimens operated at 750°C as compared to 650°C.

5.7.3.2 Welds exposed to Na_2SO_4 + 50% NaCl (SM2)

SEM images of commercial weld specimen (CE) and weld (E2M) exposed to salt mixture 2 (SM2) at temperature 750°C was shown in Figure 5.23 and Figure 5.24, respectively. The oxide scale thickness produced in weld (E2M) was (85.26µm), and the oxide layer thickness in the case of CE weld was 155.31µm. A higher oxide scale thickness was observed in the commercial weld specimen. The oxide layers were observed at the outer part of the specimen adjacent to mounting, which majorly consists of iron oxides. Line scan maps were used to estimate the concentration of different elements across the weld cross-section. The melting of Na_2SO_4-50% NaCl mixture at 650°C makes the weld susceptible to accelerated oxidation due to acidic and basic-fluxing mechanism. Many researchers have pointed out that the formation of sodium chromate (Na_2CrO_4) could result from oxy-chloridation even the temperature is lower than the melting point of salt deposits As Na_2CrO_4 is formed, the salt will wet the specimen surface which eventually leads to a mechanism of hot corrosion dominated by molten salt. SEM images of commercial weld specimens revealed the presence of Cl concentration near the metal/scale interface. The corrosion rate in the case of the commercial weld specimen was higher as compared to the specimen of E2M weld when exposed to SM2.

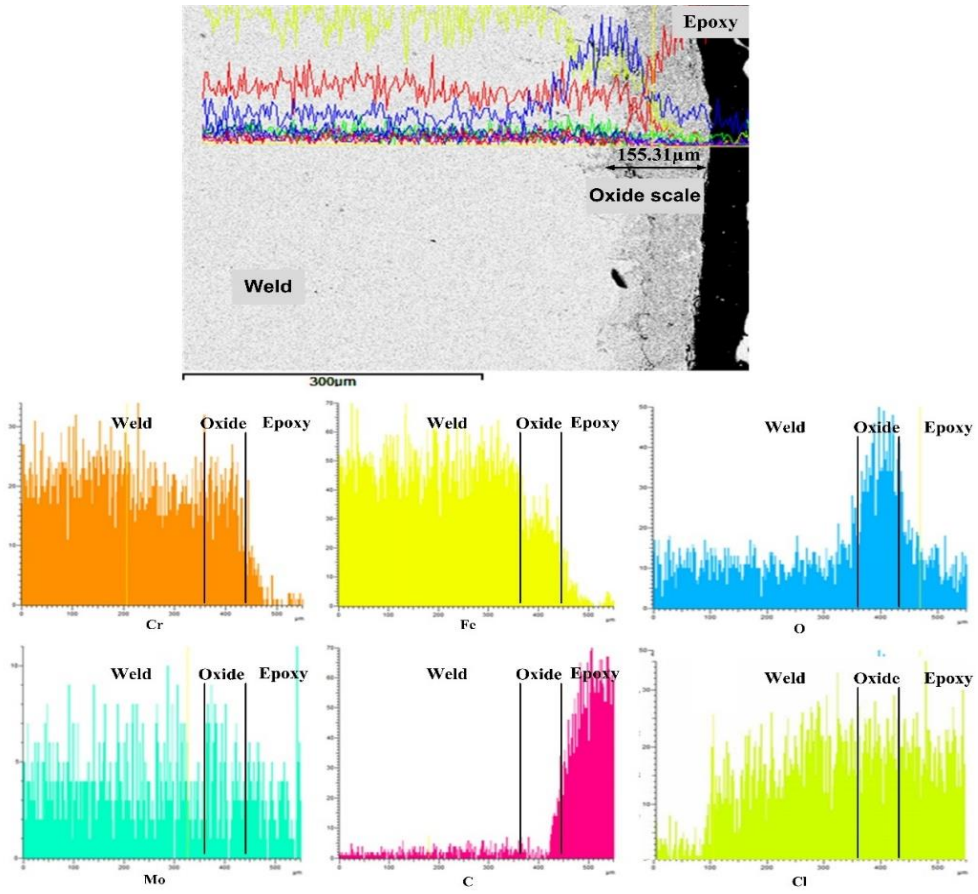

Figure 5.23: SEM images with EDS line scan mapping of commercial weld (CE) under the exposure of Na_2SO_4 + NaCl salt mixture at 750°C

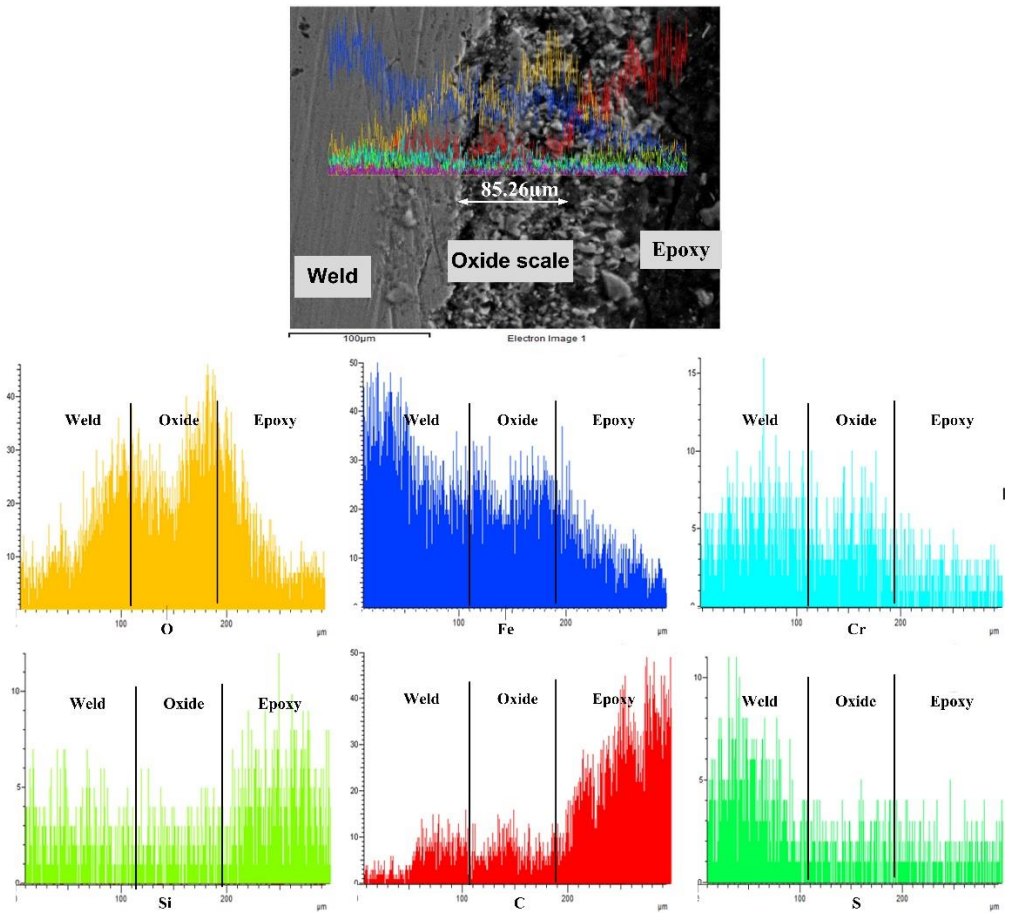

Figure 5.24: SEM images with EDS line scan mapping of weld (E2M) under the exposure of Na_2SO_4 + NaCl salt mixture at 750°C

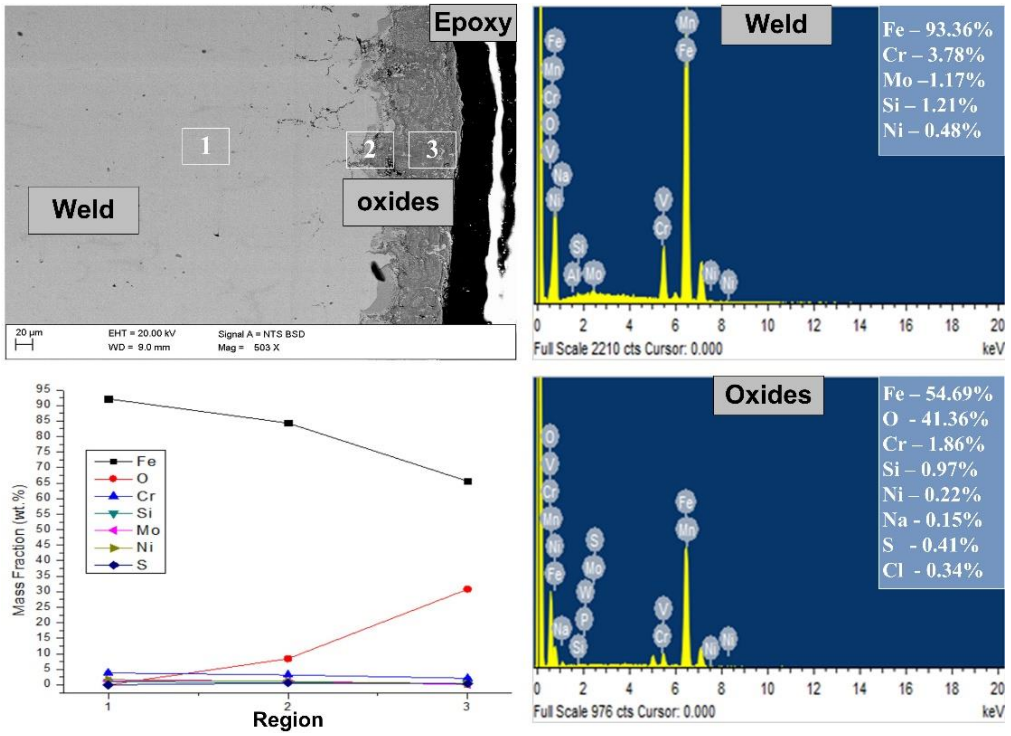

Figure 5.25: SEM image with EDS point analysis of commercial weld (CE) under the exposure of Na_2SO_4 + NaCl salt mixture at 750°C

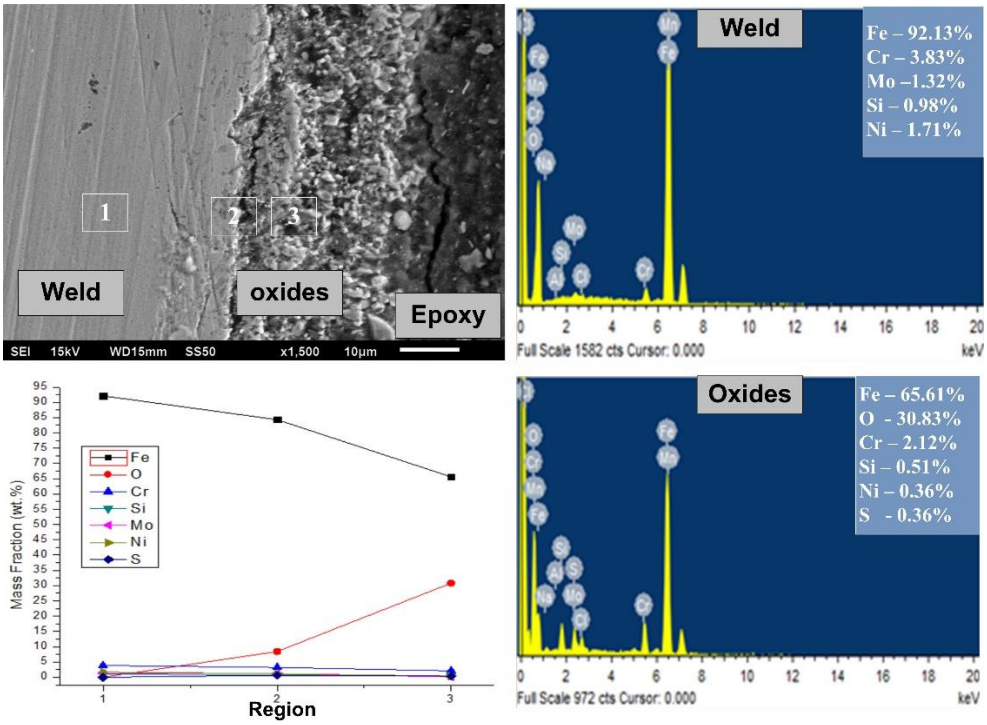

Figure 5.26: SEM image with EDS point analysis of weld (E2M) under the exposure of Na_2SO_4 + NaCl salt mixture at 750°C

SEM images with EDS point analysis of welded specimens exposed to SM2 are shown in Figure 5.25, and Figure 5.26. A higher concentration of oxygen was observed in the oxide scale of CE weld specimen (41.36 wt. %) as compared to E2M (30.83 wt. %). From the XRD analysis (Figure 5.17), Fe_2O_3, Fe_3O_4 were the major phases present in the oxide scaling due to the intense spalling in the chloride-containing environment. Fe-Cr rich spinals were also observed near the metal/scale interface in the case of the E2M welds. From SEM images Figure 5.25-5.26, significant cracks were clearly seen on the weld surface adjacent to an oxide scale. This was due to the active oxidation phenomena which happen in the presence of chlorine in the oxidation environment. Literature reveals that when chlorine is present in the oxidizing environment, the oxide scale formed is porous, loose, and cracked (Grabke et al., 1995; Mohanty et al., 2004; Nielsen et al., 2000; Skrifvars et al., 2008, 2010). Porous scale increases the chances of the oxygen and other gases to penetrate through the oxide scale to further react with the substrate and accelerate corrosion. The oxide scale formed in the weld specimen exposed to SM2 was thick, porous, and non-adherent. The metal surface adjacent to the oxide scaling shows significant cracks and pores. This leads to accelerated corrosion in the environment of SM2 as compared to SM1. The addition of vanadium and chlorine to the alkali sulphate at higher temperature forms low melting temperature eutectoids.

5.8 Fabrication and characterization of P91/SS304L dissimilar welds

5.8.1 Fabrication, preliminary inspections and weld chemistry

P91 and SS304L are structural steels having a low percentage of carbon (<0.09 wt. %), with Cr as a significant constituent. P91 possesses Mo, which provides high-temperature strength and corrosion resistance. These steels are used for high-temperature applications due to their creep resistance and corrosion-resistant properties. Atomic absorption spectroscopy results of the fabricated welds are presented in Table 5.20. It can be seen that the welds made with the laboratory-made coatings contain a low amount of carbon (<0.041) as compared to the weld made with a commercial electrode (= 0.051). High carbon concentration in the weld zone makes it brittle by enhancing its hardness. This further leads to increased susceptibility of HAZ cracking. A higher amount of Ni and Cr content was observed in the welds made with laboratory-made electrodes (E7M, E16M) as compared to the welds made with a commercial

electrode (CE). The presence of the higher Cr and Ni content provides better mechanical and corrosion-resistant properties.

Table 5.20: Chemical composition of welds fabricated using Ni-based electrodes (wt%)

Welds	C	Si	Mn	Cr	Mo	Ni	Fe	Ti	Nb
CE	0.051	1.02	7.1	11.6	1.02	48.9	25.91	2.86	1.53
E7M	0.036	0.48	3.4	19.3	0.49	63.8	9.57	1.85	1.39
E16M	0.041	0.56	4.2	17.4	0.84	57.4	15.18	1.51	1.47

The dilution also play significant role along with the electrode coating compositions and weld metal recovery during welding operation. As the dilution calculations were performed by assuming the 15% base dilution (SS304L) and 85% filler (IN-82) for the dissimilar weld using SMAW process (15% dilution is assumed along with 70% due to the buttering layer of IN-82 on the P91 side). By considering the dilution effect, the Cr content was estimated 3.412 wt. %. Cr content in E2M was observed as 4.01 wt. % which is higher because the addition of chromium powder in the coating and better weld recovery of Cr in laboratory developed electrode fabricated welds. The concentration of Mo and Mn was estimated and are comparable to the concentration estimated using atomic absorption spectrometry analysis. Mo was recovered well 0.88 and 0.87 wt. % in E2M and E18M welds. Similarly, the Mn was recovered 0.46 and 0.44 wt. % in both the E2M and E18M respectively. It was observed from the above calculations that weld element recovery and electrode coating compositions also plays significant role along with the dilution in deciding the final weld compositions.

5.8.2 Metallurgical examination of P91/SS304L welds

Dissimilar welds consist of different metallurgical zones that are immediately adjacent to each other with a significant change in properties. This leads to localize the strain. The optical microstructures and scanning electron microscopic (SEM) images of base metals are shown in Figure 5.27. The various zones of P91/SS304L DMW were fabricated using laboratory-made electrodes E7M shown in Figure 5.28, while for commercial electrodes (CE) shown in Figure 5.29. A clear transition between weld fusion zone (WFZ), buttering layer and base metals are visible. Figure 5.27a and 5.27b shows the microstructure of SS304L base metal, which consists majorly of austenitic grains. Figure 5.27c and 5.27d show the microstructure of P91 base metal which consists of tempered lath martensite with prior austenitic grain boundaries, and some of the secondary phase particles are finely distributed in the grain boundaries and within the grains. Figure 5.28a show the weld interface between SS304L and filler 182/82 welds with a HAZ of SS304L base metal. Grain boundaries near the fusion zone shows the presence of coarse austenite grains. Figure 5.28b and 5.28c show the weld microstructure at different magnifications. Grain boundaries of two types, solidification and migration, are clearly visible in the microstructure. Solidification grain boundaries (SGB`s) are primarily formed due to the competitive growth of grains across the trailing edge of weld pool. Solute diffusion into the matrix is restricted by the rapid cooling which also extends the solidification temperature range (Karthick et al., 2018). The welds made with IN-82 generally contains a higher amount of Ni > 50%, and the solidification of these welds are fully austenitic with two-phase structure consists of dendrites and inter-dendrites zone. The weld microstructure reveals as cast Ni alloy with alloy carbides (generally NbC and TiC) and columnar dendritic structure. These welds generally contain niobium (Nb). Niobium is high temperature austenite stabilizer. Available literature (Hajiannia et al., 2013) reports cellular to the columnar transformation of dendrites (Figure 5.27b) due to the constitutional cooling. Researchers also identified these dendrites enriched with Nb and form Nb carbides (Hajiannia et al., 2013).

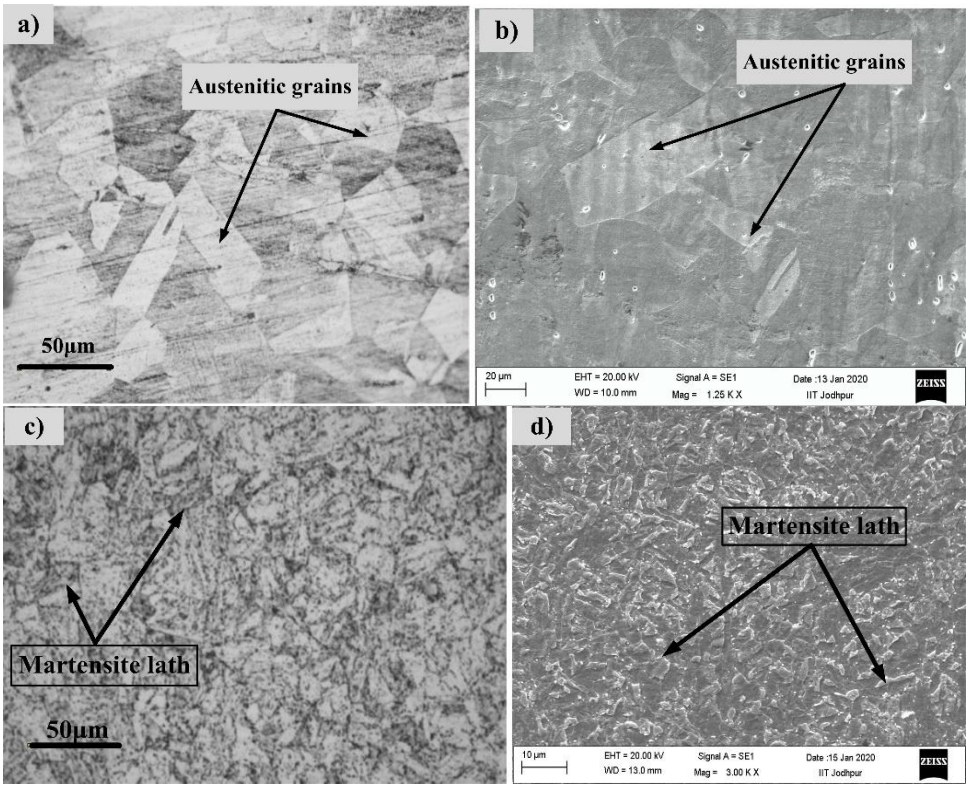

Figure 5.27: Micrographs of base materials a) Optical micrograph of SS304L b) SEM image of SS304L c) Optical micrograph of P91 d) SEM image of P91

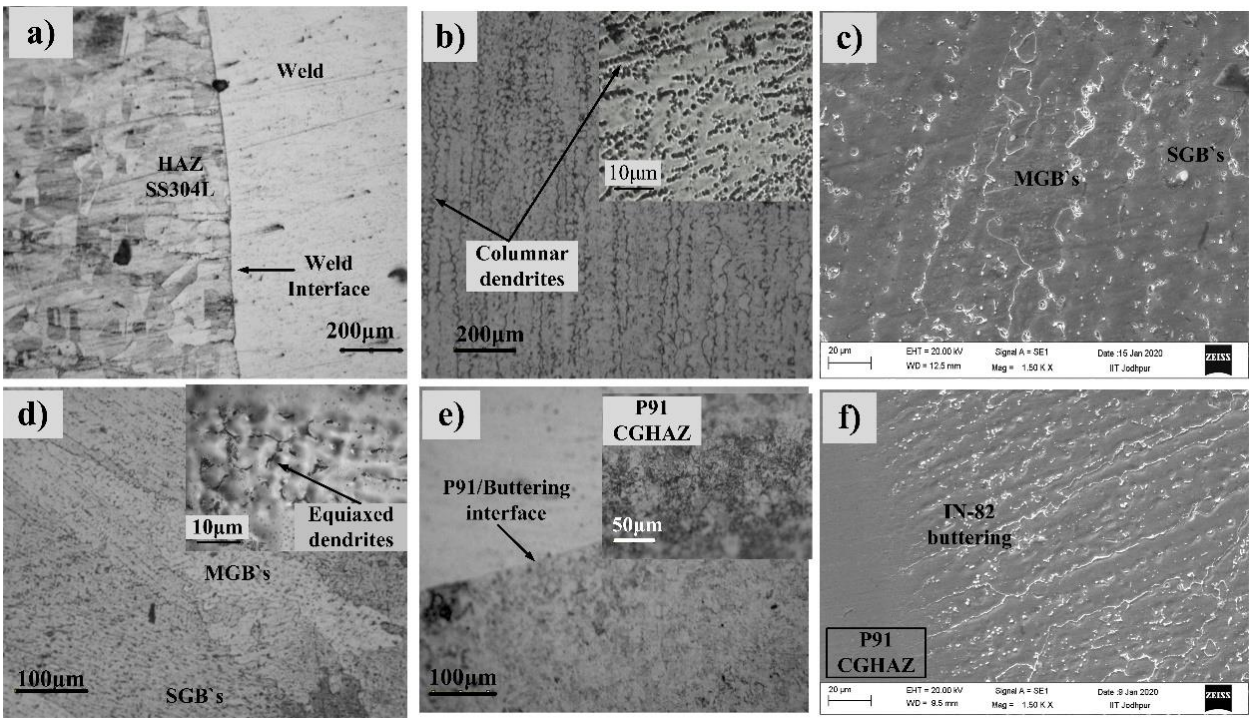

Figure 5.28: Micrographs of different regions of dissimilar weld using electrodes E7 a) Interface SS304L/IN-182 b) IN-182/82 weld at different magnifications c) SEM image of weld metal d) Buttering layer at different magnifications e) Interface P91/buttering interface f) SEM image of P91/buttering interface

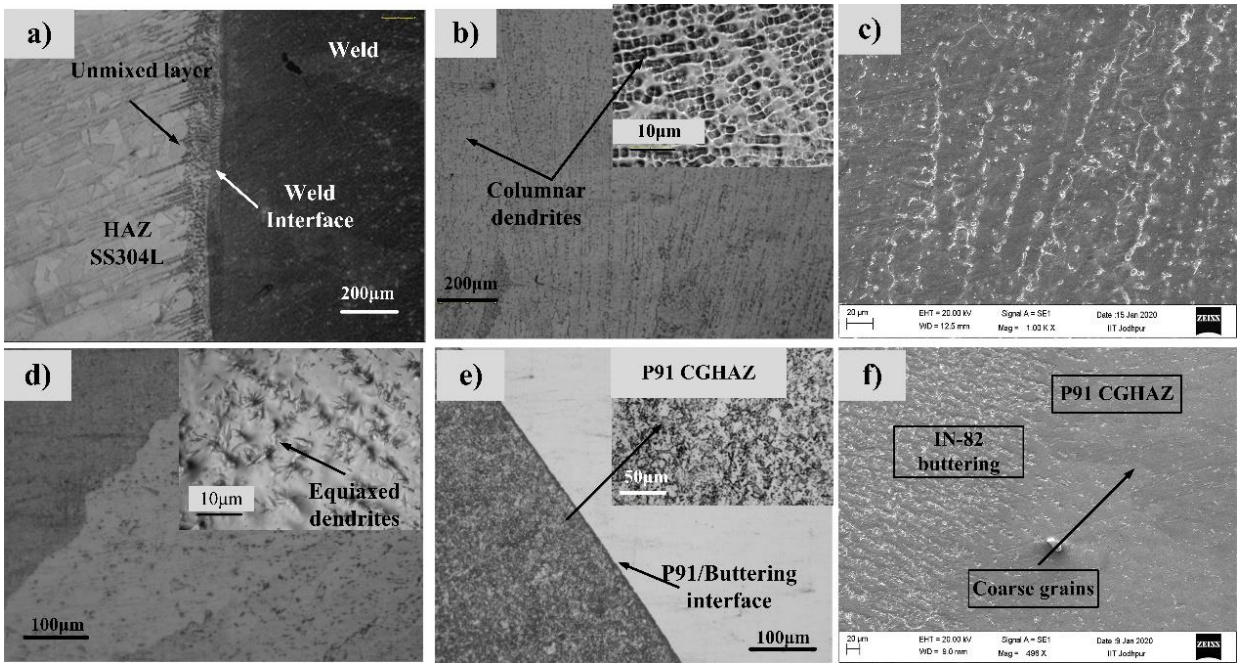

Figure 5.29: Micrographs of different regions in dissimilar weld using commercial electrodes a) Interface SS304L/IN-182 b) IN-182/82 weld at different magnifications c) SEM image of weld metal d) Buttering layer at different magnifications e) Interface P91/buttering interface f) SEM image of P91/buttering interface

Figure 5.28d presents the microstructure of the butter layer of filler 182/82, which consist of more than 68% Nickel as an alloying element. A predominant austenitic structure with some secondary phase particles (generally NbC) was observed for Filler 182/82 (Karthick et al., 2018). The microstructure of Filler 182/82 doesn't get affected by post-weld heat treatment (PWHT). Equiaxed dendrites were observed in the buttering layer at higher magnifications. A fusion boundary with tempered lath martensite was observed at the P91/Filler 182 buttering interface (Figure 5.28e). Filler 182/82 weld solidifies in pure austenitic mode while P91 solidifies as ferrite and then underwent transformation first to austenite and then to martensite. Grain growth in the HAZ of P91 was observed very near to the fusion boundary (Figure 5.28e-f). The CGHAZ was observed when moving towards the base metal from the fusion boundary. Micrographs of different metallurgical regions of P91/SS304L welds made with the commercial electrodes are shown in Figure 5.29a-f. No significant changes in the microstructure of this weld were observed as compared to the laboratory made electrode except the grain growth at the P91 HAZ near the buttering layer. There were some welding discontinuities present in the commercial electrode welds which impact the mechanical and corrosion resistance of the weld.

5.8.3 Comparison of weld`s mechanical behavior

Hardness measurement was done across the weld, with fusion zone as the origin and traversing on either side till base metals. Indents were marked at a successive distance of 1mm. Base metal SS304L has a fine austenite grain structure (Figure 5.27a-b) with a hardness value in the range of 200Hv. Heat affected zone on the side of SS304L also shows an increased hardness. Nickel is known to be a good austenite former and stabilizer. Hence, Ni-based fillers are known to favor the precipitation of austenite grains in the weld fusion zone upon subsequent cooling below the solvus temperature. The hardness of the fusion zone shows a marginal variation as compared to base metal SS304L. Moving on the other side, a buttering layer deposited with Ni-based filler is encountered. This layer has enhanced hardness as compared to the fusion zone. HAZ on the base metal P91 side is characterized with martensite which is hard and brittle. This zone has the highest hardness value amongst all other zones. P91 base metal has a typical martensitic microstructure which gives it an appreciable hardness value. Microhardness profile of P91/SS304L DMW fabricated using laboratory-made electrodes E7M, E16M and commercial electrode are presented in Figure 5.30. The average hardness of various regions of the different

welds is presented in Table 5.21. The maximum hardness of 303.05Hv was observed in P91-HAZ in the case of commercial electrode weld, while the lower values were observed in the P91-HAZ of laboratory-developed electrode welds. Post weld heat treatment was performed to relieve the excessive stresses which may develop during the buttering of P91 base alloy. From the microhardness profiles of all three welds, higher hardness values were recorded in the case of welds made with commercial electrodes and lower values were recorded in the case of welds made with electrodes coating E7M. It has been reported that an increase in CaO content in the electrode coatings have a tendency to increase it's a hardness while an increase in SiO_2 content reduces the hardness (Bhandari et al., 2016a). This can correlate with the weld developed using E7M coatings have lower a value of hardness as compared to the other welds. The heterogeneity in DMW and also in similar welded joints of P91 and P92 steel is a major problem for their application in high temperature service condition (Karthick et al., 2018). To overcome the heterogeneity and impart the ductility to WFZ and HAZ, PWHT is recommended by many of the researchers (Fuchs et al., 2010; Slaughter et al., 1962; Mittal et al., 2015; Hajiannian et al., 2013; Rowe et al., 1999; Srinivasan et al., 2016; Kulkarni et al., 2019).

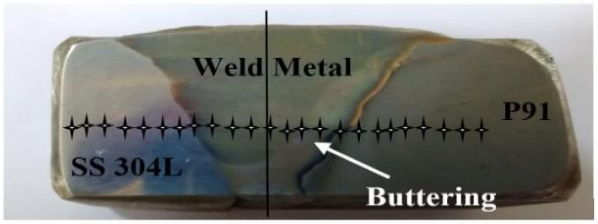

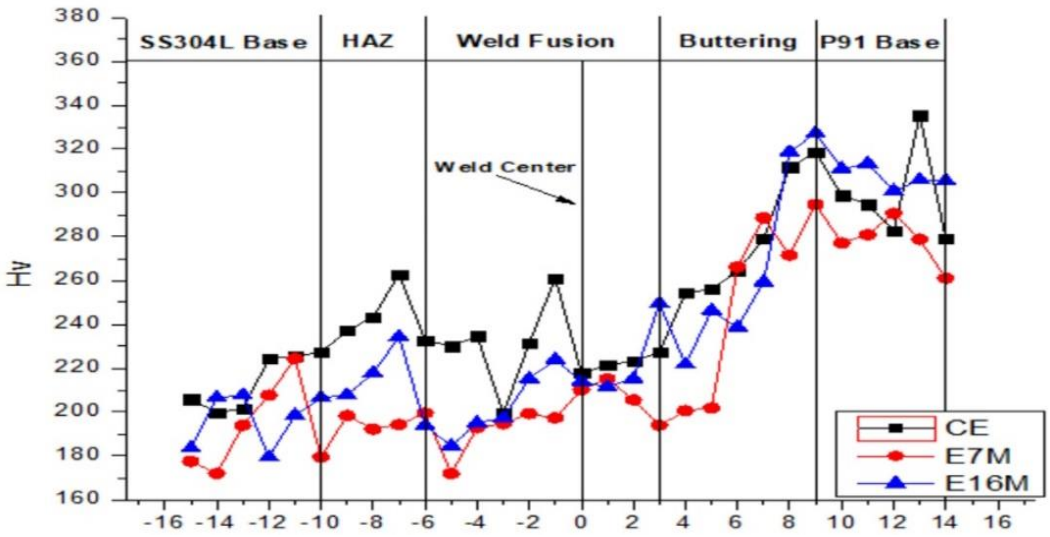

Figure 5.30: Microhardness profile of fabricated welds

Table 5.21: Average microhardness across different regions of the fabricated welds

	Base SS304L	HAZ SS304L	Weld	Butter Layer	HAZ P91	Base P91
C.E	212±11	243±11	234±12	258±4	303±17	297±6
E7M	192±18	196±3	197±10	222±7	284±10	287±5
E16M	200±9	213±9	212±12	235±10	300±14	300±8

Tensile test fractured specimen of fabricated welds and respected stress vs strain plots are shown in Figure 5.31 and Figure 5.32. The value of ultimate tensile strength, yield strength, and percentage elongation of transverse weld specimen and longitudinal weld specimen is presented in Table 5.22. Maximum tensile strength {= 685.3 N/mm² (transverse weld) and = 659.03 N/mm² (longitudinal weld)} was observed in the case of weld made with E7M electrode coating. The tensile strength obtained in case of electrode coating E7M is higher than the SS304L base and closer to the base metal P91, which is in agreement with the statement suggested by Rathod et al. (2015): In this statement, the author quoted that the strength of dissimilar welded joint should not be inferior to the parent metals. Mechanical properties of the welds depend

upon the microstructure of the weld and chemical composition also. Materials used in high-temperature applications require enhanced ductility and tensile properties. A higher amount of Ni in the welds promotes fully austenitic vermicular shaped microstructure which results in better ductility and mechanical properties with high-temperature corrosion resistance. Previous studies reported that the fracture generally happened on the low alloy steel side, which is generally due to the presence of weaker and stronger zone because of carbon migration along the transition joint (Rowe et al., 1999; Srinivasan et al., 2016; Kulkarni et al., 2019; Moteshakker et al., 2015; Rathod et al., 2015). Rathod et al. (2015) suggested that if the content of Mn, Cr, and Ni is reduced with an increase in Fe in the weld, it also affects the weld metal tensile properties. Yield strength is also improved with the higher Cr content because Cr provides some degree of solid solution strengthening because it's a substitutional atom in both BCC and FCC crystal lattice (Moteshakker et al., 2015). Weld made with laboratory electrodes possesses a higher amount of Ni and Cr with Low amount of Fe (See Table 5.20), which leads to better tensile properties. The tensile strength of E7M fabricated weld is lower than the base metals P91 and and higher than base metal SS304L. This is due to the soft zone was formed at the outer edge of the HAZ and this soft zone (Figure 5.28e and 5.29e) consisted of coarsened martensitic substructure with reduced dislocation density due to intercritical heating (between AC_1 and AC_3) during the weld thermal cycle (Hanninen et al., 2006). In this investigation, the transverse tensile specimens of E7M and E16M were failed at the outer edge of HAZ to base metal interface which may consist of inter-critical HAZ.

Table 5.22: Tensile properties of welds

	UTS (N/mm^2)	**UTS (N/mm^2)**	**Ys (N/mm^2)**	**Ys (N/mm^2)**	**%E**	**%E**	**Failure Location**
	T_w	**L_w**	**T_w**	**L_w**	**T_w**	**L_w**	
SS304L Base	558		280		41		
P91 Base	695		378		29.22		
CE weld	558.74±28	590.41±12	522.16	464.07	22.91	16.1	weld
E7M weld	685.73±20	659.03±09	559.40	542.59	33.47	22.75	P91
E16M weld	627.91±17	629.14±11	534.36	481.28	23.11	21.25	P91

Note: T_w – Transverse weld, L_w – Longitudinal weld

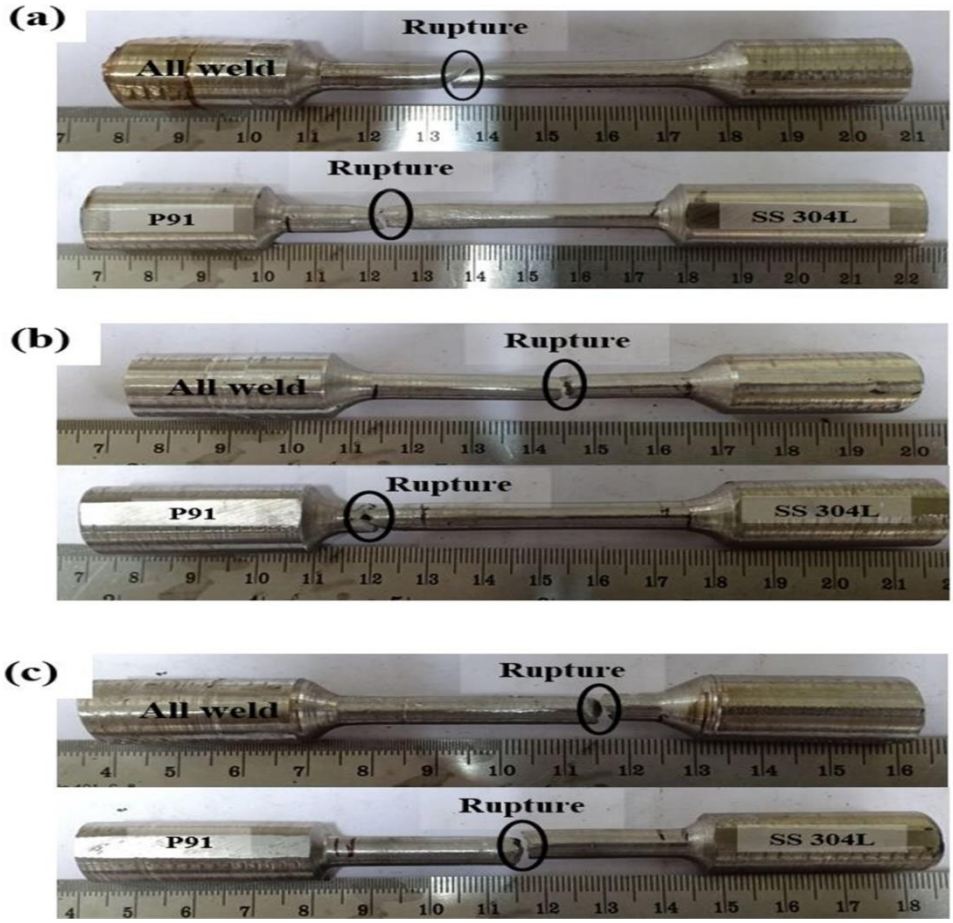

Figure 5.31: Fractured weld tensile test specimen (Transverce and All weld) fabricated using a) Electrode E7M b) Electrode E16M c) Commercial electrode

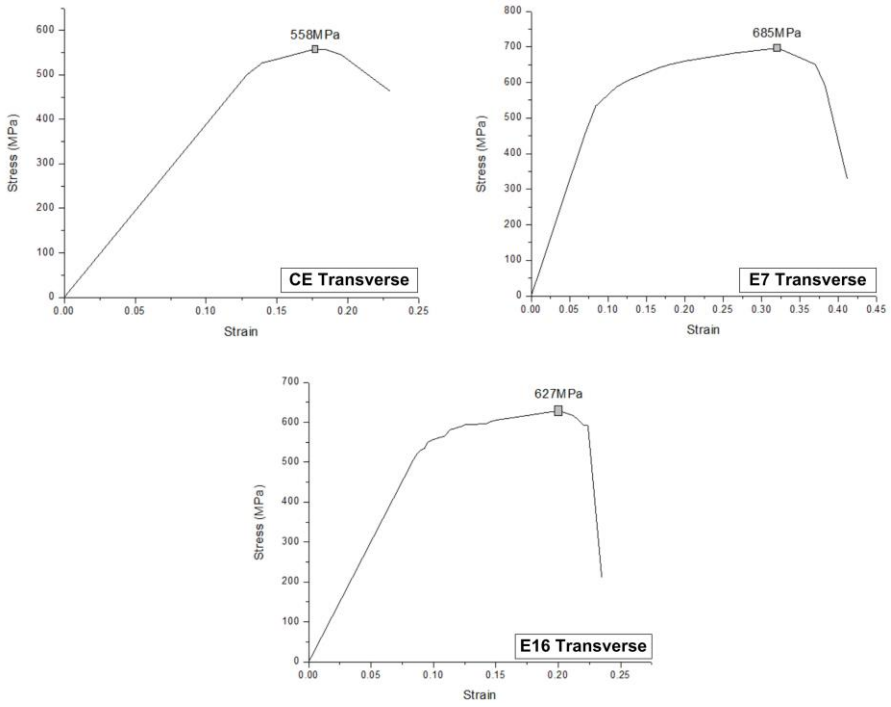

Figure 5.32: Stress vs strain plots of facbricated weld specimen

The welds prepared with developed electrodes E7M show an increased ductility (elongation of 33.47%) compared to the weld made with a commercial electrode having an elongation of 22.9%. The fractographs of weld specimens examined at high magnification using scanning electron microscopy is shown in Fig 5.33. The weld fracture zone has a mix of dimples, ductile dimples,

cleavage facets and tear ridges. The cleavage facet is a low energy fracture that propagates along the cleavage plane and it is symmetrically flat and has matching faces (Thakare et al., 2019).

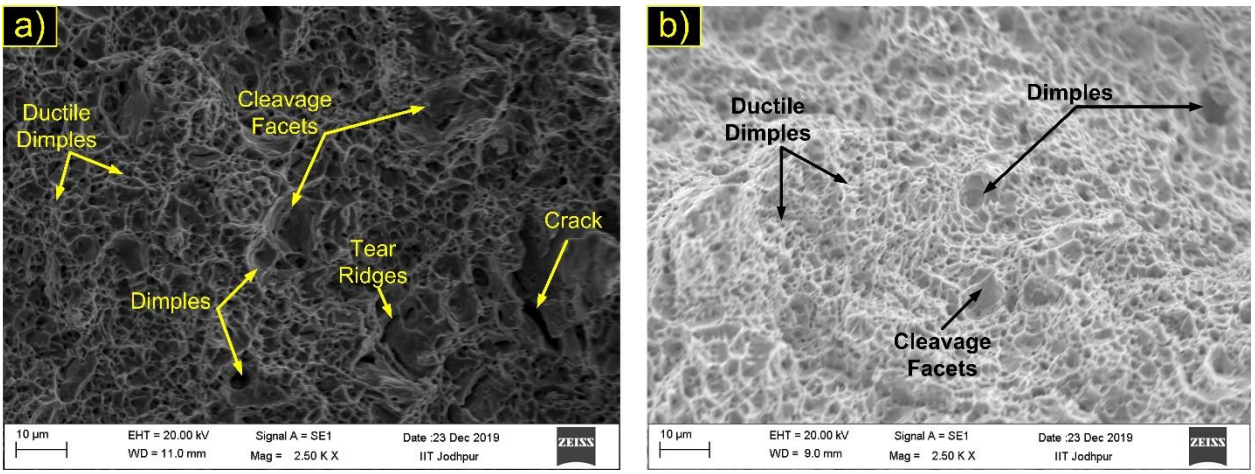

Figure 5.33: Fractography of welded tensile specimens fabricated using (a) Commercial electrodes (b) E7M electrodes

The fractured tensile specimens of welds fabricated using commercial and laboratory developed electrodes here do not have a perfect matching cracked surface, and even the cleavage facets on images are comparatively in lower proportions. This implies cleavage fracture is not the primary mode of fracture here. Weld fabricated with commercial electrodes shows the largest size of dimples on the fractures surface as compared to laboratory made electrodes. The presence of a higher number of ductile dimples on laboratory developed electrode welds confirms the high ductility of welds made as compared to the commercial electrode in which some cracks were also observed. The occurrence of tearing edge and dimple-like morphology indicating the fracture mode of both dissimilar joints are ductile fractures. Furthermore, fractured surfaces of dissimilar joints with E7M electrodes exhibited a higher number of dimples feature which implies higher ductility during the tensile test. This is in good accordance with the results of elongation values in the tensile test shown in Table 522.

Most problems are related to the formation of the carbon-depleted area in HAZ of the carbon steel and to the corresponding carbon-enriched band in the weld transition zone. The carbon depletion in the HAZ leads to a loss of creep strength in DMWs at elevated temperatures. The carbon accumulation in the weld transition zone results in the formation of extremely hard and brittle microstructures that are susceptible to hydrogen-assisted cracking. Hardness and strength increase together with the amount of martensite, but fracture toughness decreases. It explains why a majority of the transition joint failures in austenitic/ferritic steel joints occur in the HAZ of the ferritic steels, adjacent to the weld interface. The coarse-grained heat affected zone (CGHAZ) is a critical region for the performance of the weld (Fig. 5.28e and 5.29e). The results of Charpy impact tests for different welds performed at room temperature are given in Table 5.23. Three specimens were used to carry out the impact test, and the average value was taken. Weld fabricated with laboratory-made electrode E7M has a higher impact fracture energy (139.33±12 J). It has been reported that electrode coatings with high basicity index are detrimental to oxygen content in weld, which in turn has a positive effect on its toughness. It has been reported that replacing CaO with CaF_2 causes a significant reduction in the weld metal oxygen, which improves the toughness (Natalie et al., 1986). Laboratory developed electrode coatings are highly basic coatings with a higher basicity index, which provide welds with better mechanical properties due to the low oxygen and hydrogen levels.

Table 5.23: Impact properties of welds

Specimen	P91 base	SS304L base	Weld CE	Weld E7M	Weld E16M
Impact Energy (J)	247.83±4.5	211.77±8	105.33±5	139.33±12	119.03±7

5.9 Thermogravimetric behavior of P91/SS304L dissimilar welds

Parabolic rate constants for different specimen operated at different conditions were calculated using Eq. 5.23 is expressed in Table 5.24. It is observed from curves Figure 5.34, that weld specimens nearly follow parabolic rates. High temperature parabolic oxidation signifies that a thermal diffusion process is a rate-determining factor. The lower the value of Kp, the higher the oxidation resistance and vice versa.

Table 5.24: Parabolic rate constant ($mg^2\ cm^{-4}\ s^{-1}$) for weld specimens

	750°C SM1	**850°C SM1**	**750°C SM2**	**850°C SM2**
Base P91	0.344×10^{-8}	2.28×10^{-8}	1.72×10^{-8}	3.099×10^{-8}
Base SS304L	8.864×10^{-12}	10.88×10^{-12}	48.606×10^{-12}	66.22×10^{-12}
CE	12.76×10^{-12}	19.06×10^{-12}	89.82×10^{-12}	156.36×10^{-12}
E7M	4.34×10^{-12}	6.65×10^{-12}	24.37×10^{-12}	38.44×10^{-12}
E16M	7.44×10^{-12}	10.72×10^{-12}	41.29×10^{-12}	74.54×10^{-12}

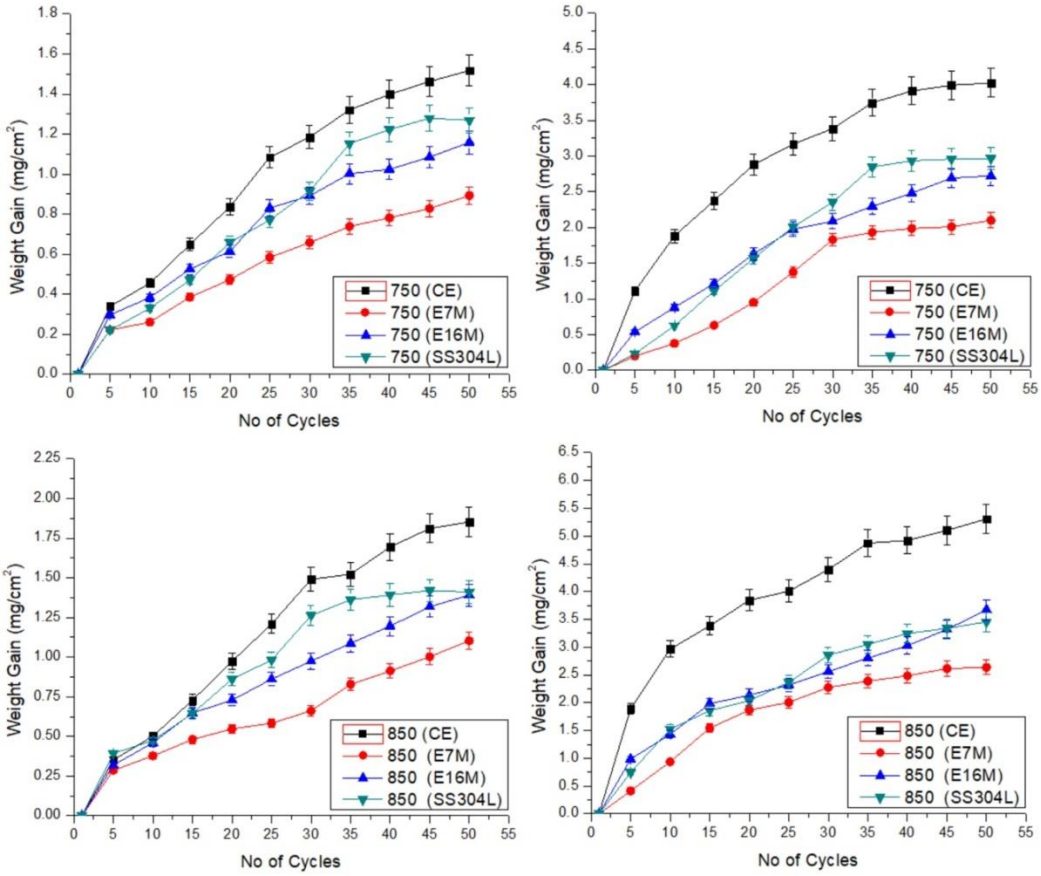

Figure 5.34: Weight gain plots for different specimen a) under the exposure of SM1 at 750°C b) under the exposure of SM2 at 750°C c) under the exposure of SM1 at 850°C d) under the exposure of SM2 at 850°C

It was observed that the Kp for alloy P91 is much higher as compared to the SS304L stainless steel and nickel-based welds. This means that the P91 corrodes at a much faster rate as compared to the SS304L and Ni-based welds. The Kp values for the E7M fabricated welds were lower than the CE fabricated welds. This shows that the welds fabricated using E7M electrodes possess better hot corrosion resistance when exposed to molten salt mixtures at both the temperature. The Kp values for laboratory developed electrode welds either remain comparable or fairs better with that of SS304L stainless steel. This indicates that the weld fabricated with developed electrodes will have enhanced high temperature corrosion resistivity as compared to the ones made with commercial electrodes.

From Figure 5.34, it was observed that the specimen exposed to molten salt mixtures at 850°C gain higher weight for the initial cycles, and the corrosion rate becomes slower as the number of cycles increased. P91 base experienced the highest weight gain in all the cases while E7M welds weight gain was recorded as the lowest. Figure 5.34 also depicts that the welds prepared with laboratory developed electrodes gain lesser weight as compared to the weld made with commercial electrodes. Higher weight gain was observed in the specimen exposed to SM2 as compared to SM1 for both the temperature conditions.

Highly basic electrodes are known to reduce the diffusible hydrogen content of the molten weld pool. This invariably leads to the fabrication of sound and defect-free welds with enhanced structural integrity. The basic coatings aim at reducing these sites, which can become points of high-stress concentration, causing early life weld failure. Cr and Ni in welds are known to increase the corrosion resistance characteristics. Investigations on fabricated weld reveal that welds made with laboratory-developed electrodes contain higher Cr and Ni content as compared to the commercial electrodes. The weld metal chemistry investigation suggests the laboratory developed electrodes to impart improved corrosion resistance to the P91/SS304L dissimilar joint.